

# Contents

<b>I</b>	<b>Fundamentals and theoretical background</b>	<b>1</b>
<b>1</b>	<b>Introduction to the project</b>	<b>3</b>
1.1	The under-development system: <i>Mira</i> . . . . .	3
1.1.1	Development milestones . . . . .	4
1.1.2	Forthcoming developments . . . . .	5
1.2	Setting the goals . . . . .	6
<b>2</b>	<b>Fundamentals of rocketry and numerical heat transfer</b>	<b>7</b>
2.1	A brief history of rocketry . . . . .	7
2.1.1	Early rocketry . . . . .	7
2.1.2	Rocketry becomes a science . . . . .	8
2.1.3	Modern rocketry . . . . .	8
2.2	Principles of rocket propulsion . . . . .	10
2.2.1	The rocket equation . . . . .	10
2.2.2	Rocket as a heat engine . . . . .	11
2.3	Rocket engine key-parameters . . . . .	12
2.3.1	A thermodynamical point of view . . . . .	14
2.4	Liquid rocket engines . . . . .	15
2.5	Numerical modeling of heat transfer . . . . .	18
2.6	General conduction energy equation . . . . .	19
2.6.1	Spatial discretization: the Finite Element Method . . . . .	21
2.6.2	Temporal discretization: the Finite Difference Method . . . . .	23
2.7	A roadmap of the verification process . . . . .	24
<b>II</b>	<b>Verification of the flight model of the engine</b>	<b>27</b>
<b>3</b>	<b>Rocket characterization through measurements</b>	<b>29</b>
3.1	Theoretical approach . . . . .	29
3.1.1	Magnitudes involved . . . . .	29
3.1.2	Rocket engine measurements . . . . .	30
3.1.3	From measurements to data . . . . .	35
3.1.4	From data to results . . . . .	36
3.2	Molding theory into practice: the engine test stand . . . . .	37

3.2.1	Sensors selection . . . . .	37
3.2.2	Sensors suite . . . . .	39
<b>4</b>	<b>Thermal-mechanical analysis</b>	<b>43</b>
4.1	Focusing the problem . . . . .	43
4.1.1	Thrust chamber: a deeper insight . . . . .	43
4.2	From the problem to a model . . . . .	47
4.2.1	A brief introduction to ANSYS/thermal . . . . .	47
4.2.2	Modeling thermal stress with ANSYS . . . . .	49
4.2.3	Input data for thermal stress analysis . . . . .	50
4.2.4	Model statement . . . . .	50
4.3	Preparatory calculations . . . . .	51
4.3.1	Rocket engine design parameters and the CEA tool . . . . .	52
4.3.2	The ideal rocket model . . . . .	54
4.3.3	Chemical analysis of the LOX/Eth70 combustion . . . . .	54
4.3.4	Convergent-divergent nozzle flow study . . . . .	58
4.3.5	Convective heat-transfer coefficients determination . . . . .	61
4.3.6	Materials' properties . . . . .	76
4.3.7	An analytical estimation of the temperature through the wall . . . . .	79
4.4	Thermal-Structural Analysis . . . . .	83
4.4.1	Boundary conditions and meshing process . . . . .	84
4.4.2	Results and discussion . . . . .	86
4.4.3	A tridimensional analysis focused on the injector plate . . . . .	89
4.4.4	Highlights and conclusions . . . . .	91
<b>5</b>	<b>Test-firing the flight model of the engine</b>	<b>107</b>
5.1	Flight model concept . . . . .	107
5.2	Test campaign for the flight model . . . . .	110
5.2.1	Highlights from the campaign . . . . .	110
5.2.2	Test #136: full data reduction . . . . .	111
5.2.3	Post-processing of temperature data . . . . .	115
5.3	Conclusions . . . . .	116
<b>6</b>	<b>Switching to a 700 N thrust chamber</b>	<b>131</b>
6.1	Taking the engine to the next thrust level . . . . .	131
6.1.1	Post-campaign lessons learned . . . . .	131
6.1.2	Thrust-to-Weight ratio augmentation . . . . .	132
6.1.3	Combustion chamber lengthening . . . . .	134
6.2	A summary of the redesign process . . . . .	134
<b>7</b>	<b>Final thoughts</b>	<b>137</b>

# List of Figures

1.1	Mira rocket . . . . .	3
1.2	Thrust chamber geometry evolution . . . . .	5
2.1	Chinese fire-arrows . . . . .	8
2.2	Tsiolkovsky's original rocket sketch, burning liquid hydrogen (H) and liquid oxygen (O) . . . . .	9
2.3	Goddard's rocket scheme . . . . .	9
2.4	Öberth's V-2 rocket . . . . .	10
2.5	Thrust chamber . . . . .	12
2.6	Schematic of a pressure-fed liquid rocket engine . . . . .	15
2.7	Variation of Mach number, pressure, temperature and density through a supersonic nozzle . . . . .	17
2.8	Wall heat fluxes in a rocket chamber . . . . .	19
2.9	Boundary conditions for the general conduction equation . . . . .	20
2.10	FEM approach: the solution region is divided into nonoverlapping elements with nodes on vertexes . . . . .	21
2.11	FDM approach: temperature variation within a time step . . . . .	23
3.1	Pivot mounts . . . . .	31
3.2	Ball or roller mounts . . . . .	32
3.3	Flexural mounts . . . . .	33
3.4	Bell crank mount . . . . .	33
3.5	Basic scheme for data acquisition from sensors . . . . .	36
3.6	Calculation scheme: from measured data to rocket parameters . . . . .	37
3.7	Schematics of the test stand . . . . .	41
4.1	Mechanical and thermal loads acting upon a rocket's thrust chamber	45
4.2	Typical stresses in a thrust chamber inner wall . . . . .	46
4.3	Sequential coupled-field analysis data flow scheme . . . . .	48
4.4	Thermal-stress analysis model . . . . .	51
4.5	Chamber temperature and specific impulse vs propellant mixture ratio for the LOX/Eth70 propellant combination . . . . .	53
4.6	Characteristics of the isentropic expansion through the nozzle . . . . .	59
4.7	Nozzle contour discretization . . . . .	60

4.8	Heat transfer coefficient distribution (Bartz method)	64
4.9	Boundary layer evolution along the nozzle according to the Schoenman-Block scheme	65
4.10	Heat transfer coefficients correlation for the JPL-1 rocket nozzle	66
4.11	Logarithmic pressure distribution for the JPL-1 rocket nozzle	67
4.12	Logarithmic pressure-gradient extrapolation	70
4.13	Laminarization of the boundary layer	70
4.14	Heat transfer coefficient distribution (Schoenman-Block)	71
4.15	Comparison between heat transfer coefficient distributions	72
4.16	Heat-transfer modeling on the faceplate	73
4.17	Materials' properties radar distribution	79
4.18	Temperature profiles estimation	83
4.19	Applied boundary conditions on the thrust chamber and meshing process result	85
4.20	Temperature distribution [K] at $\tau = 20s$	93
4.21	Temperature distribution [K] on the faceplate at $\tau = 20s$	94
4.22	Temperature profiles [K] in different stations	95
4.23	Heat flux density mapping [ $W/m^2$ ] at $\tau = 20s$	96
4.24	Temperature and total heat flux distribution along the nozzle at $\tau = 20s$	97
4.25	Total deformation of the structure [m] at $\tau = 20s$	98
4.26	Von Mises stress distribution [Pa] at $\tau = 20s$	99
4.27	Steel injector plate stress distribution [Pa] at $\tau = 20s$	100
4.28	Graphite inlay stress distribution [Pa] at $\tau = 20s$	101
4.29	Ceramic shell stress distribution [Pa] at $\tau = 20s$	102
4.30	Global deformation of the assembly under thermal loading	103
4.31	Additional boundary conditions for the tridimensional analysis	103
4.32	Temperature distribution [K] on the three-dimensional injector plate at $\tau = 20s$	104
4.33	Stress distribution [Pa] on the three-dimensional injector plate at $\tau = 20s$	105
5.1	Chamber length as a function of throat diameter	109
5.2	Comparison: engineering model vs flight model	109
5.3	Test #131: thrust chamber detachment and consequent impact damage	119
5.4	Data reduction scheme	120
5.5	Thrust vs time curve	121
5.6	Mass flow rate over burning time	122
5.7	Pressure in the combustion chamber over the burning time	123
5.8	A detailed analysis of chamber pressure evolution	124
5.9	Correlation between pressure instability and mixture ratio	125
5.10	Effects of erosion on the engine performance	126
5.11	Thermocouples positions	126

- 5.12 Temperature evolution over the firing time at TC $\emptyset$  measuring point 127
- 5.13 Temperature evolution over the firing time at TC6 measuring point 128
- 5.14 Temperature evolution over the firing time at TC7 measuring point 129



# List of Tables

1.1	Design parameters of the rocket system . . . . .	4
1.2	Thrust chamber geometry evolution . . . . .	5
4.1	Analogy between thermal and structural problem . . . . .	47
4.2	Flight model's parameters and estimated performance . . . . .	53
4.3	Calculated parameters for LOX/Eth70 propellants, Mira rocket engine . . . . .	57
4.4	A comparison in the results of the Bartz method: Mira's nozzle vs Bartz' nozzle . . . . .	64
4.5	Results from the Schoenman-Block method . . . . .	71
4.6	Temperature effect on thermal properties of the materials . . . . .	78
4.10	Graphite erosion rates and effects on rocket's performance . . . . .	79
5.1	Comparison between expected and under hot-fire test delivered performance . . . . .	118
6.1	A comparison between the 500 N and the 700 N designs . . . . .	135



## **Part I**

# **Fundamentals and theoretical background**



# Chapter 1

## Introduction to the project

Designing and developing a space system always comes to a point where the project moves from the drawing board into a phase of construction and verification: design parameters, a priori established in a preliminary design phase, need to be verified beyond doubt by means of an engineering model of the system, before manufacturing the actual flight model. Passage to the so called phase C (according to ECSS' space system lifetime phases) is so marked.

The same phase is undergoing the system designed by the SMART Rockets Project Team at the TU Dresden: a sounding rocket is under development to prove the students' capability to deal with a space-asset design project and promote a know-how acquisition experience in the field among them. At the time of writing the system is mature enough to undergo a test campaign, aimed at the verification of the flight model design.

### 1.1 The under-development system: *Mira*

TU Dresden's response to the *STERN* (STudentische Experimental RaketeN) *Programme* call - issued by the German Space Agency - for developed-by-students rockets, is a bipropellant pressure-fed liquid rocket engine system (in Fig. 1.1 a rendering of Mira). Liquid oxygen and ethanol the propellants, pressure fed by gaseous nitrogen.

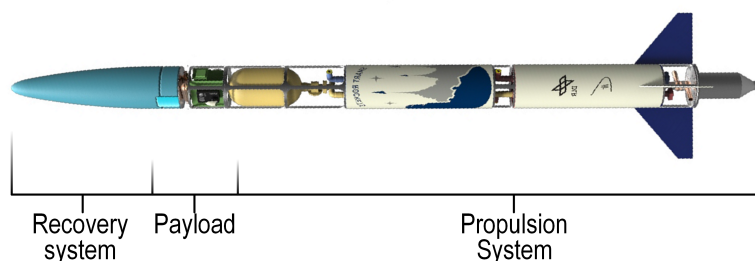


Figure 1.1: Mira rocket

<b>Parameter</b>	<b>Value</b>
Thrust [N]	500+
Chamber pressure [MPa]	1.5+
Oxidizer to fuel ratio [-]	1.0+

**Table 1.1:** Design parameters of the rocket system

Designed in compliance with DLR preliminary mission requirements - i.e. speed of sound achievement, apogee of 3+ km, flight data storage and real time transmission, safe recovery of a payload - the rocket, in its current design, is capable of delivering 500 N of thrust over 20 s of firing time. In the early stage of the project, three design parameters - namely thrust, combustion chamber pressure, and oxidizer to fuel mixture ratio - have been identified and set within reasonable ranges by comparison with similar LOX/Ethanol propelled rockets, and the rocket engine's layout, in terms of geometry and selected materials, tailored upon them in the different models which came in succession.

### 1.1.1 Development milestones

Since August 2012, when the SMART Rockets Project officially started, the design of the rocket system went successfully through Phases Ø, A and B. At the time of writing the team is finalizing phase C (Detailed Definition) yet with a step forward into Production and Qualification D phase, towards the engine verification in its flight version.

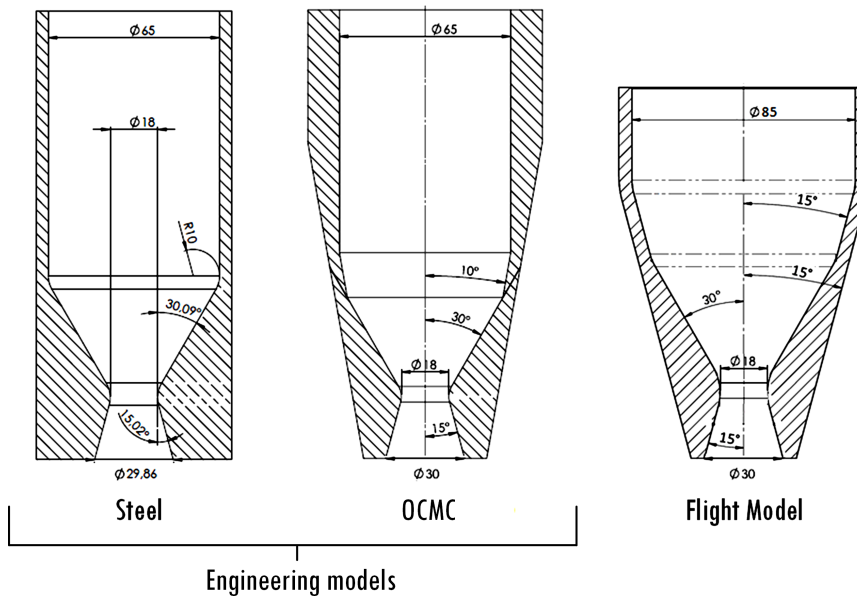
In the time in between, the thrust chamber design underwent its own evolution - in geometry layout and employed materials - well summed-up by Figure 1.2 and Table 1.2. Up to now two engineering models have been manufactured and tested. A steel housing, graphite inlay combustion chamber represented the first step in chamber development. Almost same geometry, but totally different housing material (a promising Oxide-oxide Ceramic Matrix Composite, OCMC) characterizes the second model. Whatever the model, the geometry of the nozzle's divergent portion is frozen, in terms of length, diameter at throat and expansion ratio. As for the injector plate, its geometry changes according to the chamber section from one model to another with the material always being a stainless steel. The models successfully underwent testing. In particular:

- in september 2014 the steel/graphite design achieved a thrust of 400 N during fire test #91
- in november 2015 the OCMC/graphite design delivered a thrust of 470 N during fire test #122

Both the top-performance tests above mentioned, almost achieved a 1.1 mixture ratio, so far adopted as the design value for the LOX/Ethanol combination's performance.

**Table 1.2:** Thrust chamber geometry evolution

Parameter	Steel	OCMC	Flight Model
Length [mm]	148	148	141
Diameter [mm]	65	65	85
Contraction ratio [-]	13	13	23
Characteristic length [m]	1.6	1.6	1.1
Expansion ratio [-]	2.8	2.8	2.8

**Figure 1.2:** Thrust chamber geometry evolution

### 1.1.2 Forthcoming developments

Time is ripe to take the final step in thrust chamber design, that is, the verification of its flight model. Once again, materials (OCMC casing + Graphite inlay + Stainless steel injector plate) stay the same as well as the nozzle geometry downstream of the throat. Then what marks a shift in thrust chamber design are the following features (as one can spot in Figure 1.2):

- a shorter overall thrust chamber length, thus a smaller combustion chamber volume and in the end a decreasing characteristic length - with all that that implies
- the nozzle contour upstream of the throat now follows a double cone (30 deg and 15 deg apertures) before getting straight cylindrical on the aftmost section. Suitable fillet radii allow a smooth transition from one surface to another (no sharp edges on the inner wall contour)

- a larger combustion chamber cross section area - as a consequence of a wider aperture angle for the second cone - i.e. a higher contraction ratio given the fixed throat section

Further modifications, aside the ones concerning the geometry, include:

- a higher mixture ratio - switching from the current 1.1 to a 1.2 value - still a fuel-rich mixture but one tenth closer to the performance optimum for the selected propellant combination, in the attempt to reach a better performance
- a higher level of thrust. Indeed the rocket engine requirement *PR-3000-FPAM-002* in [8] sets the thrust to a minimum of 500 N. And another project requirement *PR-0000-FP-AIT-017* limits the lift-off weight below 25 kg for avoiding the necessity of a certification by the Federal Office of Civil Aeronautics. With a maximum weight at lift-off of 25 kg the provided thrust-to-weight ratio would be roughly 2, not enough to ensure an adequate stability as soon as it leaves the launchpad. Here comes the need - to be put into effect by long-term developments - to switch to 700 N of thrust. In the short-term anyway, already the upcoming test campaign will provide indications about future improvements towards the 700 N design.

## 1.2 Setting the goals

The present Master's thesis work - embedded within the SMART Rockets Project - is concerned with the verification of the engine design in its flight version. Here follows the assignment of tasks:

1. Research about rocket engine measurements and their characterization
2. Development of a method for measuring the above derived characteristics
3. Numerical verification (thermal-mechanical analysis) of the flight model design
4. Fire-test verification of the flight model design
5. Post-campaign data reduction and analysis
6. Deriving potential design changes for the 700 N engine

## **Chapter 2**

# **Fundamentals of rocketry and numerical heat transfer**

The present chapter is devoted to recall basic notions about rocketry and to collect theoretical basics regarding numerical heat transfer, without pretension to be exhaustive, since providing a comprehensive theoretical background about the subjects above mentioned, is something beyond the purpose of both this chapter and this thesis work. For the sake of brevity only gas pressure-fed liquid rocket engines are dealt with, the rocket we are going to work on being such a type of system. As for the few concepts introduced about numerical heat transfer, they will prove useful in better understanding the backbone behind the numerical modeling of heat transfer phenomena.

### **2.1 A brief history of rocketry**

Man bumped into rockets probably by chance: in the beginning rockets were a way to entertain people. Then someone realized rockets' potential as a weapon. And only in the end rockets became the means by which man could reach the stars.

#### **2.1.1 Early rocketry**

Probably the first rocket-like devices were accidents. In the first century A.D., the Chinese reportedly used bamboo tubes filled with a simple form of gunpowder mostly for fireworks in religious and other festive celebrations. Perhaps, once torched, some of those tubes failed to explode and instead flew away, propelled by the gases produced from the burning gunpowder. Anyway the first use of true rockets dates back to 1232 when the Chinese repelled the Mongol invaders by a barrage of "arrows of flying fire": these fire-arrows were a simple form of a solid-propellant rocket (see Fig.2.1).

Over the centuries, rocket slowly spread to the West as a military weapon. However, not until the end of the 19th century and the beginning of the 20th century was the rocket understood from a technical viewpoint and was its true engineering development begun.



**Figure 2.1:** Chinese fire-arrows

### 2.1.2 Rocketry becomes a science

Before Sir Isaac Newton and his *Principia*, many were able to operate a rocket but none has ever tried a scientific approach to rocketry, the basics of which lay in the the well-known three laws. In the meantime rocket experimenters in Germany and Russia began working with rockets with a mass of more than 45 kilograms. Colonel William Congreve, a British Army artillery expert, improved rocket as a barrage missile. Another englishman, William Hale, developed a technique called spin stabilization to achieve accuracy improvement. By the end of nineteenth century non-military use of solid propellant rocket included whaling, signaling, the transfer of lifelines between ships.

Heavy artillery introduction however, put an end (at list for a while) to the rocket-as-a-weapon era: rocketry needed new challenges.

### 2.1.3 Modern rocketry

"Possibly the first seeds of the idea were sown by..Jules Verne. He directed my thinking": when the young Konstantin Tsiolkovsky read Verne's stories of space travel, he got caught by them. An early visionary, he imagined the three-stage rocket, space stations and the colonization of other worlds. Born in Russia in September 1857, Tsiolkovsky is regarded as the first true rocket scientist. Figure 2.2 depicts his concept of a rocket fueled with liquid hydrogen ( $H_2$ ) and liquid oxygen ( $O_2$ ), which was published in the Russian magazine Science Survey ("Investigation of outer space by means of reaction apparatus") in 1903: the fact that Tsiolkovsky knew to use the high specific impulse combination of  $H_2 - O_2$  testifies to the sophistication of his rocket theory.

Another boyhood was filled with dreams of flight by Verne: Robert H. Goddard's. Born in Worcester, Massachusetts, on October 5, 1882, his life had many parallels to Tsiolkovsky's: he too was an avid physicist and mathematician. He too was convinced that rockets were the key to space flight. And he too worked in virtual obscurity for most of his life. But there was one sharp difference. Whereas



**Figure 2.2:** Tsiolkovsky's original rocket sketch, burning liquid hydrogen (H) and liquid oxygen (O)

Tsiolkovsky's contributions were purely theoretical, Goddard was a pure rocketeer successfully capable of molding theory into practice thus developing the world's first liquid-fueled rocket that worked (see Fig.2.3): on March 16, 1926 it was launched into the cold winter air, achieving an altitude of 41 feet, in a 2.5 seconds flight.

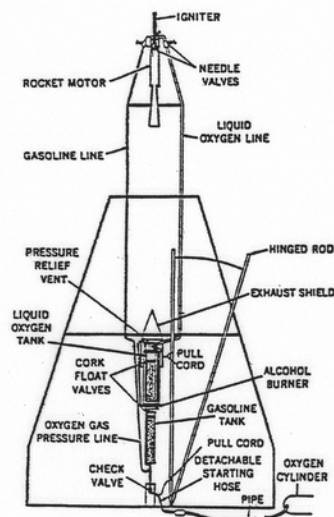


**Figure 2.3:** Goddard's rocket scheme

Quoting Prof. John D. Anderson, Jr. [4], the early history of rocket engines forms a geographic triangle, with one vertex in Russia (Tsiolkovsky), the second in the United States (Goddard), and the third in Germany. Representing this third last vertex is Hermann Oberth, born Romanian on July 25, 1894 and later became German citizen. As a young boy, he calculated the acceleration of an object under the Earth's gravitational pull and found his calculation for escape velocity - 11.2 kilometers per second - to be in agreement with his hero, Jules Verne. He grew up with the idea of rockets as a means for space flight: Oberth's ideas had a catalytic effect, especially on some of his students, such as Wernher Von Braun. And the 1930s found an almost explosive development of rocketry in Germany,

started by the successful flight of the first German rocket *Einstaber* in August 1931. His work along with Von Braun as the technical director, culminated in the development of the German V-2 rocket during World War II (see Fig. 2.4). Although an instrument of war, the V-2 was the first practical long-range rocket in history. During the closing phases of World War II, hundreds of production V-2s were captured by both Russian and U.S. forces and shipped back to their respective countries. As a result, all modern rockets today can trace their ancestry directly back to the V-2 and hence, through Von Braun, back to Hermann Oberth.

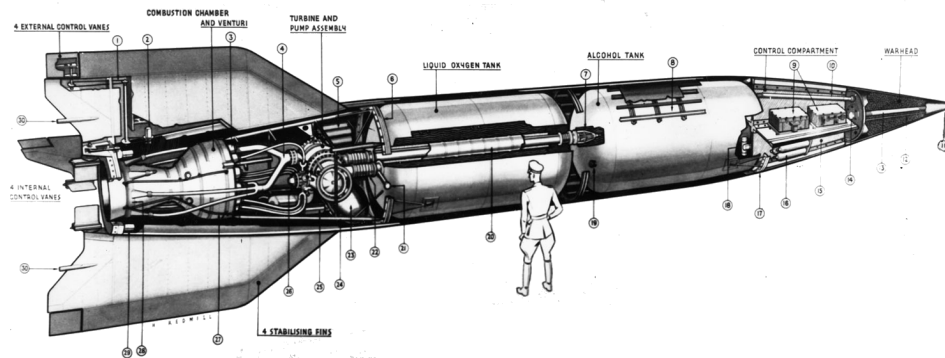


Figure 2.4: Oberth's V-2 rocket

These three gifted men, working independently in different countries, inspired by Verne's novel *From the Earth to the Moon*, explored how rockets could be designed and used for space travel. Today, they are referred to as "Fathers of rocket science".

## 2.2 Principles of rocket propulsion

Among the countless ways to engineer Newton's laws of motion there are rockets. Like a deflating toy balloon, a rocket propels itself by expelling a jet of matter: the momentum carried away by the jet results in a force, which in the end accelerates the rocket in the opposite direction of the jet.

As seen in the previous section, rocket has been a merely practical device for more than a thousand years until Tsiolkovsky came up with a simple law giving rocketry, for the first time, the status of science. So, in moving through basic rocketry, let us start from the beginning with Tsiolkovsky's rocket equation.

### 2.2.1 The rocket equation

Consider a rocket vehicle, the mass of which decreasing due to propellant expenditure and the sole force acting upon which is thrust:

$$F = -\dot{m}c$$

here expressed as the product between the time rate of change of mass due to propellant consumption and the (effective) exhaust velocity. The minus sign indicates the thrust being the reaction, equal and opposite, to the action exerted by gases upon the inner walls of the nozzle and the combustion chamber. Let us now express the same force in terms of Newton's second law:

$$F = m \frac{dv}{dt}$$

Combining the two expressions and integrating between initial - ignition, " $\bullet_i$ " - and final state - " $\bullet_f$ " -, results in the Tsiolkovsky formula, as much simple as revealing:

$$\Delta v = v_f = c \log_e \frac{M_i}{M_f}$$

one can infact notice that:

- the final velocity of the vehicle is just a function of the final mass ratio (i.e. how much propellant has been burned) and the exhaust velocity (i.e. how fast the mass can be expelled), no matter the level of thrust
- for a given exhaust velocity, the higher the mass ratio, the higher the final velocity, but with a diminishing return (note that the mass ratio is argument of a logarithm)
- the final mass ratio is always greater than one. In particular when it equals  $e$ , the basis of natural logarithm, the rocket is travelling as fast as the gas exhaust from the nozzle
- for a given final mass ratio, the higher the exhaust velocity, the higher the final velocity

It is finally important to point out that Tsiolkovsky equation's range of validity is limited by the assumptions of non thrust-velocity misalignment and the action of no other forces but thrust upon the rocket.

### 2.2.2 Rocket as a heat engine

Adopting a thermodynamical point of view a rocket can also be thought of as a heat engine: it converts the heat generated by propellants reaction - fuel and oxidizer - in the combustion chamber, into kinetic energy of a jet stream at the nozzle exhaust. This perspective offers a deeper insight into rocket functioning and a more *local* explanation of thrust generation compared to the *big picture* depicted through Newton's laws, where thrust is simply the reaction experienced by rocket's structure due to the ejection of matter at high velocity.

So let us consider a one-dimensional model of a rocket thrust chamber, as the one depicted in Figure 2.5. In the middle of the combustion chamber, a hot almost-stationary gas collects the energy - represented by the temperature and

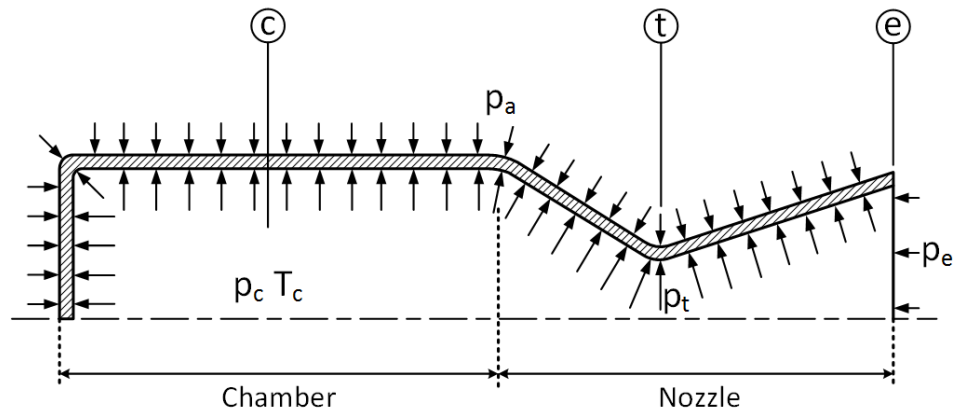


Figure 2.5: Thrust chamber

the pressure of the gas - released in the chemical reaction. This energy is then converted into velocity by the expansion and the cooling through the nozzle, where the velocity rises very rapidly, passing the speed of sound (for the local conditions) as it crosses the throat of the nozzle. Thereafter it continues to accelerate until it leaves the nozzle. This energy-conversion process results into a local pressure distribution on the inner walls of the chamber and in the end in two forces: the pressure force of the gas, which accelerates forward the rocket; and the reaction of the internal surfaces of the rocket engine, which accelerates rearward the gas.

### 2.3 Rocket engine key-parameters

A set of six parameters can exhaustively determine and describe the performance of a rocket system (for a rigorous derivation of the following expressions see [1], [2] and [3]):

- Net thrust delivered:

$$F_T = \dot{m}_p u_e + A_e(p_e - p_a) \quad (2.1)$$

where the first term, the momentum thrust, is the product of the propellant mass flow rate and its exhaust velocity relative to the vehicle. The second one is the product of the cross-sectional area at the nozzle exit  $A_e$  and the difference between the exhaust gas pressure at the exit and the ambient fluid pressure. Note that in this case - differently from subsection 2.2.1 - the propellant mass flow rate multiplies the *actual* exhaust velocity.

- Thrust coefficient:

$$C_T = \frac{F_T}{p_c A_t} \quad (2.2)$$

it measures the force augmented by the gas expansion through the nozzle, as compared to the force which would be generated if the chamber pressure acted over the throat area only. Then it can be thought of as a measure of the nozzle thrust-amplification capability (gain factor).

- Characteristic velocity:

$$c^* = \frac{p_c A_t}{\dot{m}_p} \quad (2.3)$$

it relates to the efficiency of combustion independently of nozzle characteristics: the lower the propellant consumption  $\dot{m}_p$ , the higher  $c^*$ , which indicates a combustion process of higher energy and efficiency.

- Total impulse:

$$I_t = \int_0^{t_b} F(t) dt \quad (2.4)$$

it is the thrust integrated over the burning time, i.e. the total change in vehicle momentum that can be achieved. For constant thrust and very short buildup and shutdown transients, the expression for  $I_t$  simplifies to:

$$I_t = F_T t_b$$

- Specific impulse:

$$I_{sp} = \frac{\int_0^{t_b} F(t) dt}{g \int_0^{t_b} \dot{m}_p dt} \quad (2.5)$$

it is the amount of impulse imparted to a vehicle per unit sea-level weight of propellant expended. It is an important figure of merit of the performance of a rocket propulsion system, similar in concept to the kilometers per litre parameter used in automotive: the higher  $I_{sp}$ , the better the rocket performance. Note that specific impulse's unit of measure is *seconds*: obviously it does not denote a time, but rather a magnitude akin to efficiency: two different rocket engines have different values of specific impulse and the same thrust-level; for the same amount of propellant, the engine with the higher value of specific impulse is more efficient because it delivers the same thrust over a longer timespan. Indeed a more practical definition regards the specific impulse as the time over which a rocket system can deliver a thrust amounting to the initial weight of propellant onboard. For constant thrust and mass flow, neglecting start and stop transients, the specific impulse is given by:

$$I_{sp} = \frac{F_T}{g \dot{m}_p} \quad (2.5.1)$$

- Effective exhaust velocity:

$$c = \frac{F}{\dot{m}_p} = I_{sp}g \quad (2.6)$$

it is the average equivalent velocity at which propellant is ejected from the vehicle. Since  $c$  and  $I_{sp}$  differs only by the  $g$  factor, either one can be used as a measure of rocket performance. In rocket engineering anyway,  $I_{sp}$  is usually preferred to  $c$ , since the former takes the same value in the metric and imperial systems.

### 2.3.1 A thermodynamical point of view

Under the assumption of ideal rocket model (details in [1], [2] and [3]) the above derived parameters can be rearranged in a more-thermodynamic fashion, relating them exclusively to chamber and nozzle processes and propellant properties. It follows:

- Characteristic velocity:

$$c^* = \frac{\sqrt{g\gamma RT_c}}{\gamma \sqrt{\frac{2}{\gamma+1}}^{\frac{\gamma+1}{\gamma-1}}} \quad (2.3T)$$

- Thrust coefficient:

$$C_F = \sqrt{\frac{2\gamma^2}{\gamma-1} \left[ \frac{2}{\gamma+1} \right]^{\frac{\gamma+1}{\gamma-1}} \left[ 1 - \left( \frac{p_e}{p_c} \right)^{\frac{\gamma-1}{\gamma+1}} \right] + \epsilon \left[ \frac{p_e - p_a}{p_c} \right]}$$

For an ambient pressure-matched nozzle, it simplifies to:

$$C_T = \sqrt{\frac{2\gamma^2}{\gamma-1} \left[ \frac{2}{\gamma+1} \right]^{\frac{\gamma+1}{\gamma-1}} \left[ 1 - \left( \frac{p_e}{p_c} \right)^{\frac{\gamma-1}{\gamma+1}} \right]} \quad (2.2T)$$

- Specific Impulse: combining equations (2.2), (2.3), (2.5.1), it follows:

$$I_{sp} = \frac{C_T c^*}{g}$$

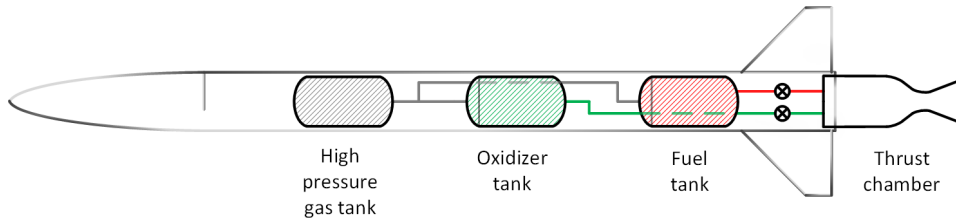


**Figure 2.6:** Schematic of a pressure-fed liquid rocket engine

finally, substitution of equations (2.2T) and (2.3T) leads to:

$$I_{sp} = \frac{\sqrt{\gamma RT_c}}{\gamma \sqrt{g} \sqrt{\frac{2}{\gamma+1}}^{\frac{\gamma+1}{\gamma-1}}} \sqrt{\frac{2\gamma^2}{\gamma-1} \left[ \frac{2}{\gamma+1} \right]^{\frac{\gamma+1}{\gamma-1}}} \cdot \sqrt{\left[ 1 - \left( \frac{p_e}{p_c} \right)^{\frac{\gamma-1}{\gamma+1}} \right]} \quad (2.5T)$$

## 2.4 Liquid rocket engines

Basically, the hardware required to a liquid propellant rocket engine system in order to produce thrust, comprises a thrust chamber - that is, a combustion chamber followed by a convergent-divergent nozzle - and the propellant tanks along with the means by which propellants are driven into the chamber. The whole is connected to a structure to transmit the thrust force. Fig. 2.6 depicts the basic schematic of a pressure-fed bipropellant liquid rocket engine.

In a quick look from the left to the right, the high-pressure gas tank is the first subsystem to come into view. It represents the feed system and its function is to force the propellants into the combustion chamber. In the specific case of a pressure-fed rocket, the energy to perform this function comes from a high-pressure inert gas stored in a designated tank. So basically the system is designed to supply the propellant tanks, over the burning time, with pressure levels high enough to ensure the propellant injection at the design flow rate. Such a system is very simple and reliable, so perfectly tailored to fit not-so-restrictive and demanding mission requirements (e.g. sounding rockets and reaction control systems). Downstream of the feeding gas tank, the liquid propellants are stored in an oxidizer tank and a fuel tank. Specifically in Fig. 2.6 they are arranged in a tandem configuration with internal piping. Finally the rightmost subsystem in the figure: the thrust chamber. Quoting Huzel and Huang from [3] *"..the thrust-chamber assembly undeniably embodies the essence of rocket propulsion: the acceleration and ejection of matter, the reaction to which imparts propulsive force to the vehicle"*. Common denominator in liquid propellant chamber systems is the presence of three main subassemblies. Following the flow in its path through the chamber from injection to ejection:

1. it is split into tiny droplets through an atomization process by the *injectors* installed on the faceplate at the chamber's base
2. it then undergoes a combustion process triggered by an *igniter* usually mounted at the center of the injector plate
3. it finally crosses the *nozzle* experiencing the thermodynamical process described in subsection 3.2.2

### Isentropic nozzle flow

The same thermodynamical process occurring in the nozzle can be treated as an isentropic transformation without big loss or divergence from reality. In real nozzle flows indeed little or no heat is added or taken away through the walls and a vast core of the flow is virtually frictionless, thus contributing to keep reasonably acceptable the hypotheses of adiabaticity and reversibility.

$$\left(\frac{A}{A_t}\right)^2 = \frac{1}{M^2} \left[ \frac{2}{\gamma+1} \left( 1 + \frac{\gamma-1}{2} M^2 \right) \right]^{\frac{\gamma+1}{\gamma-1}} \quad (2.7)$$

$$T = T_c \left[ 1 + \frac{\gamma-1}{2} M^2 \right]^{-1} \quad (2.8)$$

$$p = p_c \left[ 1 + \frac{\gamma-1}{2} M^2 \right]^{-\frac{\gamma}{\gamma-1}} \quad (2.9)$$

$$\rho = \rho_c \left[ 1 + \frac{\gamma-1}{2} M^2 \right]^{-\frac{1}{\gamma-1}} \quad (2.10)$$

The isentropic nozzle flow equations 2.7, 2.8, 2.9 and 2.10 allow to analyze the flow evolution from chamber to exhaust in terms of Mach number and static temperature, pressure and density. It is possible to plot them versus the coordinate  $x$  along the nozzle axis. Typical trends for the above mentioned magnitudes are qualitatively depicted in Fig. 2.7.

### Heat transfer phenomena

A rocket, in its nature of a combustion device, is home to thermal exchanges and heat transfer phenomena. In a rocket chamber heat is transmitted to all internal hardware surfaces exposed to hot gases and the way it transfers is a matter of radiation, convection and conduction: all the three fundamental heat transfer mechanisms (each one with its own contribution) are involved in generating and moving heat fluxes in the chamber. Consider Fig. 2.8. Moving from the hot gas side, through the wall, to the outer cold side, there can be found three main fluxes:

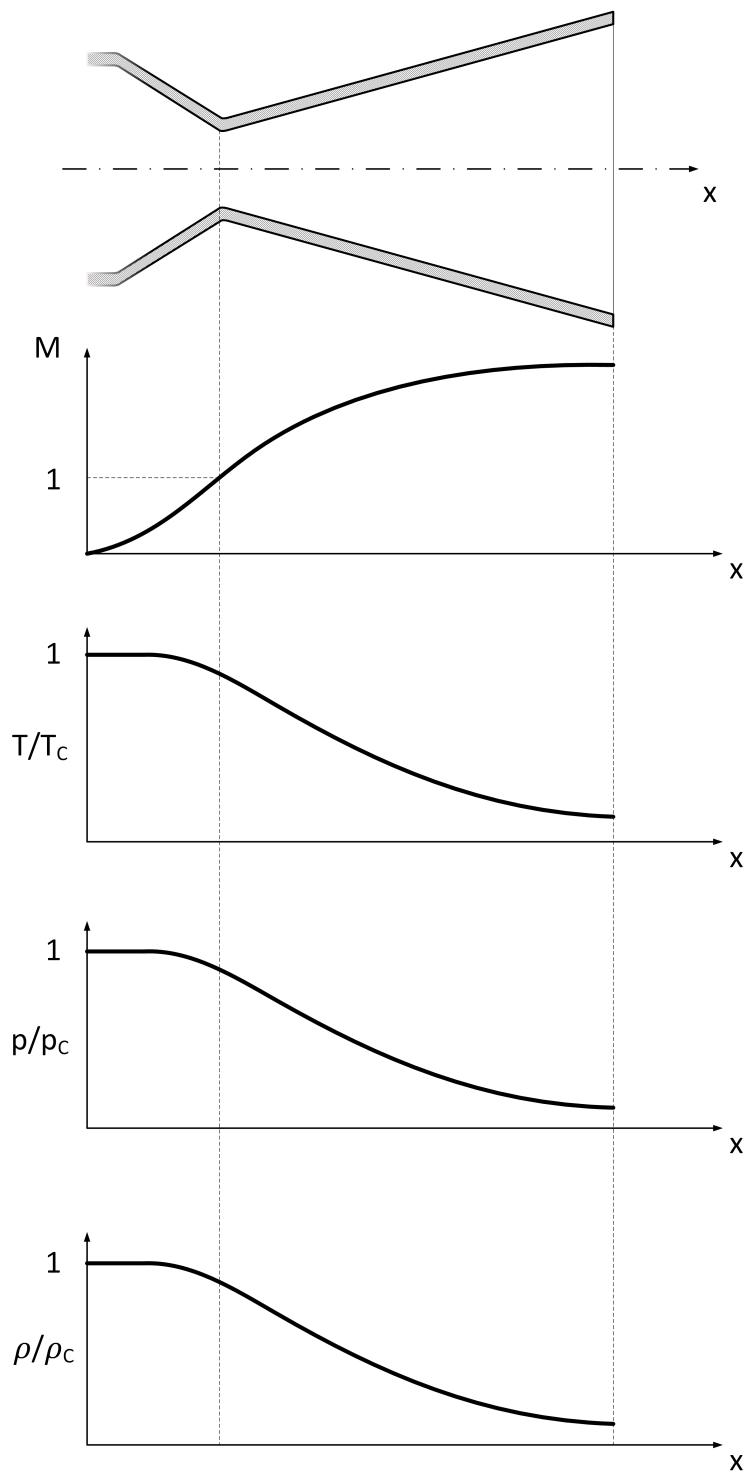


**Figure 2.7:** Variation of Mach number, pressure, temperature and density through a supersonic nozzle

- a omnidirectional radiative heat flux  $q_{\text{RAD}}$  generates in the hot combustion core and spreads towards the wall. It is proportional to the fourth power of the absolute temperature according to the Stefan-Boltzmann law for a grey body:

$$q/A = \epsilon \sigma T^4 \quad [\text{W/m}^2]$$

with the surface emissivity  $\epsilon$  ranging from zero to one and  $\sigma$ , the Stefan-Boltzmann constant, equal to  $5.6697 \cdot 10^{-8} \text{ W/m}^2 \cdot \text{K}^4$

- nearby the inner wall a convective heat flux  $q_{\text{CONV}_i}$  causes a temperature fall - from  $T_i$  on the free-stream hot gas side to  $T_{wi}$  on the wall - governed by the Newton's law of cooling

$$q/A = h(T_{wi} - T_i)$$

where  $h$  is the convective heat transfer coefficient in  $\text{W/m}^2 \cdot \text{K}$ ,  $T_{wi}$  the wall temperature,  $T_i$  the fluid temperature.

- conduction through the wall  $q_{\text{COND}}$  lowers the temperature to the  $T_{wo}$  value on the outer side of the wall. This time Fourier's law applies:

$$q/A = -k \frac{\partial T}{\partial n}$$

$\partial T / \partial n$  being the temperature gradient in the direction normal to the area  $A$ ,  $k$  the thermal conductivity in  $\text{W/m} \cdot \text{K}$

On the outer side a fourth convective flux  $q_{\text{CONV}_o}$  - due to forced convection just like  $q_{\text{CONV}_i}$  on the inner wall - could arise in the presence of a moving fluid (e.g. ambient air or coolant). Convection and radiation are major contributors to heat transfer in a combustion chamber, whereas conduction is negligible compared to them.

## 2.5 Numerical modeling of heat transfer

The heat transfer phenomena occurring in a rocket chamber can affect a rocket in at least two ways:

- by reducing the performance. This tends to be a 1-3% effect on the specific impulse only, and is therefore secondary
- by introducing challenging tasks in the design of hot-side structures that have to survive large heat fluxes

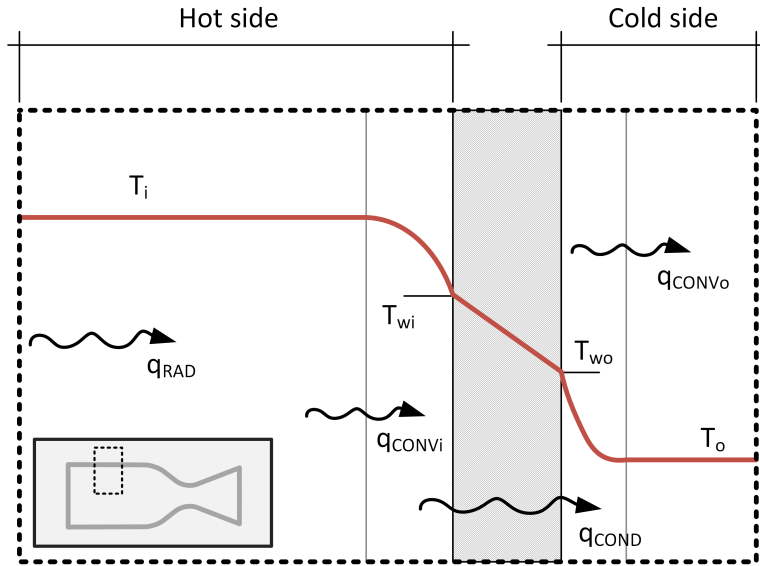


**Figure 2.8:** Wall heat fluxes in a rocket chamber

Indeed, designing against thermal overload is part of the overall design process of a rocket thrust chamber. To this purpose, the prediction of the heat load upon the walls is a crucial and necessary step, that nowadays cannot but be accomplished by means of numerical modeling.

## 2.6 General conduction energy equation

By specializing the first law of thermodynamics to a proper differential control volume in a subject-to-heating medium of thermal conductivity  $k = k(x, y, z)$ , one can derive the general conduction equation (further details in [6]):

$$\frac{\partial}{\partial x} \left( k_x \frac{\partial T}{\partial x} \right) + \frac{\partial}{\partial y} \left( k_y \frac{\partial T}{\partial y} \right) + \frac{\partial}{\partial z} \left( k_z \frac{\partial T}{\partial z} \right) + \ddot{q} = \rho c \left( \frac{\partial T}{\partial t} + V_x \frac{\partial T}{\partial x} + V_y \frac{\partial T}{\partial y} + V_z \frac{\partial T}{\partial z} \right) \quad (2.11)$$

where  $\rho$  is the medium density,  $c$  is the specific heat per unit mass in J/kg-K,  $\ddot{q}$  the internal heat generation per unit volume (e.g. resistance heating in a conductor),  $V = V(x, y, z)$  is the velocity for mass transport of heat. Equation 2.11 requires proper boundary conditions to be specified. It is presumed that the BCs cover the entire body with each condition applied to a portion of the body surface:

1. Specified temperatures acting over surface  $\Sigma_1$ :

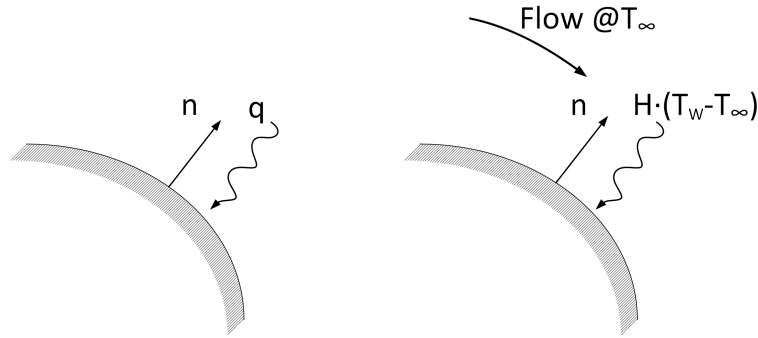


**Figure 2.9:** Boundary conditions for the general conduction equation

$$T = T^* \quad (\text{BC1})$$

2. Specified conductive heat flows acting over surface  $\Sigma_2$  (Fig. 2.9 left):

$$\frac{q}{\Sigma_2} = -k \frac{\partial T}{\partial n} \quad (\text{BC2})$$

3. Specified convective heat flows acting over surface  $\Sigma_3$  (Fig. 2.9 right):

$$\frac{q}{\Sigma_3} = -k \frac{\partial T}{\partial n} = h(T_w - T_\infty) \quad (\text{BC3})$$

The insulated (adiabatic) surface condition is achieved by imposing  $q = 0$  in BC2. Moreover, being the equation time-dependant, an initial condition has to be specified in the form:

$$T = T_0, \quad @ t = 0s \quad (\text{TC})$$

Equation 2.11 represents a versatile resolution tool for a large class of conductive-convective problems, in both steady-state and transient cases. The three fundamental laws of heat transfer (Stefan-Boltzmann's, Newton's, Fourier's) introduced at the end of Chapter 2, can easily be derived themselves from equation 2.11. But analytical solutions aside, when it comes to practical problems, a time and space discretization is required in the attempt to catch a sufficiently accurate numerical solution. In the following sections the basics of numerical heat transfer - with regard only to conduction and convection problems - will be briefly discussed. It is here pointed out that, within the realm of spatial and temporal discretization techniques, we choose to describe and apply to the general conduction equation, the Finite Element Method (FEM) coupled with the Finite Difference Method (FDM). This is a way to "get into" the ANSYS software's logic, the software that will be employed for the successive thermal-mechanical analysis of the engine.

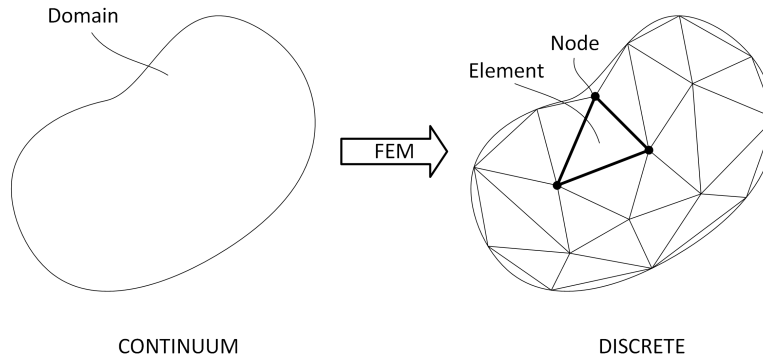


**Figure 2.10:** FEM approach: the solution region is divided into nonoverlapping elements with nodes on vertexes

### 2.6.1 Spatial discretization: the Finite Element Method

*Divide et impera.* This quote is the essence of any discretization method, FEM included. The basic idea is to build a complicated object with simple blocks, or, divide a complicated object into smaller and manageable pieces, referred to as *elements*. So considering a domain for a given problem, the goal is to reduce a continuum problem - which has an infinite number of unknowns - to one with a finite number of unknowns at specified points, referred to as *nodes*, defined on each element. In Fig. 2.10, a sketch of such a process.

Now, on each node is defined an unknown. The type of unknown is a direct consequence of the problem class. So for a structural problem it will be the nodal displacement. In the case of a heat transfer problem we are interested in determining the *nodal temperature*, i.e. a temperature distribution on the whole body. To this purpose, for every single element, the following FE system is defined by discretizing equation 2.11:

$$[C^{(e)}] \{\dot{T}^{(e)}\} + [k^{(e)}] \{T^{(e)}\} = \{f^{(e)}\} \quad (2.12)$$

$[C^{(e)}]$  being the thermal damping square matrix,  $[k^{(e)}]$  the square element conductivity matrix - both  $[C^{(e)}]$  and  $[k^{(e)}]$  accounts for physical properties of the medium, such as specific heat, thermal conductivity and convective coefficients -  $\{T^{(e)}\}$  being the nodal unknown temperatures vector,  $\{f^{(e)}\}$  being the thermal loads - essentially internal heat generation and/or external heat fluxes on the body - vector. The elemental FE systems are then combined into a global one, representing the behaviour of the entire domain:

$$[C^{(g)}] \{\dot{T}^{(g)}\} + [k^{(g)}] \{T^{(e)}\} = \{f^{(g)}\}$$

Solving the resulting set of algebraic equations gives back the temperature distribution on the body. Starting from it one can calculate other thermal quantities of interest (such as amount of heat loss or gained, thermal gradient, thermal fluxes

etc). Let us say  $n$  is the total number of nodes resulting from the FE discretization. Then  $n$  will also be the number of unknowns and in the end the dimension of the square matrices involved. It is clear that the finer the discretization, the higher the number of elements and nodes, the higher the solution accuracy at the cost of heavier calculations. In order to handle high number of unknowns, the above described method has been computer-implemented giving the birth to different commercial FE Analysis softwares, just like ANSYS.

### The FE discretized general conduction equation

From a purely mathematical standpoint what marks the transition to the FE-discretized problem is the reduction of equation 2.11 into a "FE-like" form as in equation 2.12. Such a result is achieved by adopting a variational formulation as a discretization strategy (more details in [6] and [7]), thus obtaining the following:

$$\frac{\partial}{\partial x} \left( k_x \frac{\partial T}{\partial x} \right) + \frac{\partial}{\partial y} \left( k_y \frac{\partial T}{\partial y} \right) + \frac{\partial}{\partial z} \left( k_z \frac{\partial T}{\partial z} \right) + \ddot{q} = \rho c \left( \frac{\partial T}{\partial t} + V_x \frac{\partial T}{\partial x} + V_y \frac{\partial T}{\partial y} + V_z \frac{\partial T}{\partial z} \right)$$

$\Downarrow$  (Variational Formulation)

$$[C^{(e)}] \{\dot{T}^{(e)}\} + [k^{(e)}] \{T^{(e)}\} = \{f^{(e)}\} \quad (2.12FE)$$

Now analyzing each single term in equation 2.12FE:

- $[C^{(e)}] \{\dot{T}^{(e)}\}$  comes from the time-dependant term  $\partial T / \partial t$  in equation 2.11
- the conductivity matrix can be exploded as the sum of:

$$[k^{(e)}] = [k_{mt}^{(e)}] + [k_d^{(e)}] + [k_{cs}^{(e)}]$$

an element mass transport conductivity matrix, an element diffusion conductivity matrix, an element convection surface conductivity matrix

- the thermal loads vector comprises three contributions:

$$\{f^{(e)}\} = \{Q_{mf}^{(e)}\} + \{Q_{cs}^{(e)}\} + \{Q_{hg}^{(e)}\} \quad [W]$$

left-to-right reading, the second member includes an element mass flux vector, an element convection surface heat flow vector and an element heat generation vector

By calculating the global conductivity matrix, the generic FE software solves equation 2.12FE for the assembled system in terms of the nodal temperatures. For the most general case of transient problems a temporal discretization is required in order to map the time history of temperature.

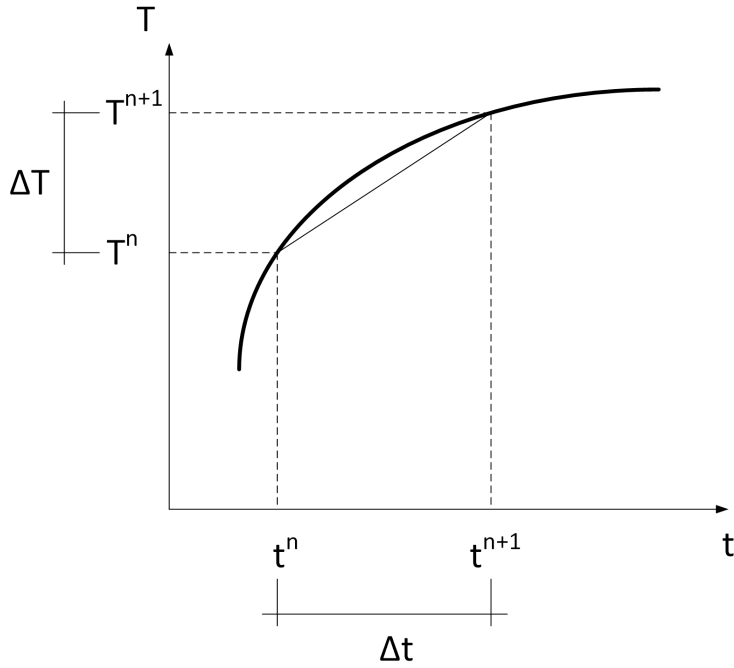


**Figure 2.11:** FDM approach: temperature variation within a time step

### 2.6.2 Temporal discretization: the Finite Difference Method

The FD method is a time-stepping procedure which allows the discretization of the time-dependant term in equation 2.12FE.

Fig. 2.11 shows a model temperature variation in the time domain between the  $n$  and  $(n+1)^{th}$  level. The temperature at the  $(n+1)^{th}$  level can be expressed in terms of a Taylor series:

$$T^{n+1} = T^n + \Delta t \frac{dT^n}{dt} + \frac{\delta t^2}{2} \frac{d^2 T^n}{dt^2} + \dots$$

neglecting second and higher order terms:

$$\frac{dT^n}{dt} \approx \frac{T^{n+1} - T^n}{\Delta t} + \mathcal{O}(\Delta t)$$

introducing a parameter  $\theta$  such that:

$$T^{n+\theta} = \theta T^{n+1} + (1-\theta) T^n$$

then the FE system becomes:

$$[C] \left\{ \frac{T^{n+1} - T^n}{\Delta t} \right\} + [k] \{T\}^{n+\theta} = \{f\}^{n+\theta}$$



$$[C] \left\{ \frac{T^{n+1} - T^n}{\Delta t} \right\} + [k] \{ \theta T^{n+1} + (1 - \theta) T^n \} = \theta \{ f \}^{n+1} + (1 - \theta) \{ f \}^n$$

The above equation can be rearranged as follows:

$$([C] + \theta \Delta T [k]) \{ T \}^{n+1} = ([C] - (1 - \theta) \Delta t [k]) \{ T \}^n + \Delta t \left( \theta \{ f \}^{n+1} + (1 - \theta) \{ f \}^n \right)$$

which gives back the nodal values of temperature at the  $(n + 1)$  time level, given the  $n$  time level values. By varying the  $\theta$  parameter, different time-integration schemes can be set:

- Forward difference method for  $\theta = 0$
- Backward difference method for  $\theta = 1$
- Cranck-Nicolson method for  $\theta = 0.5$

The transient integration parameter  $\theta$  defaults to 0.5 in ANSYS. Further details about equations and solution schemes implemented in the software can be found in Ref. [6].

## 2.7 A roadmap of the verification process

Chapters 1, 2 are intended to introduce the current status of the project and to prepare the ground to successive calculations and models, thus pointing the way to the next major step in the development of the rocket, that is, the verification of the flight model of the engine, which is the subject of the present thesis work. The main goal is to verify that the manufactured flight model, as it is designed, can actually deliver the expected performance when operated. To this purpose a test campaign is envisaged in task #4 from the assignment of tasks. Tasks #1, #2, #3 are preparatory to it. Indeed a design can be labeled as test-verified if certain thresholds in terms of performance and design parameters, as defined by requirements, are met under testing. Here comes the need (task #1 and #2) to understand how to quantify, by means of measurements, the rocket engine parameters introduced earlier in the present chapter. Furthermore in fulfilling task #3, the heat transfer phenomena occurring in the thrust chamber will be modeled and quantified through the equations and methods introduced in the previous section, as implemented in the ANSYS software, thus making possible

a preliminary assessment of their influence on the functioning and the performance of the engine. Once the test campaign takes place, it will be debriefed (task #5) and possible lessons learned will assist in the development of an improved version of the engine (task #6).

With this roadmap in mind, goals are set. Let us proceed further.



## **Part II**

# **Verification of the flight model of the engine**



## Chapter 3

# Rocket characterization through measurements

The envisaged test-campaign on Mira's rocket engine is aimed at validating its flight<sup>1</sup> version, i.e. to verify its design beyond any doubt, thus maximizing the probability that the system will function properly and successfully - meeting the requirements and performing the way it is designed to do- when operated. To this purpose, performance estimation under hot-fire tests is mandatory. This chapter is intended to deal with rocket engine key parameters and their experimental measurements.

### 3.1 Theoretical approach

Table ?? in chapter 1 sets the design parameters the system has been tailored to fit to and is expected to meet. Primary objective of the test campaign is then to verify that no gap exists between predicted and delivered performance. So the problem we are dealing with here is to quantify the performance the system can actually deliver by means of measurements. As a common practice in engineering the problem deserves a preparatory understanding from a theoretical standpoint, addressing simple questions such as: *What* has to be measured? *How* to achieve that specific measurement? Once these questions have been answered, one can eventually formalize a calculation scheme to be eventually engineered in a test stand.

#### 3.1.1 Magnitudes involved

As a first step, let us summarize here all the possible magnitudes involved in a rocket engine characterization through measurements. By simple inspection of

---

<sup>1</sup>It is appropriate to clarify that the adjective *flight* does not imply the engine is "go" for flight, since a series of final integration and acceptance tests represent the last step for the system to achieve the flight readiness status.

formulas 2.1 to 2.6 in Chapter 3, § 3.3, one can gather in the following order:

$F_T$ , Thrust [N]  
 $\dot{m}_p$ , Propellant mass flow rate [kg/s]  
 $u_e$ , Actual exhaust velocity [m/s]  
 $A_e$ , Flow area at nozzle exit [m<sup>2</sup>]  
 $p_e$ , Flow static pressure at nozzle exit [Pa]  
 $p_a$ , Ambient pressure [Pa]  
 $p_c$ , Chamber total pressure [Pa]  
 $A_t$ , Flow area at nozzle throat [m<sup>2</sup>]  
 $g$ , Local value of gravity acceleration [m/s<sup>2</sup>]

Now, only few out of the nine, above-listed magnitudes shall be measured in order to thoroughly characterize a rocket system. First of all since thrust and chamber pressure have been identified as main design parameters, it makes total sense to measure them, so as to verify whether or not their design values are met under test. A measurement of the propellant flow rate shall be performed in order to verify the third design parameter, i.e. the mixture ratio. Furthermore the geometry of the nozzle has been tailored to meet the level of thrust and pressure requested by design, meaning that the exit section and the throat section (therefore the expansion ratio) are frozen. Needless to say the local gravitational acceleration is given. And once thrust is measured, then there is no need for measurements involving pressure and velocity at the exhaust or the ambient pressure. In the end, it turns out that by performing only three measurements, a rocket system is described in terms of the six key-parameters introduced in the previous Chapter. The temperature as measured in the combustion chamber, could also prove useful in characterizing the combustion process as well as the heat transfer from the hot gas to the chamber walls.

### 3.1.2 Rocket engine measurements

Considerations from the previous subsection suggest that four measurements shall be performed in order to characterize a rocket system:

- a force measurement, i.e. thrust
- a mass flow measurement, i.e. propellant mass flow
- a pressure measurement, i.e. chamber pressure
- a temperature measurement, i.e. chamber temperature

It is the purpose of this section to provide a quick, yet comprehensive review about the above mentioned measurements, by discussing in sufficient detail instruments and procedures that have proved satisfactory to perform them.

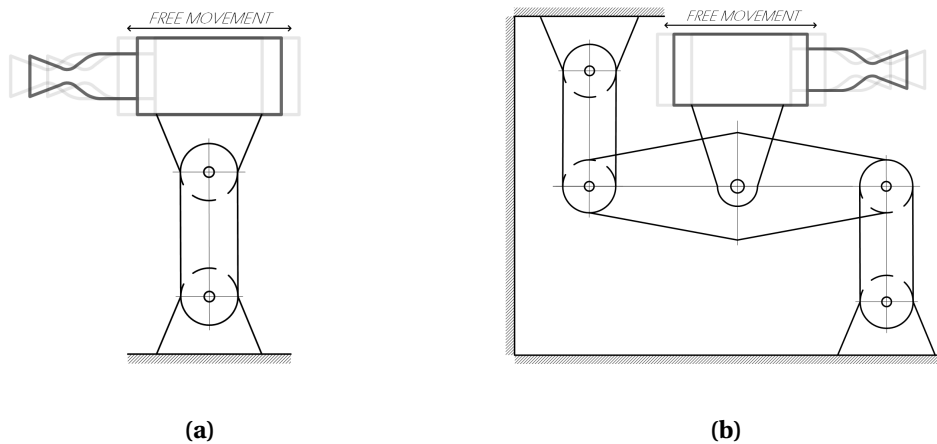


**Figure 3.1:** Pivot mounts

### Thrust measurement

The measurement of a thrust force may be accomplished either by a direct method or an indirect procedure. If the former involves an instrument designed to *directly* respond to this specific stimulus, the latter is arranged to measure one or more thrust-related properties.

**Engine Mount** Whatever the way, is a primary concern to provide the engine with a support connecting it to the instrument in a proper way, since the key to a good measurement lies in minimizing the corresponding error. This especially applies to direct methods where the engine-to-instrument force transmission through contact is the *sine qua non* for the measurement. For an *engine mount* to be properly designed, it is therefore required to:

1. transmit a force being exactly equal to the thrust produced by the engine
2. as a corollary, not introduce additional errors - in need to be calibrated out - beside those associated with the measuring instrument itself

As a first type of mount let us consider the one depicted in Figure 3.1: multiple units of *type (a)* - involving as free from friction as possible pivot points - are arranged in a horizontal bed-like configuration in order to support the engine (an obvious variant is the pendulum mount with the engine suspended from above). The mechanical linkage extending from the ground up to the bed, introduces a vertical downward movement tending to wipe the mount across the thrust pickup instrument, which in turn may transmit troublesome secondary forces in it. In order to eliminate this vertical movement, one can adopt the improved mount of *type (b)*.

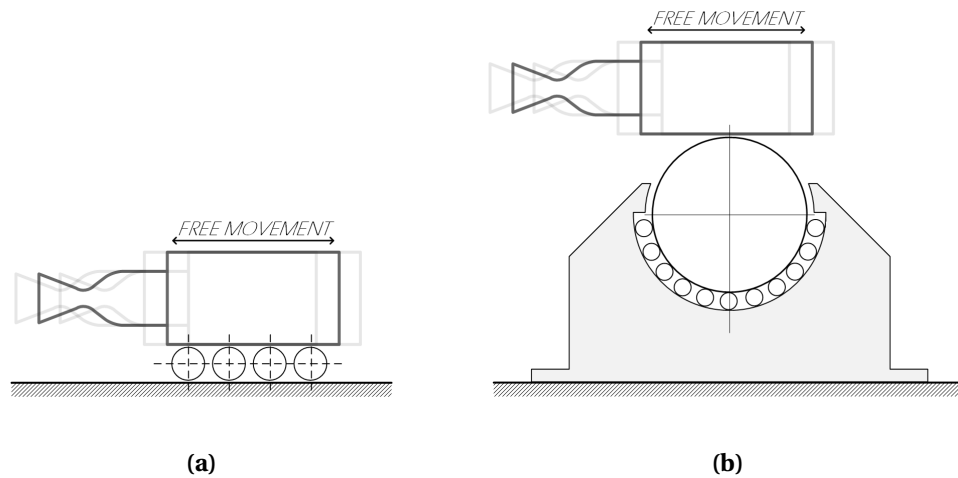


**Figure 3.2:** Ball or roller mounts

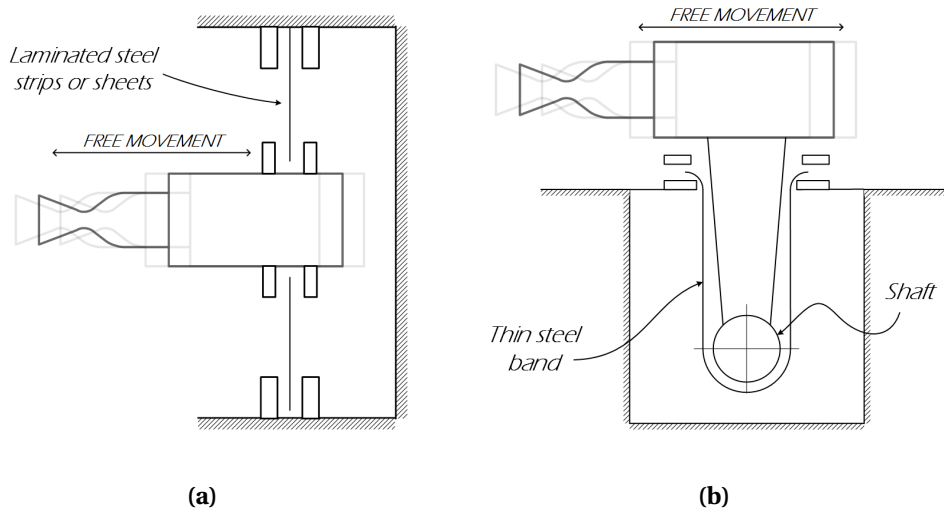
Mechanical linkages can be avoided by the use of suitably guided balls or rollers, as shown in Figure 3.2. Such a configuration is excellent from the friction standpoint, but is practical only for supporting small weights (unless abundantly multiplying the rolling pieces).

Figure 3.3 depicts a couple of flexural or elastic hinge type of mount. It is clear that such a configuration offers resistance to movement, but still it can be considered frictionless in the sense that the resistance force is almost wholly dependant upon the elastic qualities of the hinge, therefore it varies according to a definite physical relation (provided the hinge stresses are within the elastic limit).

One last configuration is sketched in Figure 3.4: the bell crank mount is useful both as a primary mount and as a force-transmitting link. Its value as a transmitting link is due to the magnification or reduction of the force which can be achieved to adapt the engine thrust to the capacity of the particular measuring instrument.

**Direct Measurements** Direct methods for the measurement of thrust involve a transducer, that is, a device that receives a physical stimulus and changes it into another measurable physical quantity through a known relationship. The most common type of force transducer is the strain gauge load cell, which basically converts a force into a measurable electrical output. The gauges themselves are bonded onto a beam or structural member that deforms subjected to the applied load and the resulting strain changes the electrical resistance of the gauges in proportion to the load. Strain gage load cells have become the most widespread of all force measurement transducers.

Beside strain gauge cells, pneumatic load cells are sometimes used where in-



**Figure 3.3:** Flexural mounts

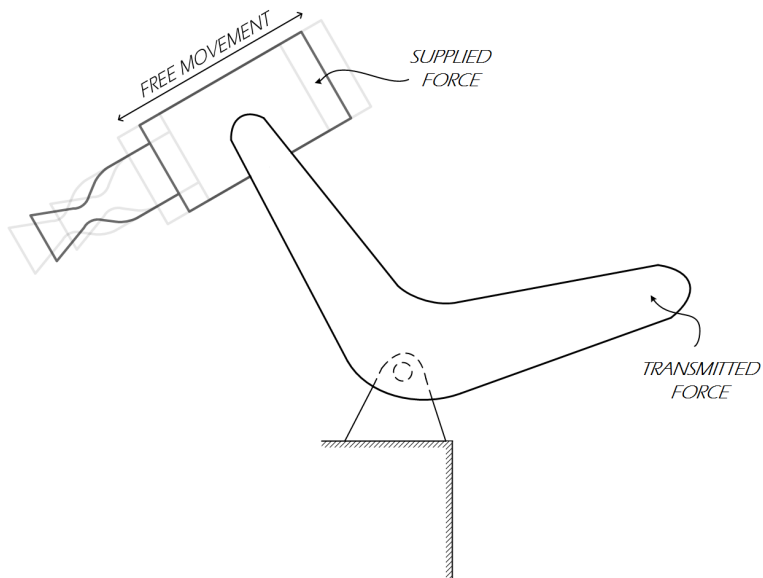


**Figure 3.4:** Bell crank mount

trinsic safety and hygiene are desired, and hydraulic load cells are considered in remote locations, as they do not require a power supply.

**Indirect Measurements** Several methods exist whereby thrust can be estimated without a direct force measurement:

- by simply measuring the chamber pressure and the throat area of the rocket and then applying the isentropic thrust coefficient value appropriate to the nozzle area ratio and the atmospheric pressure involved
- by integration of the static pressure over the whole interior surface of the combustion chamber and nozzle
- by measuring, via optical devices, the velocity of the rocket exhaust gases and simultaneously the mass consumption rate of the available propellant. The thrust is estimated as the product of mass flow and velocity and eventually corrected for a non correct expansion of the gases, by addition of a pressure-thrust term
- thrust could also be estimated from the wavelength of the pattern of standing shock diamonds visible in luminous exhausts

The accuracy of these indirect methods ranges from good to highly approximate.

### **Propellant mass flow measurement**

Mass flow measurements may be accomplished through mass flow meters. The most widely used types of flow meters include differential pressure, thermal mass, and Coriolis devices.

**Differential Pressure Flow Meter** An obstruction (a nozzle, venturi or thin sharp edged orifice) of known diameter is inserted into a region of laminar flow, and fluid pressure measured on each side. Pressure will be higher on the upstream side, with the difference in readings being proportional to the square of the velocity. It follows that if all other factors remain constant, then the pressure differential is proportional to the square of the rate of flow.

**Thermal Mass Flow Meter** These are available in two designs: heated sample tube and inserted probe. Both derive mass from the specific heat capacity of the fluid (thus negating density variations) so this property must be known. In a heated sample tube mass flow meter, some or all of the flow passes through a high precision tube. Heat is applied to the tube and the change in temperature measured. The difference in temperature between the two points indicates how much energy the fluid has absorbed, which depends on the mass moving through the tube.

Inserted probe mass flow meters use the same principle, but with two RTD (resistance temperature detectors) probes positioned in the flow. The upstream sensor measures the fluid temperature while the second is heated to a temperature above that of the first sensor. Heat is transferred from the second sensor to the fluid at a rate corresponding to the mass flowrate.

**Coriolis Flow Meter** Coriolis mass flow meters measure mass through inertia. Liquid or a dense gas flows through a tube which is vibrated by a small actuator. This acceleration produces a measurable twisting force on the tube proportional to the mass. The mass flow rate is indicated without needing any knowledge of the fluid flowing inside. More sophisticated Coriolis meters employ dual curved tubes for higher sensitivity and lower pressure drop.

### Chamber measurements

It is appropriate here to state that chamber measurement targets are static values of pressure and temperature (reservoir conditions can be assumed into the chamber). To this purpose the traditional thermocouple probes and piezoresistive pressure transducers would fit well. The operating principle is basically the same as the load cell previously described, i.e. the conversion of the measured magnitude into an electrical signal:

- In a thermocouple two dissimilar metal wires joined at one end generate a temperature-dependent voltage as a result of the thermoelectric effect
- Pressure applied to the pressure transducer produces a deflection of the diaphragm which introduces strain to the wheatstone-arranged gages. Again the strain will produce an electrical resistance change proportional to the pressure

The state of the art when in need for performing accurate chamber measurements include non-contact devices - primarily optical sensors - all operating on some form of radiative heat transfer measurement: heat can be detected as a radiation emitted from a source, thus resulting in a spectrum from which one can determine the temperature of the source. Different systems work in different spectral regions (the operator can choose among infrared thermometers, camera field devices or fiber optical thermometers, etc).

At any rate the harsh chamber environment pose a demanding challenge since it requires the sensors to be designed in such a manner to withstand the high local pressure and temperature, as well as vibration.

### 3.1.3 From measurements to data

The above mentioned instruments can be arranged into a test stand. Consider the scheme depicted in Fig. 3.5: with the sensor suite properly installed on

the test engine, when a fire test is being run the transducers will produce a voltage signal (eventually to be amplified) as output. A data logger will collect and store these outputs over the firing time. Finally measurement data will be transferred to the Human-Machine-Interface (HMI, essentially a PC) for post-processing. Before proceeding any further some preliminary requirements can be jotted down for the next put-into-practice phase. First and foremost, as already mentioned, the test stand shall provide real-time measurements of the well-known quantities of interest. In addition the test stand shall enable the storage of data for in loco preparative processing. Last but not least the test stand shall allow tests of rocket engines in different regimes of operation, by enabling the variation of parameters such as chamber pressure, mass flow rate and firing time, in such a way to cover and explore as much operational flight envelope as possible according to a *test-like-you-fly* philosophy.

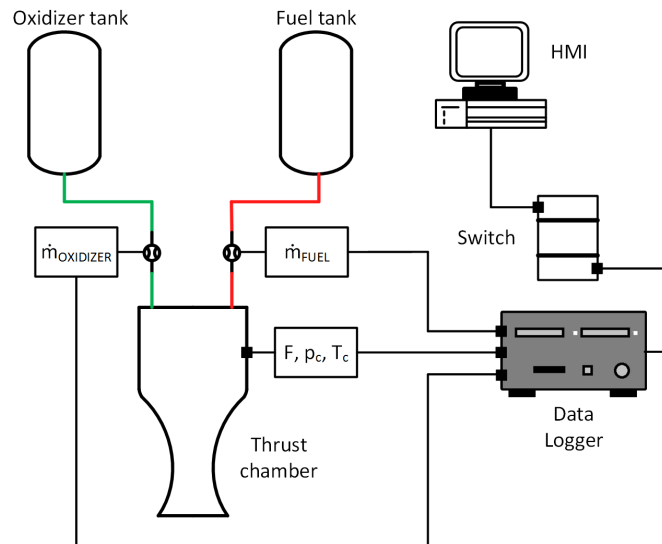


**Figure 3.5:** Basic scheme for data acquisition from sensors

### 3.1.4 From data to results

Once the measured data have been acquired, post-processing can be performed. Consider the calculation scheme presented in Fig. 3.6:

1. Data from mass flow meters allow the calculation of the overall propellant mass flow, as the sum of oxidizer mass flow and fuel mass flow
2. From the load cell data it is possible to trace the thrust behaviour over the burning time
  - Calculation of total (2.5) and specific impulse (2.5.1) as well as effective exhaust velocity (2.6) can be performed

### 3. Pressure transducer gives back chamber pressure readings

- Calculation of characteristic velocity (2.3) can be performed
- Calculation of thrust coefficient (2.2) can be performed

All the six rocket parameters, as delivered by the specific design being under test, are so evaluated.

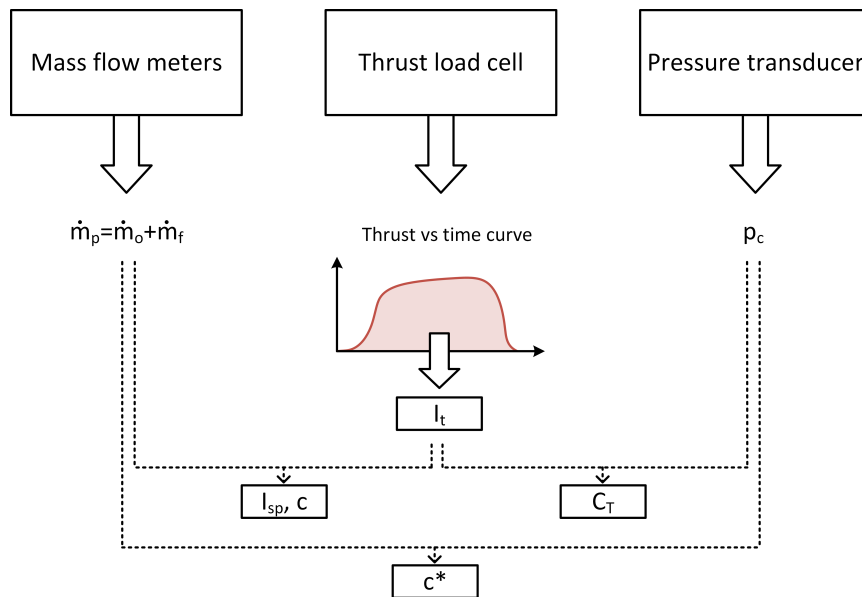


**Figure 3.6:** Calculation scheme: from measured data to rocket parameters

## 3.2 Molding theory into practice: the engine test stand

All the informations so far gathered about rocket measurements laid the ground-work for engineering a test stand, that is, an assembly comprising a mount for supporting the engine along with a sensors suite for data acquisition, aiming at the characterization of the rocket in terms of canonical performance parameters. Before describing the test stand, the selection of appropriate sensors is briefly discussed.

### 3.2.1 Sensors selection

Considering the single magnitude of interest, as seen in subsection 4.1.2 there are different ways to get a measure of it, i.e. different instruments. We want here to discuss the most suitable among them and associate one single instrument to each of the measurements that shall be performed. Our discussion starts with the thrust measurement apparatus by forthwith excluding indirect methods, since they provide the same precision - if not lower - in evaluating the

thrust that can be achieved with well-established direct methods, which besides are more reliable and less expensive. In the wake of this keep-it-simple logic, the bell crank type seems the natural choice for the engine mount. Indeed in order to avoid spurious recording of thrust, the ideal engine mount avoids any friction or other force which restrains its movement in an unpredictable fashion and the single hinge of the bell crank mount helps minimizing the friction. Furthermore it can be used to secure any desired orientation of the engine.

As for the propellant mass flow measurement, of the three methods indicated in the previous section, the Coriolis type is the most accurate as well as highly reliable and low maintenance. The only concern when operating this kind of flow meter is avoidance of bubbles in liquid. Although slightly less precise than the Coriolis type, a differential pressure meter represents a very cost-effective solution. Its no-moving-parts feature makes it simple, rugged and reliable. Thermal mass flow meters are excluded, for they present downsides which make them incompatible with rocket measurements. They need time to reach a steady-state operating temperature. Readings should not be taken as soon as the device is powered-up. But most of all, there is no need to heat up the propellants before their instertion in the injector (this specially applies to the ethanol, being the coolant in the regenerative cooling scheme adopted on the injector plate).

Finally the chamber measurements, namely static temperature and pressure of the hot combustion gases. In this case the harsh chamber environment requires the sensors to be combustion-proof and their operation must be proven feasible not only in terms of survivability, but in ability to pass data with sufficient integrity. Let us suppose we want to employ a direct method - say a thermocouple - for measuring the temperature of the hot gas in the combustion chamber. In order to obtain a correct measurement, the thermocouple must reach a local thermal equilibrium condition with the gas (ideally to this purpose it should have no thermal mass, nor thermal conductivity). Now, typical chamber temperature values estimated in the previous test-campaigns do not drop below 2000K. Considering the fuel-richer mixture ratio envisaged for the flight model of the engine - with a consequent higher combustion temperature - it is unthinkable the application of any of the traditional contact devices in performing the measurement, not only thermocouples. Indeed the gas temperature must be lower than the melting point of the materials of the instrument (not mentioning a possible chemical interaction between the gas and the probe). Currently, no existing device meets this basic requirement. Furthermore one should account for the thermal conductivity of the thermocouple wires as well as its radiative loss, ultimately resulting in a measured temperature cooler than the actual one characterizing the gas within the chamber volume. Then in order to avoid contact with the hot medium being the subject of the measurement, one should look into optical instruments. In this case, even supposing a secure integration of the instrument in the structure, how can the hot gases' spectrum - and only that - be isolated from the surrounding (the combustion flame, the inner graphite surface of the chamber, etc.)? In other words it is impossible to "look" precisely

at the combustion gases in such a small volume, characterized by several not-singularly-detectable emitting sources. What instead represents a clearly visible source of light are the exhaust gases. Then optical instruments could perform a correct measurement of the exhaust temperature and this information - along with the velocity of the exhaust flow and few other parameters of the gases at the exit section of the nozzle - could be used to trace the temperature back to the combustion chamber by applying the one-dimensional isentropic-flow theory. Working the chamber pressure out by means of a direct measurement, represents a feasible task instead and a regular pressure transducer can correctly carry it out. The sensor is not required to directly face the hot combustion gases in order to perform the measurement. It can be installed in a backward location - thus reducing the heat load on it - and the pressure transmission from the chamber to the diaphragm can be achieved by an insulating medium in between them. Quasi-reservoir condition is expected in the combustion chamber with a gas flow reasonably static, thus making insignificant the measurement error possibly introduced by dynamic pressure.

### 3.2.2 Sensors suite

In Figure 3.7 the test stand arrangement is finally presented. The engine will be supported by a bell-crank mount and feed by the propellants flowing from the tanks (housed in the engine rack, not represented in figure) into the engine head. A series of sensors will provide the team with all the necessary data required for the engine characterization in terms of performance. Specifically, the sensors suite comprises:

- 2 × mass flow meters - one per propellant line, particularly a Coriolis type for the oxidizer, an orifice type for the fuel - for the measurement of the propellants' mass flow rate  $\dot{m}_p$
- 1 × force load cell - namely a compression load cell - for the measurement of thrust  $F_T$
- 1 × pressure transducer for the recording of the chamber pressure  $p_c$ . The sensor is installed at the far end of a tube running perpendicularly from the chamber across the whole injector head's thickness and beyond, so as to prevent erroneous pressure readings or any damage due to excessive heat load. The air trapped in the tube as soon as the engine gets started will transmit the pressure from the chamber to the sensor
- 3 × temperature transducers - namely K-type thermocouples - for monitoring the temperature on specific locations of the thrust chamber. In particular, as one can spot in the detailed sketch of the engine,  $T_0$  is measured on the outer surface of the ceramic shell,  $T_6$  and  $T_7$  on the injector head, the former in the back side of the front plate, the latter half way down, 2

mm deeper in the middle of the front plate. No sensor is envisaged for the recording of the chamber temperature, since, as explained in the previous subsection, such a measurement would be more of a challenge

Additional sensors are installed in the engine head - two pressure transducers per propellant to measure the pressure drop across the injector, three temperature transducers to track the temperature change of the ethanol as it flows through the injector head - and will further prove useful in assessing the performance of the engine as well as the thermal load developing under firing condition. Finally, measurement data are collected and stored on a computer, which allows the tuning and real-time monitoring of selected parameters, as well as preliminary data processing through the LabVIEW software.

The engine test stand will then allow the characterization of the rocket engine in terms of delivered performance, a comparison of which with theoretical predictions for the same parameters, will either verify the tested design or activate a redesign process followed by further testing, until the design working point is struck with satisfying margin.

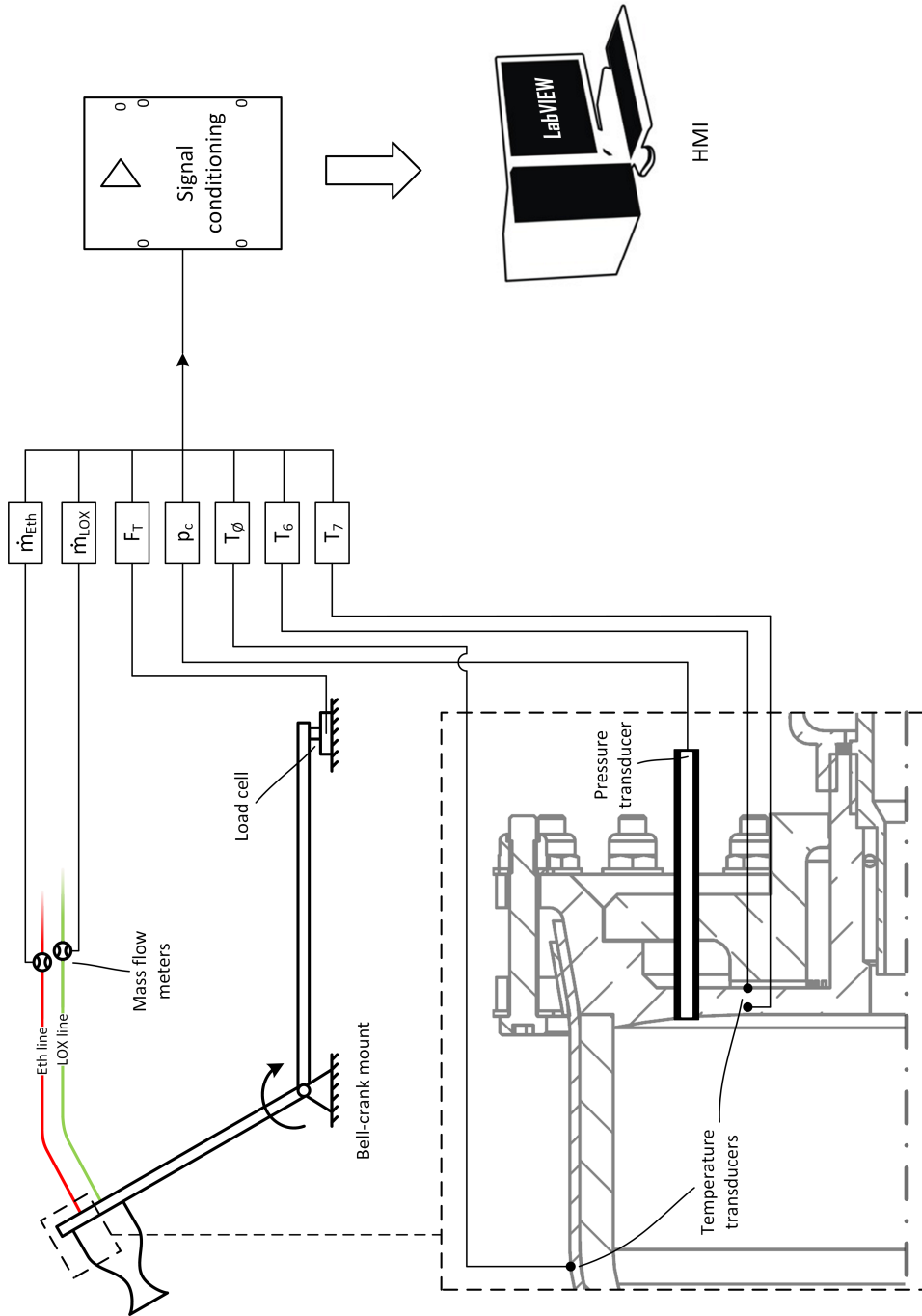


Figure 3.7: Schematic of the test stand



## Chapter 4

# Thermal-mechanical analysis

When dealing with the design of external-loaded systems, it always comes a time when the engineer has to face the prediction of induced loads on the system's structure. That applies to the case of a rocket engine as well. Such a system indeed - in its nature of a combustion and high pressure device - experiences both thermal and mechanical loads and, when operated, whether or not it shall withstand them with no mission compromising, it is up to the ability of estimating the inner-induced stress with sufficient precision so as to properly tailor the structure - in terms of material selection and sizing (always with an eye to the minor-weight criterion when dealing with aerospace systems) - to withstand them. The estimation of thermal-mechanical stress acting upon the thrust chamber, by means of a numerical analysis - to be performed on the FEA software ANSYS - is the subject of the present chapter within the frame of the flight version engine verification.

### 4.1 Focusing the problem

According to the assignement of tasks - Chapter 1, § 1.3 - the purpose of the following numerical analysis is to verify the current rocket's thrust chamber design, that is: for the given geometry and the selected materials, will the engine withstand the thermal and mechanical loads - and the resulting related stresses - without any critical failure? This is the core question we are going to address in this chapter. And the quest for the answer starts from a deeper understanding of the loads the engine is designed to bear.

#### 4.1.1 Thrust chamber: a deeper insight

In Fig. 4.3 a cross-section view of Mira's thrust chamber is presented. The assembly comprises essentially three main axysimmetric pieces - namely an external shell in Oxide-oxide Ceramic Matrix Composite, which houses a graphite inlay with convergent-divergent nozzle-shaped inner contour, plugged back by

a stainless steel injector plate (faceplate + backplate) - fastened and bonded together so as to withstand the operational loads occurring over the 20 s burning time.

As soon as the engine gets started, after a short build-up transient, the thrust action settles to the nominal design value of around 500 N as a result of a pressure distribution along the chamber wall as depicted in the sketch: pressure drops towards the exhaust as the gas flow experiences an expansion. And so does the temperature, thus triggering heat-transfer phenomena across the wall. Detailed sketch 1 in the figure shows the temperature fall due to the combined action of both convective heat fluxes - on the fluid-wall interface - and conductive heat fluxes throughout the wall thickness. Now considering detailed sketch 2, an active cooling strategy has been adopted for cutting down the heat load on the rear part of the faceplate: ethanol from the tank is guided into radial cooling channels, where it gains velocity and removes heat from the plate while rising up its temperature before being injected into the combustion chamber (regenerative cooling scheme). Additional cooling of the injector head is achieved by means of a passive technique involving the propellant cones sprayed out from the swirl injector: the ethanol excess in the fuel-rich propellant mixture allows a wider spray angle with part of the fuel being laid down over the wall where it evaporates, thus realizing a partial heat removal. The adoption of such cooling strategies is of primary importance in the near injector plate zone where the combustion takes place. A further rise in temperature is nearby due to a radiant heat flux moving towards the wall and further heating up the nozzle, net of the absorbed heat which is in turn radiated away in the surrounding air.

So far the following loads have been found to act upon the thrust chamber under nominal functioning conditions:

- mechanical loads
  - thrust force  $F_T$
  - pressure distribution at wall  $p(x)$
  - weight force
  
- thermal loads
  - temperature distribution at wall  $T(x)$
  - heat fluxes due to forced convection  $h_{\text{wall}}, h_{\text{cool}}$
  - heat fluxes due to conduction  $k_{\text{graph}}, k_{\text{OCMC}}, k_{\text{steel}}$
  - heat flux due to radiation  $q_{\text{rad}}$

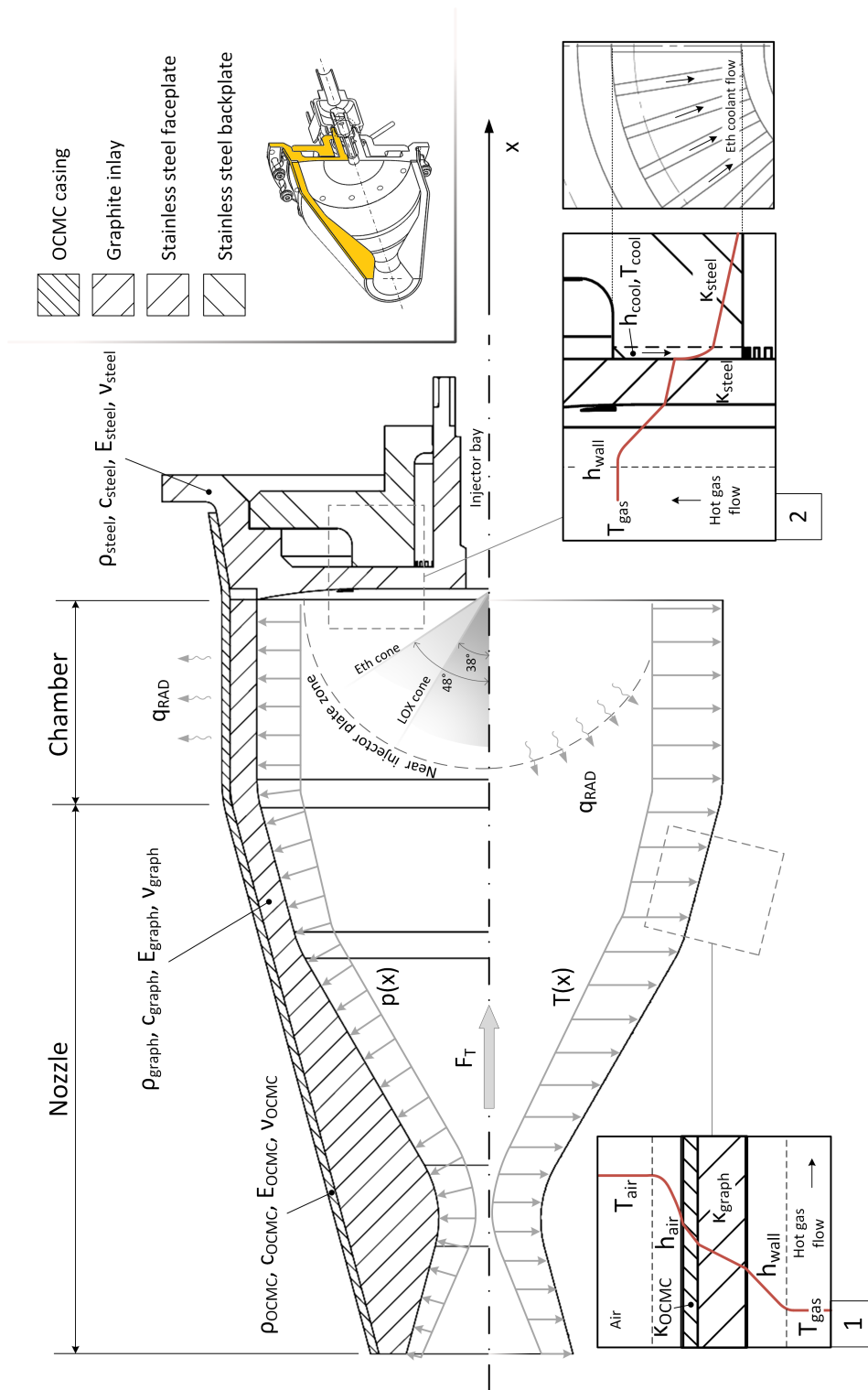
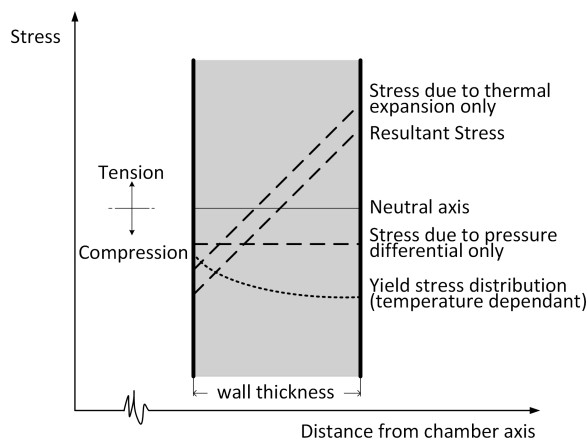


Figure 4.1: Mechanical and thermal loads acting upon a rocket's thrust chamber

Now, before starting a direct attack to the problem, as a wise common practice in engineering, some preliminary reasonable assumptions could simplify the model and the subsequent calculations. Let us start by neglecting thrust, weight and other body forces among the mechanical loads, the contribution of such actions to the total deformation being small. As for the thermal loads, each heat source/sink has a different impact on the total amount of thermal loading. Indeed, the heat transfer inside the thrust chamber is mainly convective in its nature. Heat conduction from the chamber to the rest of the structure can be considered negligible when compared to the convection mechanism at least for the firing duration. The small-surface connections between the injector plate and the rest of the rocket structure, slow down the conduction process: by the time heat flows from side to side throughout the thickness, convection has already taken place upon the wall. Any heat-adding radiative heat flux is cut out, as well as the heat-removing flux radiating from the outer surface of the nozzle, which is not taken into account. The net result of such loads acting in concert upon the wall, is the stress arising in the nozzle materials (see Fig. 4.2). Standing above the others, there is the thermal stress induced by the temperature gradient across the wall. The inner wall surface, adjacent to the hot gas flow, expands more than the wall surface in direct contact with air, thus resulting in compressive stress on the inner side and tensile stress on the outer side. An extra compressive stress, due to the pressure load, is usually small compared to the thermal stress. The last consideration allows to neglect the pressure distribution at wall.

The above simplifications reduce our problem to a thermal-stress analysis. The next step is now to understand how such loads can be treated through the ANSYS software, in order to switch from the problem to a model.



**Figure 4.2:** Typical stresses in a thrust chamber inner wall

**Table 4.1:** Analogy between thermal and structural problem

<b>Thermal</b>	<b>Structural</b>
thermal conductivity	Young's modulus
temperature	displacement
thermal loads	body force loads

## 4.2 From the problem to a model

Recalling the core question from the previous section - about the engine's capability to survive the operational loads - for sure an answer will come from the data given back by the tool employed in carrying out the task, the ANSYS software. And whether or not the answer will be plausible, it depends on the input data the program is fed with. Indeed it is mandatory in such tasks to avoid the *garbage in, garbage out* situation. Therefore, assiduous attention has to be paid to the input data, which in turn can be either the result of preliminary calculations or some ready-to-use data from someone else's work. Long story short, first of all we need some reliable input data. Let us start from working on them in order to build a model for the problem.

### 4.2.1 A brief introduction to ANSYS/thermal

The goal of a thermal analysis is to understand the response and behaviour of a given structure with thermal loading by calculating the temperature distribution and related thermal quantities of interest. To this purpose one can run the ANSYS/thermal program in essentially two modes:

- Steady-State (SS) mode, which aims at finding the temperature distribution when a thermal equilibrium is reached, i.e. under steady-state loading conditions. The program will solve equation 2.12FE where the time-dependent term vanishes under steady-state assumption:

$$[C] \{\dot{T}\} + [k] \{T\} = \{f\} \quad (5.1)$$

- Transient-State (TS) mode, which sets out to determine the temperature time history by solving - in time and space domain as seen in the second chapter - the full FE equation:

$$[C] \{\dot{T}\} + [k] \{T\} = \{f\}$$

Many applications require to run a coupled-field (CF) thermal-structural analysis in order to calculate thermal stresses (that is, structural stresses caused by thermal expansions or contractions). This can be achieved with a *sequential* approach, i.e. by performing two analyses in a row - each belonging to a different

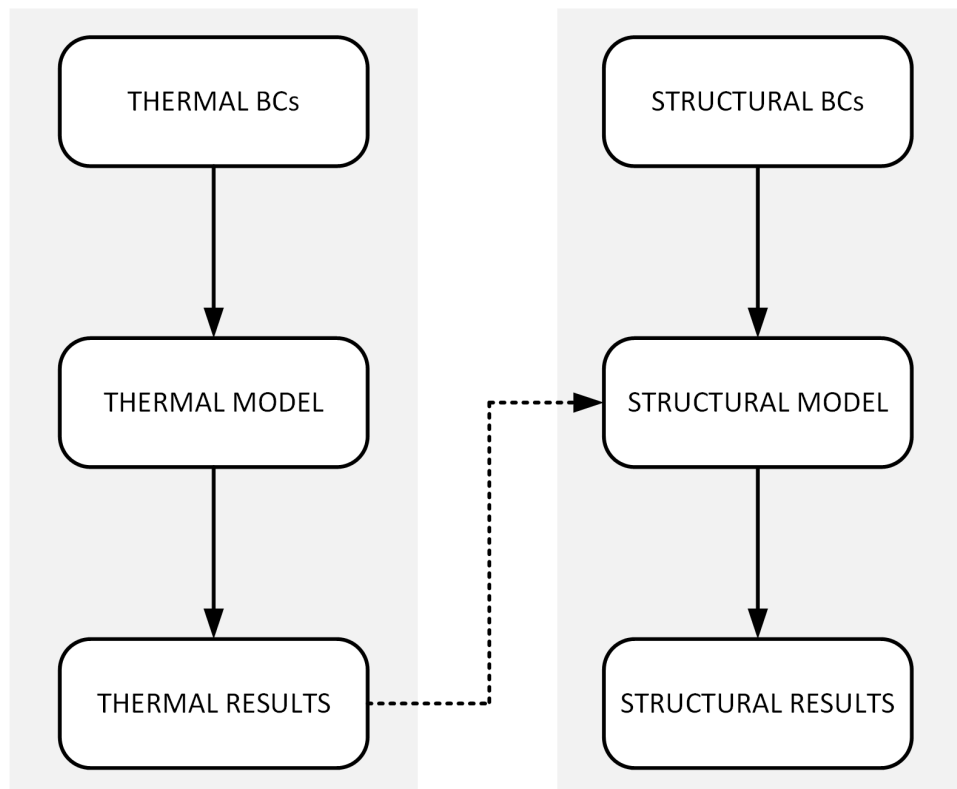


**Figure 4.3:** Sequential coupled-field analysis data flow scheme

field - so as results from the first one to be loads for the second (as sketched in Fig 4.4). In this case, the program solver calculates the temperature distribution from equation 2.12FE and then apply them as "body force" loads in the subsequent structural-stress analysis. The latter in particular is aimed at the solution of the following FE equation:

$$[k] \{u\} = \{f\} \quad (5.2)$$

for the  $u$  unknown, which is the structural displacement or deformation due to - among others - thermal loading. Matrix  $[k]$  is the stiffness matrix. One should notice the similarity between equations 5.1 and 5.2. Indeed they are formally identical - since the results of the same FE discretization process seen in chapter 2 - but still different in the elements that fill up the vectors and the matrices involved, because different is the physics underlying each one of them. Table 4.1 fully clarifies the above mentioned analogy.

#### 4.2.2 Modeling thermal stress with ANSYS

Suppose that the geometry, for a given thermal stress problem, has been split into elements and nodes. Adopting a sequential approach, the ANSYS program will firstly solve the FEM-discretized conduction equation 2.12FE so as to calculate nodal temperatures and then uses the nodal temperatures to obtain other thermal quantities. Equation 2.12FE needs some boundary conditions and thermal properties to be specified. And that is what modeling is about:

- once the thermal conductivity is specified for the medium(s) involved, by assigning a temperature to one or more - say a region - elements/nodes, conduction is modeled
- by specifying the convective coefficient and the bulk fluid temperature on a region, convection is modeled as a surface load
- specific heat and density of the selected material(s) are requested if one is interested in modeling time evolution of thermal quantities of interest

Basically equation 2.12FE is specialized and solved on each region according to local specified boundary conditions and material properties. The same applies to equation 5.2 when the software is called to solve the structural problem:

- besides geometrical characteristics, material properties such as Young's modulus and Poisson's ratio are requested for filling the stiffness matrix
- on a single structural element, and on a region by extension, several types of load - concentrated rather than distributed - can be specified eventually along with displacement constraints as boundary conditions

Finally the following thermal expansion equation represents the interface between thermal and structural analyses:

$$\epsilon_{\text{th}} = \alpha \Delta T \quad (4.1)$$

where  $\Delta T$  is an output from the former and the strain  $\epsilon_{\text{th}}$  is used to determine the thermal contribution to total deformation in the latter. This further clarifies the dataflow scheme in Fig. 4.3.

### 4.2.3 Input data for thermal stress analysis

The previous thrust chamber loads analysis along with the understanding of ANSYS' basic logic behind the modeling of thermal-structural phenomena, make now possible a detailed recognition of the input data required to run a thermal stress analysis, by distinguishing between:

- material properties: thermal conductivity  $\kappa$ , density  $\rho$ , specific heat  $c$ , Young's modulus  $E$ , Poisson's ratio  $\nu$
- boundary conditions: bulk fluid temperature  $T_{\text{gas}}$  and convective heat transfer coefficient  $h_{\text{wall}}$  of the hot gas flow in the nozzle, bulk fluid temperature  $T_{\text{cool}}$  and convective heat transfer coefficient  $h_{\text{cool}}$  of the coolant flow in the faceplate

Among the boundary conditions, further structural displacement constraints will be defined later. Input data are mapped over Fig. 4.1. Let us now move further by piecing together all the information so far gathered into a model statement.

### 4.2.4 Model statement

For the set, in terms of geometry and selected materials, flight version design of the rocket engine's thrust chamber we here choose to perform a one-way sequential thermal-mechanical analysis. Given the axysimmetry of the nozzle assembly it seems a natural choice to run a 2D analysis - symmetrical the geometry, symmetrical the loads, symmetrical the results - in the attempt to strike computational effort savings. This not applies to the injector plate, where the presence of a single sided-ethanol inlet breaks the rotational symmetry. With regard to the material properties, the analysis will be linear, in the sense that it is assumed that they are not affected by temperature variations. The sequence will involve a transient thermal analysis followed by a static structural analysis with proper inputs each. Fig. 4.4 summarizes the model statement.

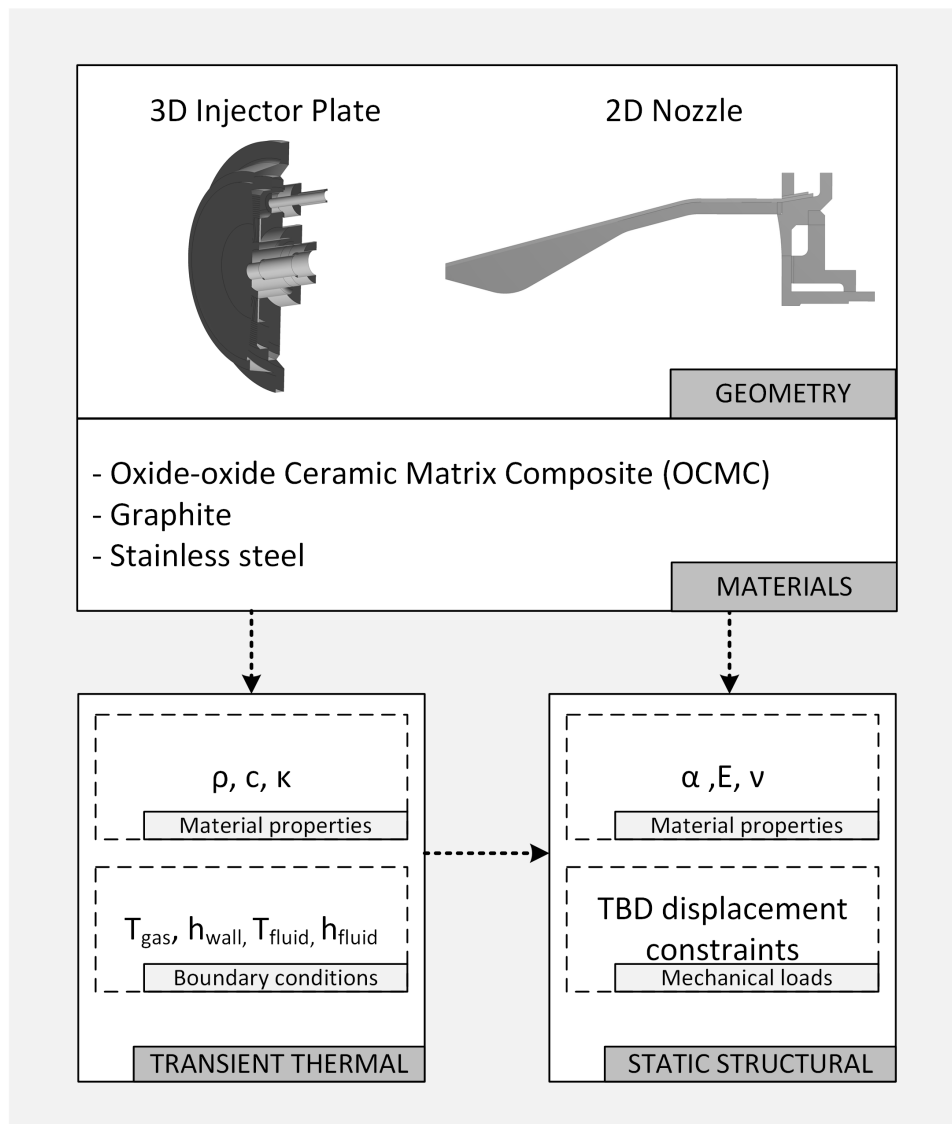


**Figure 4.4:** Thermal-stress analysis model

### 4.3 Preparatory calculations

By the end of this section, adequate values for the requested input data will be collected. We will start with some preliminary considerations on the adopted propellant combination. The characterization of the gas flow through the nozzle will follow. Then the calculation of convective heat transfer coefficients will be performed. Finally the determination of material properties will close the following preparatory phase.

### 4.3.1 Rocket engine design parameters and the CEA tool

In a preliminary design phase of the project, three main design parameters have been identified, that is, thrust, combustion chamber pressure, and oxidizer-to-fuel mixture ratio, along with the selection of a "green" propellant combination considering liquid oxygen as oxidizer and ethanol thinned with water (30% vol) as fuel. Historical data pertaining to similar rocket systems operating on the same propellant combination, oriented the design parameters towards reasonable ranges and eventually generated the following requirements:

- The rocket engine shall produce a thrust of at least 500 N
- The chamber pressure shall be between 1.5 MPa and 2.0 MPa
- The mass ratio oxidizer/fuel (O/F) shall be 1.0 - 1.2

Fire tests so far conducted on the engineering models, attempted to reach a 500 N thrust level, given a 1.5 MPa combustion pressure and a 1.1 mixture ratio. The same chamber pressure and thrust level are envisaged for the flight model, whereas the mixture ratio will be raised. In particular, for a design pressure of 1.5 MPa in the chamber, the LOX/Eth70 combustion reaction has a stoichiometric mixture ratio of  $\sim 1.5$  - to which corresponds the maximum adiabatic flame temperature of  $T_{AF} \sim 3000$  K - and an optimum performance mixture ratio of  $\sim 1.3$ . Considering that in order to put into effect the passive cooling strategy on the injector plate, a fuel rich mixture ratio is required and in order to limit the chamber temperature, the mixture ratio for the flight model has been fixed to a value of 1.2, which is also closer to the maximum performance value (in contrast with  $O/F = 1.1$  so far adopted for the engineering models). Higher values would potentially push the chamber temperature far beyond the materials' limit, unless some additional cooling strategy is adopted. Now given the LOX/Eth70 propellants,  $p_c = 1.5$  MPa - achieved through the combustion of  $\dot{m}_p = 0.25$  Kg/s of propellants at  $O/F = 1.2$  - and some geometrical features of the chamber - namely the expansion area ratio  $\epsilon = A_e/A_t$  (adjusted to a 2.8 value so as to realize the design thrust-level of 500 N) and the contraction area ratio  $A_c/A_t = 22.3$  - it is possible to estimate additional engine parameters through the Chemical Equilibrium with Application (CEA) tool, provided free and open source by NASA. Applications include, among the others, assigned thermodynamic states and theoretical rocket performance. Table 4.2 gathers the engine's design parameters along with theoretical performance as outputted by the CEA tool, while Fig. 4.5 compares the flight model to the previous design in terms of specific impulse and adiabatic temperature in the combustion chamber.

The CEA tool will be useful in monitoring the nozzle flow's thermophysical parameters, in particular their evolution through the expansion. These values will come in handy in the characterization of the heat exchange processes in the thrust chamber.

Parameter	Value
Propellant combination	LOX/Eth70
$F_T$ @sl [N]	510
$p_c$ [MPa]	1.5
$O/F$ [-]	1.2
$\dot{m}_p$ [Kg/s]	0.25
$\epsilon = A_e/A_t$ [-]	2.78
$A_c/A_t$ [-]	22.29
$T_c$ [K]	2913
$I_{sp}$ [s]	225

**Table 4.2:** Flight model's parameters and estimated performance

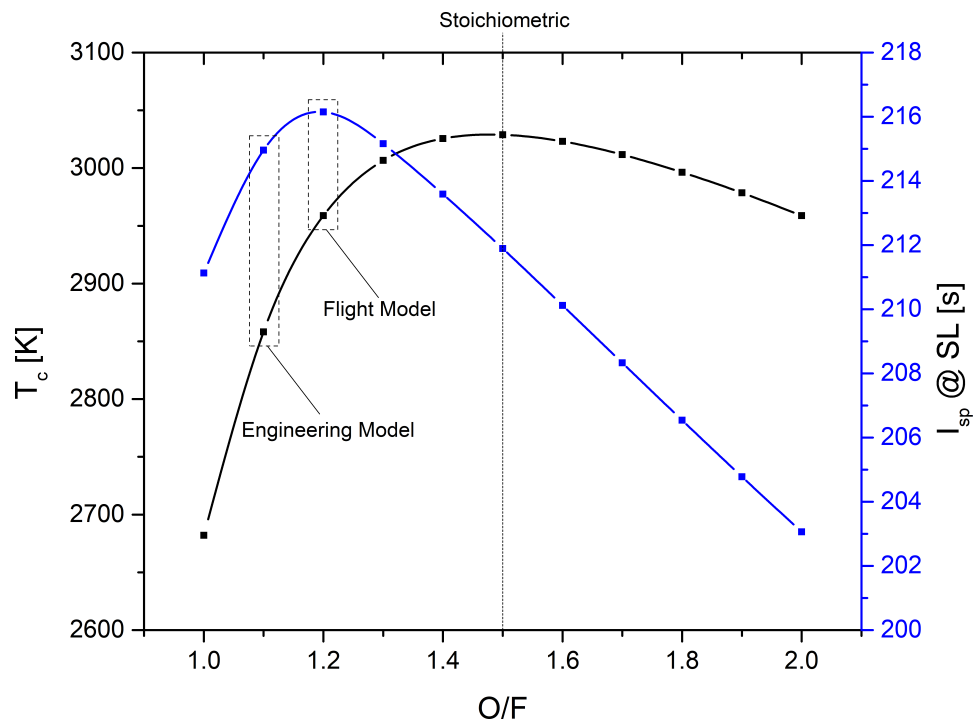


**Figure 4.5:** Chamber temperature and specific impulse vs propellant mixture ratio for the LOX/Eth70 propellant combination

### 4.3.2 The ideal rocket model

As a common and accepted practice in rocket engineering, the subsequent calculations will be performed under the adoption of the ideal rocket model, which comprises a series of reasonable equation-simplifying assumptions, thus easing calculations without compromising precision, since the distance from reality can be quantified in a 1% to 6% margin of error. Sutton[1] expresses the ideal rocket model in terms of the following list of assumptions:

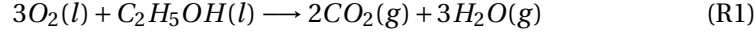
1. The working substance (or chemical reaction products) is homogeneous.
2. All the species of the working fluid are gaseous. Any condensed phases (liquid or solid) add a negligible amount to the total mass.
3. The working substance obeys the perfect gas law.
4. There is no heat transfer across the rocket walls; therefore, the flow is adiabatic.
5. There is no appreciable friction and all boundary layer effects are neglected.
6. There are no shock waves or discontinuities in the nozzle flow.
7. The propellant flow is steady and constant. The expansion of the working fluid is uniform and steady, without vibration. Transient effects (i.e., startup and shutdown) are of very short duration and may be neglected.
8. All exhaust gases leaving the rocket have an axially directed velocity.
9. The gas velocity, pressure, temperature, and density are all uniform across any section normal to the nozzle axis.
10. Chemical equilibrium is established within the rocket chamber and the gas composition does not change in the nozzle (frozen flow).

The ten above mentioned assumptions, are key assumptions for the NASA CEA code as well, which constitutes our main tool for the rocket performance assessment. Now everything is set so as to move on and start the determination of the requested input data. The analysis of the combustion process, represents the first step towards the goal of running the thermal-mechanical analysis of the engine.

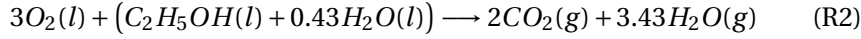
### 4.3.3 Chemical analysis of the LOX/Eth70 combustion

It is the purpose of this subsection to write down the correct combustion reaction for the propellant combination LOX/Eth70, and characterize it in terms of magnitudes of interest that will prove useful in the subsequent calculations. The combustion process involves liquid oxygen as the oxidizer reacting with a

solution of ethanol thinned with water as the fuel. Let us start by the combustion reaction of pure ethanol with oxygen:



The reaction is perfectly balanced. Now, Eth70 is an ethanol/water formulation with a concentration of 70% in alcohol. A simple proportion allows to assert that 0.43 moles of water has to be added on both sides of the reaction so as to get the LOX/Eth70 combustion reaction without unbalancing it:



Precisely, the one above written is the stoichiometric LOX/Eth70 combustion reaction, meaning the one where the reactants are in such a ratio that they are all consumed, i.e. none remains afterwards. The corresponding stoichiometric oxidizer-to-fuel mixture ratio is:

$$\begin{aligned} (O/F)_{St} &= \frac{n_{O_2} \times \mathcal{M}_{O_2}}{n_{Eth70} \times \mathcal{M}_{Eth70}} = \\ &= \frac{3 \times 2 \times 15.999}{1 \times 64.084} = \\ &\simeq 1.5 \end{aligned}$$

where  $n$  and  $\mathcal{M}$ , are moles and molecular weight of each compound, respectively. A 1.2 design mixture ratio is actually prescribed by requirements for the flight version injector plate. That means the final reaction must be rebalanced in terms of the 1.2 mixture ratio. In doing so, we estimate the amount of reactants in terms of moles number and then let the CEA code calculate the amount of products. Indeed, for the sake of precision, it would be too simplistic to keep including only water vapor and carbon dioxide on the reactants' side. An attempt has been done to manually compute the adiabatic flame temperature for reaction R2. The iterative trial-and-error procedure resulted in a  $\simeq 4000K$  value, definitely an overestimation. In [10] the same problematic is pointed out by considering the LOX/LH2 reaction occurring in the SSME. The conclusion is that one cannot simply exclude species such as  $H_2$ ,  $H$ ,  $O$ , etc., from the products. Dissociation into minor species plays a significant role in lowering the adiabatic flame temperature down to the actual value expected within the chamber. In the end, computer-assisted chemical analysis is mandatory.

The following equations allow to calculate the mass flow rates for each propellant, both in stoichiometric and on-design condition:

$$\begin{cases} O/F = \frac{\dot{m}_O}{\dot{m}_F} \\ \dot{m}_O + \dot{m}_F = 0.25 \end{cases}$$

where the second equation originates from requirement PR-3100-FP-AM-008 in [8], which sets the total propellant mass flow to a 250 g/s design value. Then,

again by proportion, one can determine the exact grams of fuel and oxidizer corresponding to the design mixture ratio:

$$\begin{cases} O/F = 1.2 \\ m_O = 87.290544 \text{ g} \rightarrow \% \text{oxidizer} = 54.56 \\ m_F = 72.799424 \text{ g} \rightarrow \% \text{fuel} = 45.44 \end{cases}$$

finally, the correct moles for each reactant in the final combustion reaction are obtained from the following system of equations:

$$\begin{cases} n_{O_2} \times 2 \times 15.999 = 81.5949 \\ \frac{n_{O_2} \times 2 \times 15.999}{n_{\text{Eth}70} \times 64.084} = 1.2 \end{cases}$$

Solving for  $n_{O_2}, n_{\text{Eth}70}$ , the final reaction follows as:



Now the above calculated mole fractions along with the chamber pressure, contraction ratio, expansion ratio and mixture ratio at the design point (see Table 4.2) represent the input parameters for the CEA program. Shifting equilibrium in the nozzle flow has been adopted, thus cancelling hypothesis number ten from the ideal rocket model statement. This implies a higher estimated performance due to the recovery of part of the chemical energy freed in the decomposition of complex molecular species in the chamber (a kind of afterburning effect). Table 4.3 shows the results, units consistent with SI system. The very high contraction ratio, i.e. the wide chamber with a cross section larger than the throat area by a 23 factor, implies a small pressure drop along the chamber, so that few energy is required to accelerate the gas. The Mach number's rise along with temperature, pressure and density drops are indicative of an expansion taking place as the gas flows through the nozzle. The Prandtl number's values are within the typical range for gases. In particular their less-than-unit values indicate a general dominance of thermal diffusivity over viscous diffusion rate, although it slightly increases due to the velocity gain of the expanding flow. As for the other thermodynamic and transport properties, suffice it to say that numbers are coherent with what expected from a rocket engine combustion gas. In the obtained gas mixture, major components are water vapor, carbon monoxide and dioxide, as well as gaseous hydrogen. The first three are known to actively and substantially participate in radiative heat transfer within the chamber.

Now since Mach number's values are outputted for only four stations along the nozzle - namely injector head, combustor end, throat and exit - a nozzle flow study is required in order to make a denser distribution available for the subsequent calculations.

**Table 4.3:** Calculated parameters for LOX/Eth70 propellants, Mira rocket engine

Location	<i>Parameters</i>			Exit
	Injector face	Comb. end	Throat	
$p_{inj}/p$	1.0	1.0008	1.7507	1.3406
$\gamma$ (spec. heat ratio)	1.1531	1.1531	1.1635	1.204
$M$ (Mach number)	0	0.02675	1	2.3091
$T$ (temperature)	2913.3	2913.14	2693.14	1869.51
$p$ (pressure)	15	14.994	8.575	1.094
$\rho$ (density)	1.331	1.3306	1.8232	0.1513
$R$ (spec. gas constant)	386.8	386.8	384.43	381.34
$C_p$ (spec. heat)	3783.5	3783.3	3232.1	3273.7
$\mu$ (dyn. viscosity)	$9.6431 \cdot 10^{-5}$	$9.6427 \cdot 10^{-5}$	$9.1793 \cdot 10^{-5}$	$7.3537 \cdot 10^{-5}$
$\kappa$ (th. conductivity)	0.70201	0.70195	0.5334	0.25890
$\mathcal{M}$ (mol. weight)	21.495	21.495	21.627	21.802
	<i>Mole fractions of gas mixture</i>			
CO	0.23588	0.23587	0.23243	0.21370
CO <sub>2</sub>	0.12711	0.12711	0.13280	0.15449
H	0.01096	0.01096	0.00736	0.00055
H <sub>2</sub>	0.12472	0.12473	0.12721	0.14720
H <sub>2</sub> O	0.48514	0.48514	0.49143	0.48386
O	0.00072	0.00072	0.00027	0.00000
OH	0.01435	0.01435	0.00808	0.00020
O <sub>2</sub>	0.00111	0.00111	0.00042	0.00000

#### 4.3.4 Convergent-divergent nozzle flow study

The ideal rocket assumptions make possible to study the nozzle flow in isentropic, quasi-one-dimensional theory. In particular, as seen in Chapter 2, the isentropic nozzle flow equations allow to analyze the flow evolution from chamber to exhaust in terms of Mach number and static temperature, pressure and density:

$$\left(\frac{A}{A_t}\right)^2 = \frac{1}{M^2} \left[ \frac{2}{\gamma+1} \left( 1 + \frac{\gamma-1}{2} M^2 \right) \right]^{\frac{\gamma+1}{\gamma-1}} \quad (3.7)$$

$$T = T_c \left[ 1 + \frac{\gamma-1}{2} M^2 \right]^{-1} \quad (3.8)$$

$$p = p_c \left[ 1 + \frac{\gamma-1}{2} M^2 \right]^{-\frac{\gamma}{\gamma-1}} \quad (3.9)$$

$$\rho = \rho_c \left[ 1 + \frac{\gamma-1}{2} M^2 \right]^{-\frac{1}{\gamma-1}} \quad (3.10)$$

Indeed for a given spot along the nozzle, defined in terms of the local area ratio  $(A/A_t)^2$  (derived by direct exportation from the CAD model of the nozzle), equation 3.7 gives back the local Mach number when trial-and-error solved. Chamber values of temperature, pressure and density are known from the CEA tool as well as the local specific heat ratio  $\gamma$ . Equations 2.8, 2.9, 2.10 finally result in local nozzle flow characterization in terms of temperature, pressure, density. In this way, the flow evolution is mapped over a single dimensionless nozzle coordinate  $x/L_n$  as shown in Fig. 4.6:

- the Mach number increases the way it is meant to for a convergent-divergent nozzle, from subsonic in combustion chamber to supersonic at exhaust, passing the sonic condition at throat
- temperature, pressure and density all decrease since an expansion is occurring through the nozzle

It is pointed out that, in order to locally describe the flow in terms of the above mentioned magnitudes, a nozzle contour discretization - see Fig. 4.7 where each point has been marked by a vertical bar so as to ease the graph interpretation - has been performed. A total of 178 nodes has been employed in two different, yet equally spaced each, distributions. The nozzle contour is limited by nodes 1 at chamber starting and 178 at nozzle exit, with convergent-starting node 23 and throat node 106 in between. From a section slightly upstream of the throat throughout the divergent sections - nodes 78 to 178 - it seemed appropriate to adopt a denser spacing, since the near-throat area is the most sensitive region, where the flow is transonic and the maximum heating is expected according to

experimental data. As already mentioned in the previous subsection, CEA provides the user with specific heat ratio's values only at nodes 1, 23, 106, 178, so a linear variations has been imposed for the nodes in between.

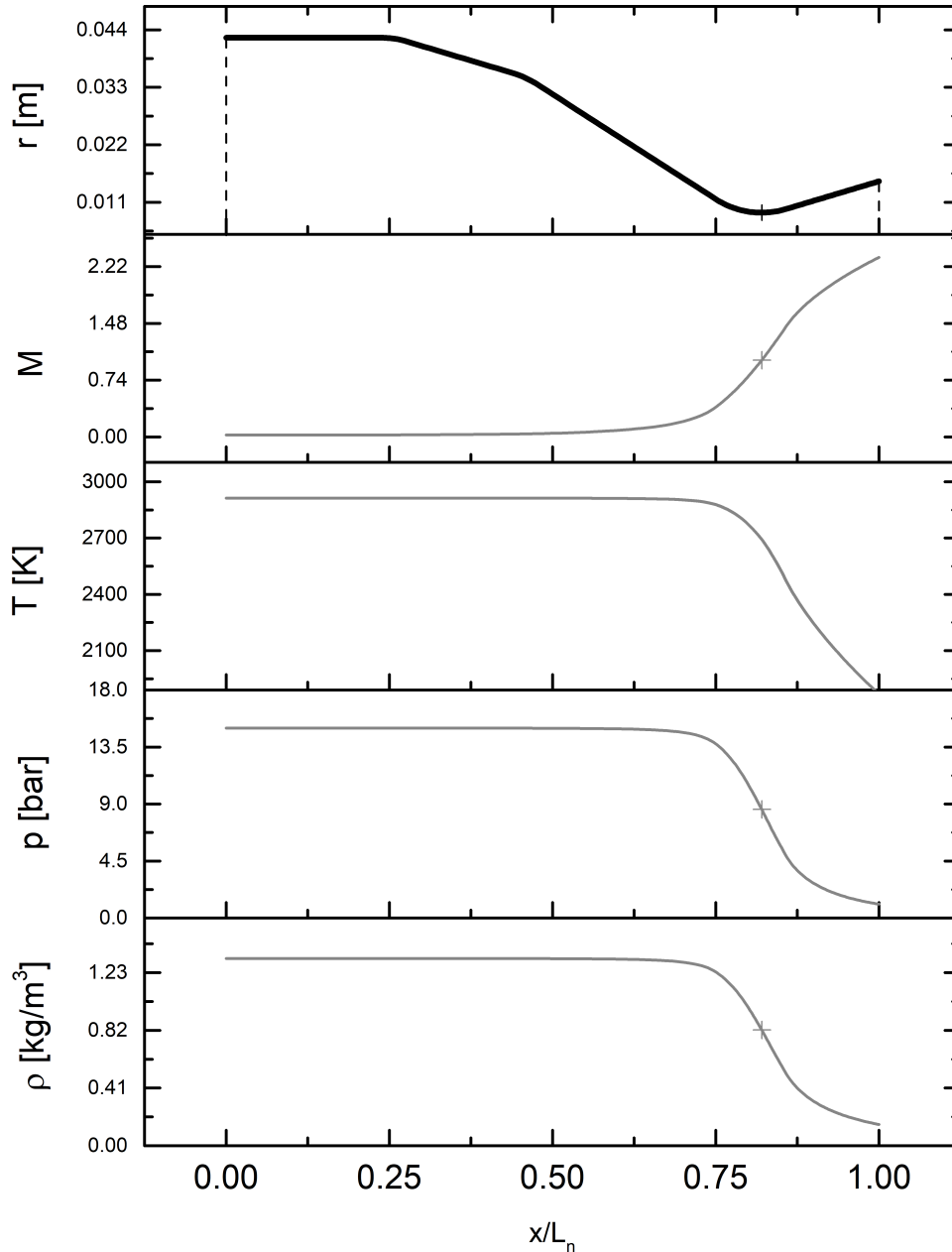


**Figure 4.6:** Characteristics of the isentropic expansion through the nozzle

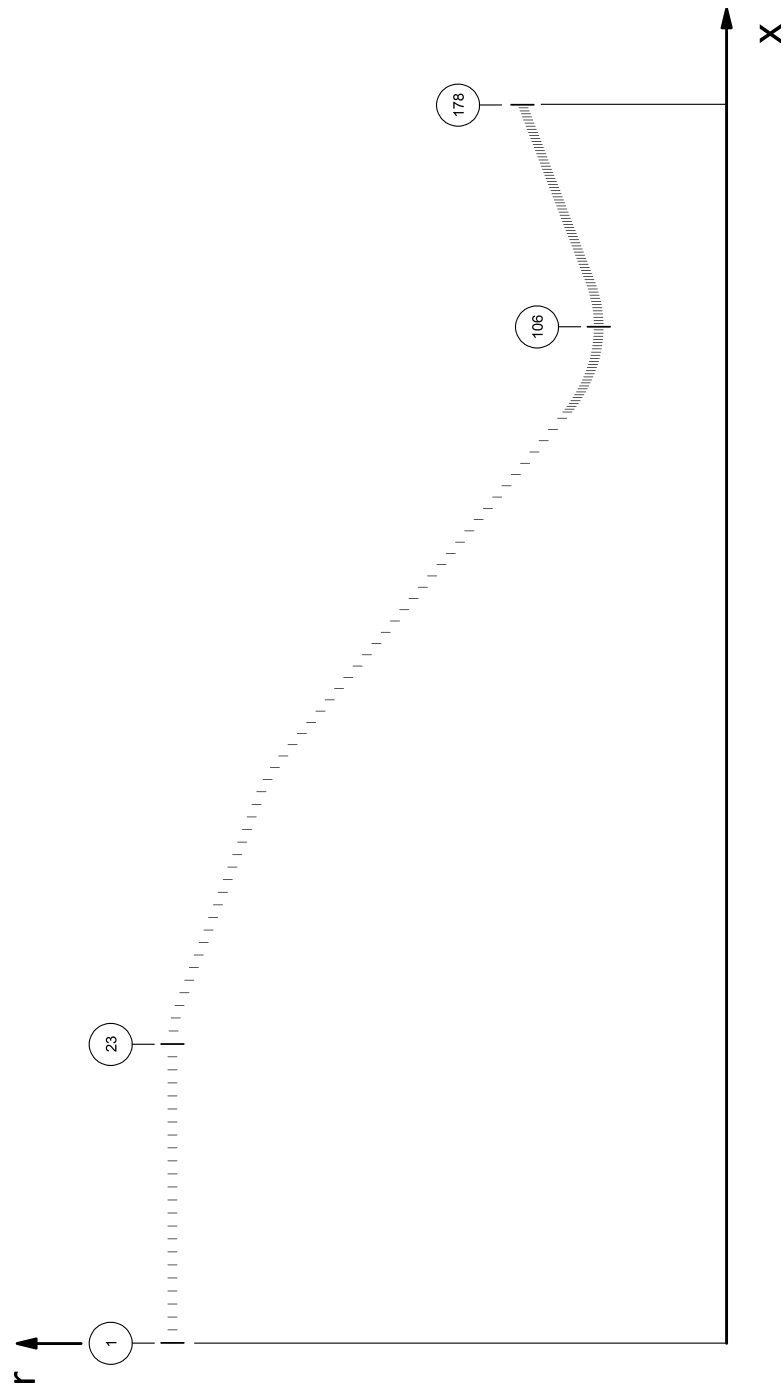


**Figure 4.7:** Nozzle contour discretization

#### 4.3.5 Convective heat-transfer coefficients determination

It has been already mentioned that in a rocket thrust chamber the majority of the heat is transferred by forced convection, from the hot gas flow to the chamber wall. Now in order to quantify that 'majority of heat', a proper formula has to be picked in the vast realm of convective heat-transfer correlations. There are plenty indeed of heat-transfer handbooks and papers, filled with experimental data as well as formulas for the heat-transfer coefficients determination, suited for each situation and practical problem. Provided that the convective heat transfer is of the forced type in a thrust chamber, one must take into account the flow characteristics - e.g. whether it is turbulent or laminar - and the geometry features of the case, when in quest of a proper correlation. So let us get started by distinguishing between the nozzle assembly, where a quasi-isentropic hot gas mixture flows in the axial direction after being generated in the combustion chamber, and the injector faceplate (plus the near injector portion of the chamber) that features burning combustion gases flowing in the radial direction, against the thermal load of which the chamber is partially shielded by the wider cone of ethanol in excess, as described previously in subsection 5.1.1. Different the geometry and the flow nature in the nozzle and the injector plate, different the approaches in the calculation of the heat-transfer coefficients, as in the following subsections.

##### Convection in the nozzle modeling

Historically, the early methods for predicting convective heat-transfer coefficients in convergent-divergent nozzles were based on the assumption of turbulent boundary layer. Anyone who is familiar with nozzle theory and fundamentals of boundary layer, would firmly assert that the above mentioned assumption is debatable. For a given nozzle geometry, one cannot simply infer about the boundary layer nature without having at least a term of comparison - e.g. a similar rocket engine - or in the best case, experimental data for the given geometry to base his conclusions on. Once the boundary layer is established across the nozzle wall, it grows until it separates somewhere in the divergent portion, downstream of the near throat zone. And what happens in between, as far as the boundary layer nature is concerned, is barely predictable: boundary layer could stay the same throughout the nozzle or could evolve, at least one time, from turbulent to laminar or backwards. Then, why basing heat transfer coefficients calculation on turbulent flow assumption? Probably because of the good correlation between turbulent-theory based predictions and experimental data, at the time when rocket heat transfer analysis was moving its first steps. Worst case scenario in fact, the coefficients were overestimated with those turbulent methods being labeled as conservative. Bartz [11] among the others, in 1957 presented in his own words "*a simple, yet reasonably accurate, approximation equation for making rapid preliminary estimates of the convective heat transfer*

*coefficients in rocket nozzles*". Let the Bartz method be the starting point.

**The Bartz method** Based on turbulent boundary-layer assumption, the Bartz equation has become a milestone in nozzle heat transfer analysis, to the extent that survives nowadays in many rocketry literature must-have textbooks ([1] and [3], to name just a couple) as the first preliminary step towards heat transfer coefficients estimation.

Under the inference of turbulent boundary layer, Bartz affirms that the experience until then gained, suggested that the mass flow rate per unit area is the most influential factor on heat transfer coefficient values and then gets to the following formula:

$$h = \left[ \frac{0.0026}{D_t^{0.2}} \left( \frac{\mu^{0.2} C_p}{Pr^{0.6}} \right)_c \left( \frac{p_c g}{c^*} \right) \left( \frac{D_t}{(r_c)_t} \right)^{0.1} \right] \left( \frac{A_t}{A} \right)^{0.9} \sigma \quad (5.8)$$

where  $D_t$  is the throat diameter,  $g$  the gravitational acceleration,  $(r_c)_t$  the throat radius of curvature,  $\mu$ ,  $C_p$ ,  $Pr$ , the dynamic viscosity, the specific heat at constant pressure, the Prandtl number respectively, evaluated at chamber station. As for the rightmost factor  $\sigma$ , it corrects for property variations across the boundary layer:

$$\sigma = \frac{1}{\left[ \frac{1}{2} \frac{T_w}{T_c} \left( 1 + \frac{\gamma-1}{2} M^2 \right) + \frac{1}{2} \right]^{0.8-\omega/5} \left[ 1 + \frac{\gamma-1}{2} M^2 \right]^{\omega/5}} \quad (5.9)$$

$T_w$  is the gas-side wall temperature. It is underlined that the Bartz formula, as it here appears, is consistent with the USC system of units. It is worth noting that the factor in the square brackets - which, for the sake of brevity, we will indicate as the Bartz' constant  $K_{\text{Bartz}}$  - is a constant throughout a nozzle, leaving only  $A_t/A$  and  $\sigma$  to be evaluated at each station. For the case of our nozzle,  $D_t$  and  $(r_c)_t$  can be exported from CAD models, the gravitational acceleration is set to the local value of 32.2019 fps<sup>2</sup>,  $p_c = 1.5$  MPa is a design parameter,  $c^*$  is given back by the CEA tool. Finally Bartz himself suggests the following relations to get a reasonable estimation of the Prandtl number and the dynamic viscosity of the gas mixtures:

$$Pr = \frac{4\gamma}{9\gamma - 1}$$

$$\mu = 46.6 \cdot 10^{-10} \mathcal{M}^{1/2} T_c^{0.6}$$

where  $\gamma$  and  $T_c$  are CEA outputs, while the average molecular mass  $\mathcal{M}$  is calculated as follows:

$$\mathcal{M} = \frac{\sum n_i \mathcal{M}_i}{\sum n_i}$$

with moles number  $n_i$  and molecular weight  $\mathcal{M}_i$  of the single gas-mixture component, readily available from the chemical analysis of the LOX/Eth70 combustion reaction in subsection 5.3.3. Finally the value of the Bartz' constant amounts to:

$$K_{\text{Bartz}} = 0.0015 \text{ Btu/in}^2\text{-sec-F}^\circ = 4418 \text{ W/m}^2\text{-K}$$

Now given the nozzle contour discretization of Fig. 4.7, the Bartz method can be readily code-implemented. What is left uncalculated are the factors  $A_t/A(i) = r_t^2/r(i)^2$  and  $\sigma(i)$  on the  $i$ -th station. Nozzle CAD drawings provide the local radius for the calculation of the former, while the latter is calculated by equation 5.9, where values for  $\gamma$  comes from the CEA model at stations 1, 23, 106, 178 with imposed linear variation on the nodes in between; Mach number  $M$  values are taken from the nozzle flow study in subsection 3.3.4, and the temperature ratio  $T_w/T_c$  is set to one, in a worst-case scenario approach (that is, no temperature drop across the thermal boundary layer upon the wall).

So basically, the Bartz method consists in a three-factors formula, where the constant  $K_{\text{Bartz}}$  is mitigated or amplified at each station - depending on the values of  $A_t/A(i)$  and  $\sigma(i)$  - thus resulting in a heat transfer coefficients distribution along the nozzle. One can notice that, the other parameters being equal, smaller diameters lead to larger heat fluxes ( $h \propto R(i)^{-0.9}$ ), with the maximum heat flux occurring at throat. Fig. 4.8 presents the heat transfer coefficients distribution as calculated with the Bartz method. The graph features a double vertical axis. Indeed a USC system-consistent scale has been added to the SI scale, so as to compare the obtained values for the heat transfer coefficients with those presented by Bartz in [11] for a specific nozzle, as shown in Table 4.4. Both the order of magnitude and the numerical values seem in good agreement, although the geometry features and thermodynamic and transport properties of the flow differ from one nozzle to the other. Not to loosing sight of the final goal, it is natural to question the plausibility of the results in the perspective of the nozzle thermal-mechanical analysis. In [11], Bartz lists a series of factors that can drive the method towards either underestimation or overestimation of the heat transfer coefficients. For example, the choice, in the model statement, of neglecting any radiative heat-transfer phenomenon, could lead to smaller predictions, at least near the throat and downstream. Carbon dioxide and water - which, among the others, result as major products of the LOX/Eth70 combustion reaction - are both known to be strong gas-radiation emitters. Thus, one way to move our model closer to reality could be somehow to include the effect of radiation heating. As for the other factors listed by Bartz, they do not apply to the case of our rocket or simply cannot be verified. In the end, net of radiation heat transfer, results obtained through the Bartz' method are acceptable. As long as turbulent boundary layer is assumed throughout the nozzle.

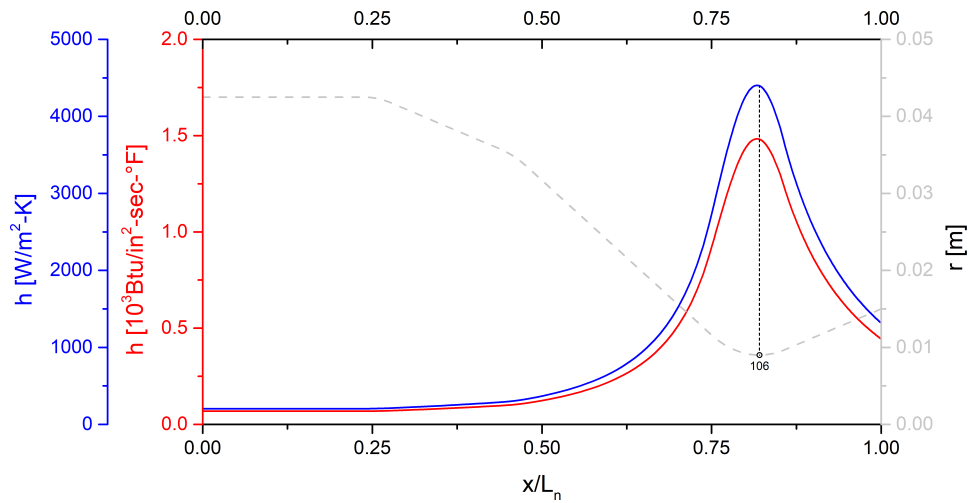


**Figure 4.8:** Heat transfer coefficient distribution (Bartz method)

	h [10 <sup>3</sup> · Btu/in <sup>2</sup> -sec-F°]		
	@chamber	@throat	@exit
Mira's nozzle	0.07	1.4	0.5
Bartz' nozzle	0.4	2.5	0.6

**Table 4.4:** A comparison in the results of the Bartz method: Mira's nozzle vs Bartz' nozzle

**The Schoenman-Block method** Schoenman and Block in [12] prove that the established turbulent boundary-layer methods for predicting throat heat fluxes are often conservative by factors of 2 or more when applied to low-thrust rocket engines. Historically, test data available to validate these methods have come from the testing of relatively large nozzles. But when dealing with small-size low-pressure nozzles, correlation was lost. The inability to achieve a good correlation with experimental heat-transfer coefficients has been overcome by the a-priori assumption of laminar boundary-layer flow for the near throat region and downstream. Figure 4.9 illustrates the boundary-layer development as it might actually occur along the contour of a low-thrust, low-pressure thrust chamber. In Schoenman and Block's words "A stagnation point is assumed to exist at the injector-chamber interface, followed by the development of a laminar boundary layer. Transition to a turbulent boundary layer occurs prior to arrival at the point in the convergent section where the pressure gradient begins to affect the heat transfer. Further downstream, the pressure gradient may be strong enough to initiate reverse transition. If this strong gradient persists over a long enough flow path, a completely laminar region will follow in the vicinity of the throat. A second forward transition to a turbulent boundary layer, may occur downstream from the throat as the pressure gradient decreases". Basically, for the purpose of

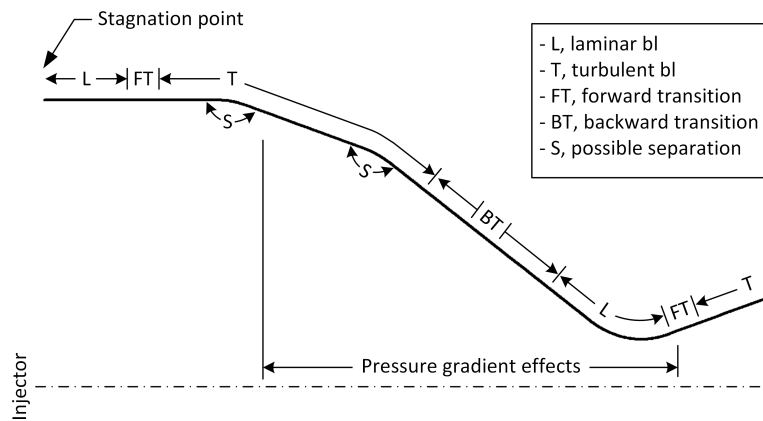


**Figure 4.9:** Boundary layer evolution along the nozzle according to the Schoenman-Block scheme

quantification and good-correlation striking with experimental data, Schoenman and Block modeled the boundary layer evolution as turbulent from the chamber starting to a conveniently-chosen reference point in the backward transition zone, and laminar downstream. The heat transfer coefficient calculation is formulated in terms of the following Stanton number correlations:

- a modified form of the Colburn equation for the prediction of heat-transfer coefficients for turbulent boundary layer in ducts and nozzles:

$$St = C_g Re_d^{-0.2} Pr^{-0.67} \quad (5.10)$$

where  $C_g$  was experimentally found to range from 0.028 at the start of convergent nozzle to 0.016 at the throat

- the uniform-temperature, flat-plate equation for laminar boundary layer:

$$St = 0.332 Re_x^{-0.5} Pr^{-0.67} \quad (5.11)$$

The plot in Fig. 4.10 shows the comparison of analytical predictions - as obtained from equation 5.10 (Turbulent Pipe Flow Eq (1) in the figure) and 5.11 (Laminar Boundary Layer, (2) in the figure) - with experimental data for the JPL-1 rocket nozzle, which actually features a geometrical layout for the throat region and downstream - namely a 30 deg convergent half-angle, a 15 deg expansion angle and a 2.68 expansion ratio - that makes it similar to our nozzle. A great correlation has been struck, transitional region aside where experimental points have been curve-fitted. As the flow accelerates, the experimental Stanton number starts to drop below the turbulent prediction calculated from equation 5.10. The start of the reverse transition is characterized by the deviation between turbulent prediction and measured data which becomes greater at each successive

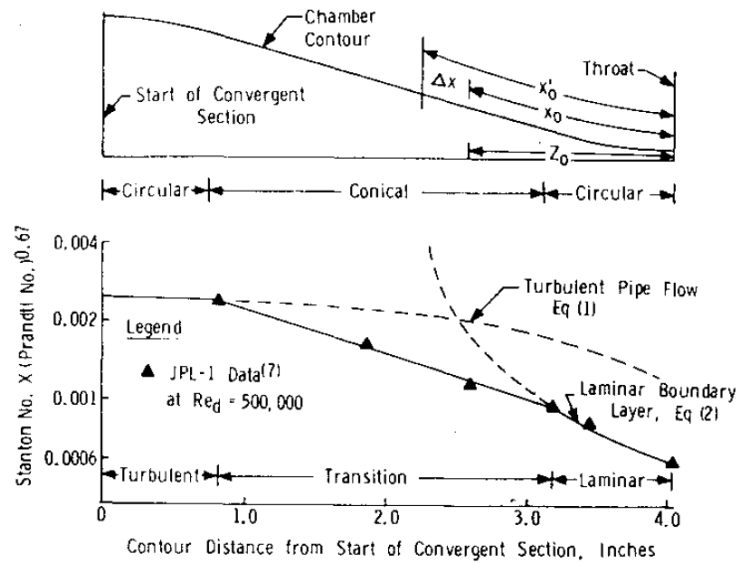


**Figure 4.10:** Heat transfer coefficients correlation for the JPL-1 rocket nozzle

station approaching the throat. Finally, after sustaining an interval of strong acceleration, the data become coincident with laminar boundary layer prediction of equation 5.11, when a particular reference position is selected. Indeed, the switch from one method to another has to occur at some station along the nozzle. Moreover, equation 5.11 - which is formulated in terms of a Reynolds number function of a coordinate  $x$  running along the flat plate surface - needs some starting point, i.e. a point at which  $x$  equals zero. Here comes the need for establishing some criteria for the determination of a reference position. The start of nozzle convergence is often suggested as a reference position for the length in boundary-layer analyses. But it is possible to link the reference position for  $x$  to the pressure gradient - which is the main driver in the laminarization process - rather than to a particular geometric feature of the nozzle. Let us consider fig. 4.11 where the ratio of local static pressure to chamber pressure ( $P_0$  in figure) is plotted versus the local coordinate  $Z$  moving upstream from the throat. Extrapolation of the maximum logarithmic pressure gradient to the point where  $P/P_0 = 1$ , provides a unique method of estimating the axial position at which the pressure gradient becomes significantly nonzero. This position, defined as  $x_0$  or  $Z_0$ , is shown in Fig. 4.10. The  $x_0$  obtained in this fashion is not far removed from the point designated as  $x'_0$ , where the laminar boundary layer equation must be effectively started so as to match the test data further downstream. The difference between  $x'_0$  and  $x_0$  is  $\Delta x$ , the initial starting length, which is determined under the assumptions of:

- boundary-layer step change from turbulent to laminar at  $x_0$
- heat-transfer coefficient continuity at  $x_0$

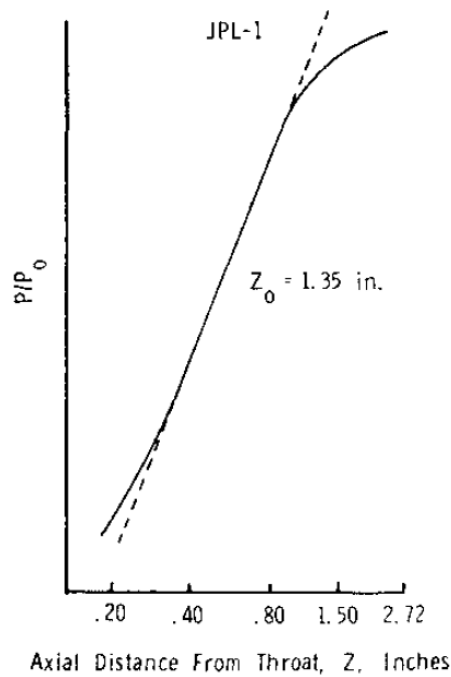


**Figure 4.11:** Logarithmic pressure distribution for the JPL-1 rocket nozzle

In this way, at the station corresponding to  $x_0$ , the turbulent Stanton number calculated from equation 5.10, equals the laminar Stanton number from equation 5.11, and an initial nonzero value for length in Eq. 5.11 can be calculated:

$$\Delta x = \left( \frac{0.332}{0.02} \right)^2 Re_{d_{x_0}}^{-0.6} D_{x_0} \quad (5.12)$$

The following step-by-step algorithm summarizes the Schoenman-Block method:

1. plot, on logarithmic scales, of the dimensionless static pressure ratio  $P/P_0$  (in the convergent section) vs axial distance as measured from the nozzle throat
2. extrapolation of the maximum logarithmic pressure gradient to the point where  $P/P_0 = 1$  in order to obtain the axial distance  $Z$ , and the corresponding contour distance  $x_0$
3. determination of  $\Delta x$  to obtain  $x'_0$
4. calculation of Stanton numbers upstream from the point  $x = x_0$  by Eq. 5.10, and by Eq. 5.11 with  $x$  measured from the point  $x = x'_0$ , to obtain Stanton numbers downstream of the point  $x = x_0$

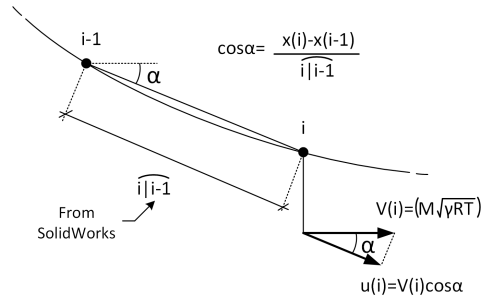
When applied to our nozzle, results in Figures 4.12, 4.13, 4.14 are produced. Fig. 4.12 shows the graphical extrapolation of the axial coordinate  $Z_0$  associated to a local pressure gradient with a significantly nonzero value. The plot in Fig. 4.13 has been created in order to monitor the  $St \cdot Pr^{2/3}$  parameter between the start of convergent station and the throat. By comparison with the same plot in Fig. 4.10, results obtained for our nozzle are confirmed: the trend is the same as well as the order of magnitude. One can notice that the turbulent and the laminar predictions, cross each other exactly at station 73 - corresponding to the point  $x_0$  - consistently with condition 5.12 of heat-transfer coefficient continuity. The red dashed line is a correction of the curve in the transition zone, so as to give a proper continuity and the typical bell-shaped profile to the heat transfer distribution in Fig. 4.14. Indeed in the transition zone, where the switch from one equation to the other occurs at point 73, there is a left peak of the curve, exactly on the switching point, that locally lends an undesired and physically-meaningless volcano-like shape to the distribution. Then - just like Schoenman and Block did in [12] (see Fig. 4.10 again), but for the purpose of experimental-data fitting in their case - a transition zone has been defined from point 61 to 78 and the  $St \cdot Pr^{2/3}$  group has been locally corrected thus remodeling the peak the way it appears in Fig. 4.14. The curve portions corresponding to nozzle-contour slope-changing points - where equation 5.10 exhibited a certain dependance upon the local nozzle evolution in shape - underwent a slight correction as well. Table 4.5 summarizes some results from the method as applied to our nozzle.

Here follow some implementation details of the code written to perform the calculations required by the method:

- the nozzle discretization of Fig. 4.7, already employed in the nozzle flow study, represented again the starting point for the nozzle heat-transfer coefficients evaluation
- at each single station of the above mentioned discretization, the following magnitudes are known:
  - local axial coordinate  $x$  and section radius  $r$
  - local Mach number  $M$ , static temperature  $T$ , pressure  $p$  and density  $\rho$  of the fluid as given back by the nozzle flow study
  - specific heat ratio  $\gamma$ , specific gas constant  $R$ , constant-pressure specific heat  $C_p$ , local dynamic viscosity  $\mu$ , local thermal conductivity  $\kappa$  of the gas mixture are known from the CEA tool at station 1, 106 and 178. A linear variation for the points in between has been imposed
- given the above mentioned properties data, if  $i$  is the  $i$ -th station in the transonic and supersonic region, the following calculations are performed by the code:

$$\left\{ \begin{array}{l} x_{\text{plate}}(i) = \Delta x + \frac{x_{x_0} - x_{74}}{\cos \alpha} + \frac{x_{74} - x_{74}}{\cos \alpha} + \dots + \frac{x_{i-1} - x_i}{\cos \alpha} \\ u(i) = M(i) \cos \alpha \sqrt{\gamma(i) R(i) T(i)} \\ Re_x(i) = \frac{\rho(i) u(i) x(i)}{\mu(i)} \\ Pr(i) = \frac{\mu(i) c_p(i)}{\kappa(i)} \\ St(i) = 0.332 Re_x(i)^{-0.5} Pr(i)^{-0.67} \\ h(i) = St(i) \rho(i) u(i) c_p(i) \end{array} \right.$$

where the direction cosine  $\cos \alpha$  of the local velocity vector equals 1 on the horizontal portion of the nozzle contour and at the throat station where the flow is locally horizontal (points 1 to 23 and 106 respectively),  $\cos(\pi/12)$  on the first convergent tract (points 24 to 44),  $\cos(\pi/6)$  on the second convergent tract (points 45 to 77) and on the divergent tract (points 120 to 178). As for the curve tract which characterizes the throat region, the following approximation for the local velocity at each station has been adopted:



i.e. the local velocity is approximated by that vector having a direction coincident with the line tangent to the nozzle-arc between the current node  $i$  and the previous node  $(i - 1)$

- the same calculations are performed in the subsonic region, the only difference lying in the Reynolds and Stanton formulas:

$$\left\{ \begin{array}{l} Re_d(i) = \frac{\rho(i) u(i) 2r(i)}{\mu(i)} \\ St(i) = C_g Re_d(i)^{-0.2} Pr(i)^{-0.67} \end{array} \right.$$

for the  $C_g$  factor experimental values are suggested by Schoenman and Block from 0.026 at chamber to 0.016 at throat. Again, a linear variation has been imposed for the points in between

The previous code-implementation details close the discussion of the Schoenman-Block method. As a last step, a results comparison with the Bartz method is mandatory in order to make a choice.

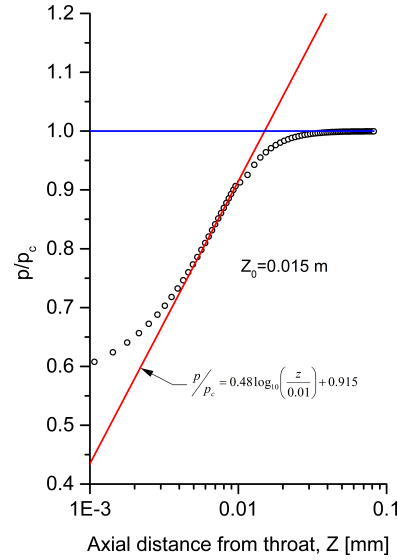


Figure 4.12: Logarithmic pressure-gradient extrapolation

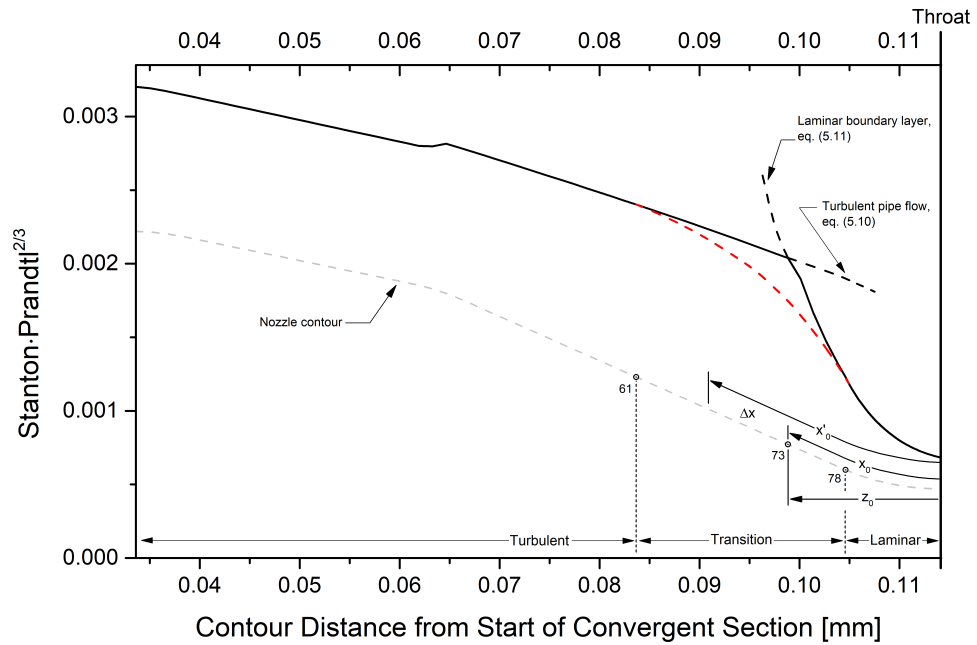
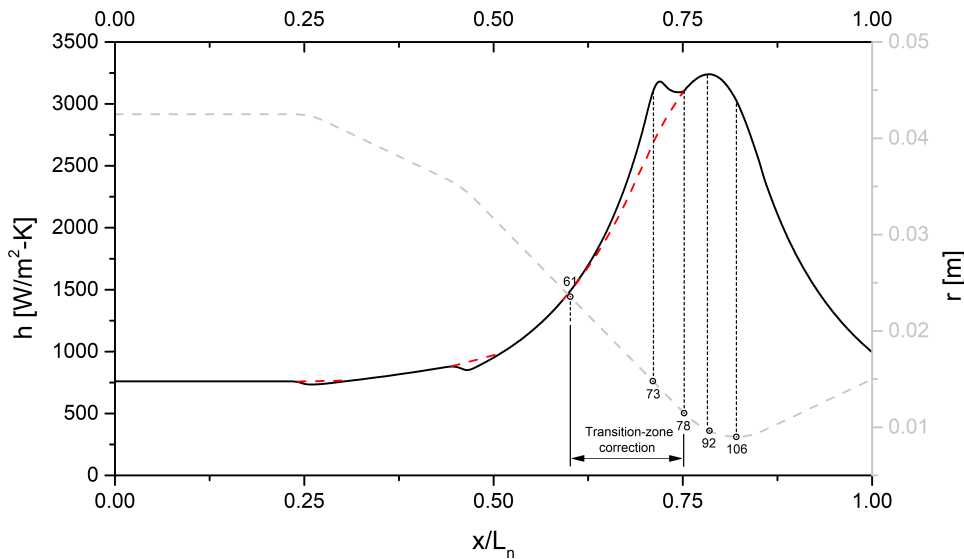


Figure 4.13: Laminarization of the boundary layer



**Figure 4.14:** Heat transfer coefficient distribution (Schoenman-Block)

$x_0$ [mm]	$x'_0$ [mm]	$\Delta x$ [mm]	$h$ @ throat [W/m <sup>2</sup> -K]
0.0162	0.0220	0.0058	3028

**Table 4.5:** Results from the Schoenman-Block method

**Bartz VS Schoenman-Block** In Fig. 4.15 the obtained heat-transfer coefficient distributions are plotted. The trend is similar, with the bell-like typical profile, but still different. The first difference one can spot by inspection, lies in the heat-transfer coefficient gap at each station. Before point 71, where the curves intersect, it amounts to 300 W/m<sup>2</sup>-K at chamber - where the Bartz estimation is more than doubled by S-B method's predictions - and slightly decreases to zero when the curves approach each other, station by station, until point 71. Afterwards the Bartz distribution goes up to a peak of 4397 at throat section, whereas the Schoenman-Block curve presents a local value of 3028 and the distance between the curves reaches its maximum. It is plain that the laminar boundary-layer assumption implicates a substantial reduction in the heat-transfer coefficient values. But after all such a consequence is coherent with the physics underlying the boundary layer heat transfer. Indeed, in turbulent flows, an additional mechanism of heat-transfer - namely the eddy transport - is active in the radial and azimuthal directions, thus providing a much better transfer of energy across the flow at a given axial station, than in laminar flow. Therefore turbulent correlations for the heat transfer coefficient are calibrated on experimental data so as to give back larger values. Another difference one can notice, is the maximum of the Schoenman-Block distribution not occurring at throat (precisely at

station 92 as indicated in Fig. 4.14). This is not surprising and actually is more consistent with real nozzles behaviour. Back et al. in [14], relate the maximum in heat transfer coefficient to the mass flow rate per unit area, which experiments prove to be largest just upstream of the throat.

In the end, experimental data from literature lead to conclude that the Bartz method is good for rapid calculations and for order-of-magnitude estimations of the convective heat-transfer coefficient for large nozzles, but when applied to small rockets, it overestimates heat transfer coefficients by a factor of 2 or more (1.5 for the case of our rocket, but it is pointed out that in our calculation of the coefficients through the Bartz method, the temperature ratio  $T_w/T_c$  has been set to one, its maximum, thus giving back the lowest distribution possible; more realistic less-than-unity values of the ratio would produce larger heat transfer coefficients, thus increasing the gap between the two methods). Adopting a 1.5 factor (at least) would mean a conservative choice with overestimated heat flux and, potentially, temperatures beyond the materials limits. It could lead to misleading results and to a redesign of the nozzle, disadvantageous in terms of costs and weight of the system as well as pointless, since the result of an overestimation.

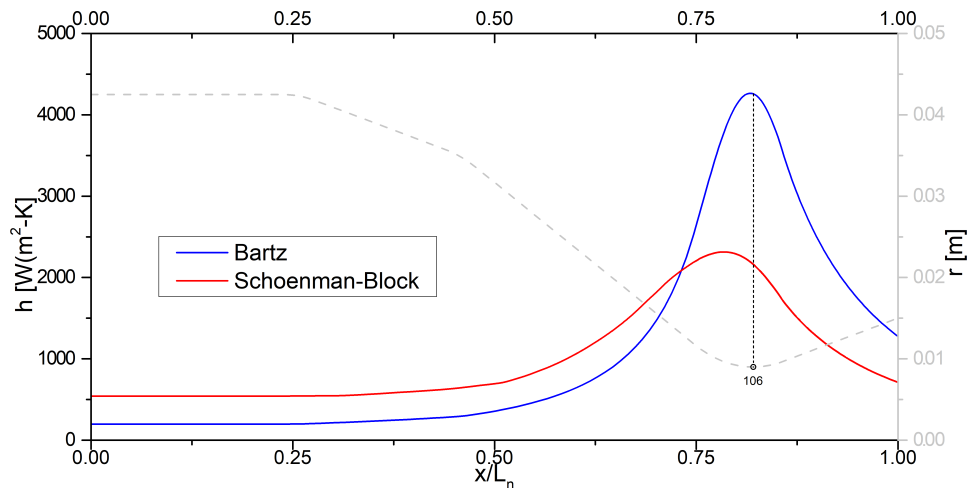


**Figure 4.15:** Comparison between heat transfer coefficient distributions

### Convection on the faceplate modeling

Fig. 4.16 depicts a plausible scenario for the injector-plate heat-transfer modeling. Exactly in the middle of the faceplate, takes place the exhaust of the swirl injector assembly, consisting in a thin conical sheet of propellants mixture undergoing combustion, which is supposed to be restricted to an area as close as possible to the injector head (stoichiometric combustion core in the figure). In this way, it is implicitly assumed that the processes of vaporization, mixing, atomization and reaction of the propellant occur in a very fast way, i.e. the con-

ical jet starts burning close to the injector head. As previously mentioned, a passive cooling strategy has been adopted for the combustion chamber wall: the ethanol injection follows a conical path with a spray angle wider than the oxygen's, thereby easing the thermal loading acting upon the chamber. Given the  $48^\circ$  spray angle and the 42.5 mm chamber radius, the length  $x_l$  of chamber shielded by the ethanol cone, is readily estimated as follows:

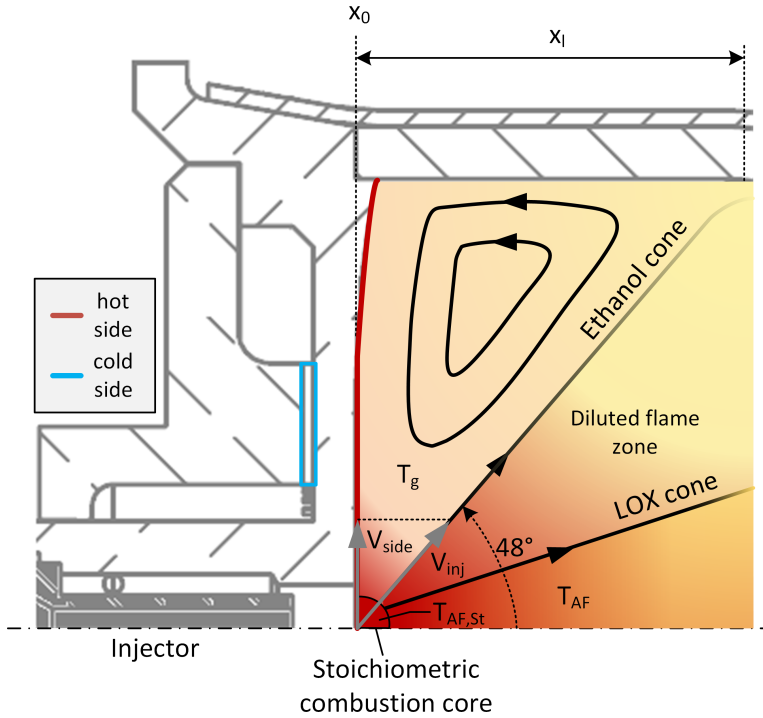


**Figure 4.16:** Heat-transfer modeling on the faceplate

$$\frac{42.5}{x_l} = \tan 48^\circ \Rightarrow x_l = 38.3 \text{ mm}$$

a number corresponding to station 25 of the nozzle discretization so far adopted. The gas-side temperature, for the wall points laying within the chamber length extending from  $x_0$  - chamber starting, i.e. faceplate - to  $x_l$ , is expected to be lower than the theoretical adiabatic-flame chamber temperature  $T_c = T_{AF} = 2913 \text{ K}$  predicted by the non-stoichiometric model implemented in the CEA tool. Now, the question is: how much lower? The gas temperature, in the chamber portion spanning from  $x_0$  to  $x_l$ , rises from  $T_g$  - that is, the bulk temperature characterizing the combustion gas before forced convection occurs on the faceplate - up to  $T_c = T_{AF}$ . So first of all we are interested in obtaining a reasonable estimation for  $T_g$  on the hot side. In doing so, let us map the different combustion zones in the chamber. The injection of the propellants with different spray angles, creates a combustion core in front of the injector, where combustion is locally realized

at stoichiometric condition - with a temperature being  $T_{AF,st} = 3260$  K pertaining to the LOX/Eth70 combustion at  $O/F_{st} = 1.5$  - while the excess of ethanol surrounds the inner cone. The droplets then continue their journey through the chamber while mixing until the non-stoichiometric nominal ratio is reached and the flame temperature drops to the adiabatic-flame chamber temperature  $T_c = T_{AF} = 2913$  estimated in subsection 5.3.3. This axial combustion zone is enclosed with a diluted flame area bounded by the ethanol cone. Finally, outside the ethanol cone the combustion flow forms a large corner recirculation zone. Here the temperature is not axially uniform. On the faceplate the bulk temperature of the combustion gases drops to  $T_g$ , while gradually increasing in the axial direction until a uniform profile at  $T_c = T_{AF}$  is achieved around station 25, where the ethanol shielding effect is over. Now, a reasonable estimation of  $T_g$  would be that temperature that, averaged with the stoichiometric reaction temperature  $T_{AF,st}$  - that is, the temperature reached in the inner cone beside the injector head - gives back the adiabatic-flame combustion temperature  $T_c = T_{AF}$ :

$$T_c = T_{AF} = \frac{T_g + T_{AF,st}}{2} \Rightarrow T_g = 2566 \text{ K}$$

It is now possible to estimate the hot-side convective heat-transfer coefficient for the faceplate through the following Stanton-number correlation for the turbulent incompressible flow over a flat-plate:

$$St_{HS} = 0.185 (\log_{10}(Re_x))^{-2.584}$$

Convective heat transfer is indeed realized by the fluid moving along the faceplate with velocity  $v_{side}$ . The Reynolds number is estimated as follows:

$$\left\{ \begin{array}{l} \mathcal{M} = 21.495 \text{ mol} \\ R_{GAS} = \frac{R}{\mathcal{M}} = 386.8 \text{ J/kg-K} \\ \rho = \frac{p_c}{R_g T_g} = 1.5113 \text{ Kg/m}^3 \\ v_{side} = 29 \text{ m/s} \\ \mu_g = 2.3753 \cdot 10^{-5} \text{ Pa} \cdot \text{s} \\ Re_x = \frac{\rho v_{side} r_c}{\mu_g} = 78419 \end{array} \right.$$

where the average molecular mass  $\mathcal{M}$  is obtained from the chemical analysis of the LOX/Eth70 combustion; the viscosity of the gas mixture  $\mu_g$  has been calculated with a Nasa method for the viscosity of gas mixtures [13], given the molecular mass of major species, namely carbon dioxide, water, carbon monoxide, hydrogen, obtained through the CEA program, and the dynamic viscosity of each component at  $T_g$ ; the local velocity of the fluid flowing parallel to the faceplate has been estimated by Fiore in his thesis work [25], concerning the swirl injector

device dimensioning and optimization. Finally, the following coefficient characterize the hot-side heat transfer on the faceplate:

$$h_{HS} = St_{HS} \rho v_{\text{side}} C_p = 507 \text{ W/m}^2\text{-K}$$

with the constant pressure specific heat  $C_p$  obtained as the summation of the  $C_{p_i}$  of the single component (at  $T_{AF}$ ) times its molar fraction  $x_i$ , as taken from the propellant combustion reaction in subsection 5.3.3.

Now let us consider the faceplate-backplate interface. Here a system of 40 tiny channels cools down the injector plate by forced convection of the ethanol flowing at high pressure through them. In order to get an estimation of the corresponding convective heat-transfer coefficient, the Reynolds number must be calculated, so as to understand the boundary layer nature - laminar or turbulent - and pick up an adequate formula. The single channel is square sectioned -  $A_c = 1 \text{ mm}^2$  - thus an equivalent hydraulic diameter is calculated as follows:

$$D_H = \frac{4A_c}{P_w} = 10^{-3} \text{ m}$$

$P_w$  being the wetted perimeter. Then, given for the ethanol the following properties, evaluated at  $0^\circ\text{C}$  in [15]:

$$\begin{cases} \mu_c = 1.792 \cdot 10^{-3} \text{ Ns/m}^2 \\ c_p = 2250.57 \text{ J/Kg-K} \\ \kappa_c = 0.17435 \text{ W/m-K} \end{cases}$$

and the  $\dot{m}_F = 0.1136 \text{ Kg/s}$  propellant mass flow rate, as redefined in subsection 5.3.3 for the 1.2 mixture ratio prescribed for the flight model, the following Reynolds and Prandtl numbers follow:

$$\begin{cases} Re_c = \frac{\rho_c V_c D_h}{40 \mu_c} = \frac{\dot{m} D_h}{40 A_c \mu_c} = 1585 \Rightarrow \text{laminar flow} \\ Pr_c = \frac{\mu_c c_p}{\kappa_c} = 23 \end{cases}$$

Under the assumption of fully developed laminar flow, the following Nusselt correlation - provided by Mills in [16] - allows the heat-transfer coefficient determination:

$$Nu = 3.66 + \frac{0.065 Re_c Pr_c D_h/L}{1 + 0.04 (Re_c Pr_c D_h/L)^{2/3}} = 25 \Rightarrow h_c = \frac{Nu \kappa_c}{D_H} = 4359 \text{ W/m}^2\text{K}$$

The obtained value differs by an order of magnitude from the hot-side coefficient, reflecting the higher effectiveness of a liquid phase over a gas when it comes to convective heat transfer.

Now the last step in collecting all the necessary input data for the thermal stress analysis, is represented by the choice of proper materials' properties values, subject of the following subsection.

### 4.3.6 Materials' properties

In the model statement the assumption of temperature nonlinearities negligibility has been adopted, that is materials' properties do not depend upon temperature. Such an assumption would make perfect sense if a thermal equilibrium condition was reached by the system. But this is not the case of our rocket engine by far, since the very short firing-time span does not allow the temperature of any material to set on steady values. On the bright side, the shorter the firing time, the lower the maximum temperature reached, the shorter the materials exposure to increasing temperature. At any rate, as a common practice in engineering, we choose to pursue simplification by adopting worst-case values for the properties involved in the analysis.

Now, in a rocket engine, temperature varies over the burning time as well as in space due to the hot gas flow expansion occurring through the nozzle. And so do material properties along with it. In table 4.2 for each of the thermal properties - namely thermal conductivity, specific heat and thermal expansion coefficient - a couple of values are indicated, at room condition and around the maximum service temperature, followed by the percent variation in between. 304 Series Stainless Steel's properties all exhibit increasing values: conduction heat fluxes become greater thus assisting heat removal from the chamber; at the same time the temperature increase is slowed down and deformations become more significant. Behaviour would be the same for the two materials which the nozzle is made up of, if the thermal conductivity did not decrease: indeed both Iso-statically Pressed graphite and OCMC exhibit a more insulating behaviour when temperature goes up. One can also spot a good thermal expansivity matching between the nozzle materials. As for the other mechanical properties requested as input, it is sufficient to say that they basically drop with temperature. Materials indeed generally deliver poorer mechanical performance at high temperatures. Graphite is an exception since its Young's modulus can increase up to 25% starting from the room temperature value. Further details about high temperature characteristics of stainless steel, graphite, OCMC in Ref. [17], [18], [19], [20], [22], [23], [24].

Again, since the analysis will be linear, it is required to pick a single value for each property:

- the graphite liner is directly exposed to the hot gas flow with a maximum bulk temperature of  $(T_\infty)_{\max} = 2913 \text{ K}$ , a value which is close to the material's maximum service temperature. Forced convection - the main driver in the heat removal process in the thrust chamber - will cause a temperature fall down to a value  $T_w$  at wall, well below  $(T_\infty)_{\max}$ . Worst-case scenario would be  $T_w \approx (T_\infty)_{\max} \approx T_{\max}$  with properties' values to be picked near the maximum service temperature
- the OCMC shell is in direct contact with the liner. Forced convection at wall first and conduction through the graphite then, will further lower

the temperature. In [8], it is reported an observed temperature of about 1300°C on the ceramic during a test. It is then correct to assume a maximum service temperature of around 1600K. Let us suppose an average temperature of  $T_i = 0.7(T_\infty)_{max} = 1100K$  at the OCMC-graphite interface. This time average values of the properties seem a good compromise

- the stainless steel faceplate experiences direct contact with the hot combustion gases on its hot side where forced convection takes place, followed by conduction through steel and then again forced convection on the cold side by means of ethanol as a coolant which relieves local thermal loading. Surface temperature on the hot side has been estimated by Fiore[25] to be around  $T_{w,hs} = 485 K$ . It has to be pointed out that such a value results from a propellant mixture ratio of  $O/R = 1.1$ . The engine in its flight version features a  $O/R = 1.2$  mixture ratio, consequently a higher adiabatic flame temperature and eventually a higher wall temperature in the chamber. Again, average values for the stainless steel's properties seem a reasonable compromise

The radar plot in Fig. 4.17 summarizes the properties for each material along with the selected values (units are consistent with Table 4.2). Graphite has the highest thermal properties of the trio. The large thermal conductivity will minimize temperature gradients and produce high heat transfer rates through the wall, thus reducing thermal stresses within it, while the good specific heat will ensure valuable heat-absorption capacity. As for the thermal expansion coefficient, it is enough to highlight, one more time, the good matching of graphite's with OCMC's. Since graphite does not play the role of insulator, the OCMC material provides the thrust chamber with such a capability. It features indeed the lowest thermal conductivity while fulfilling the structural shell function as well, thus covering for the quite low mechanical properties of the graphite. A moderate thermal conductivity and the lowest heat capacity characterize the stainless steel. The amount of heat absorbed by the faceplate over the burning time - and afterwards when the graphite is heated through and still heating - should be limited, thus avoiding excessive thermal loading. In conclusion, such an overall configuration perfectly portrays the identikit of a *heat-sink* chamber, which utilizes the transient-energy-storage capability of the wall in order to limit surface temperatures.

### Erosion

Experience gained with nozzles made up of carbon materials, such as graphite, suggests that, when exposed to a high-temperature, high velocity gas flow during burning, it is likely for the nozzle to undergo erosion, which can represent a major issue if not controlled with consequences on both the thermal response and the overall performance of the rocket itself. Of particular concern is the throat region where an enlargement in the section area could lower the chamber

**Table 4.6:** Temperature effect on thermal properties of the materials

Property	@ $T_{room}$	@ $\sim T_{max} \simeq 1100K$	% $\Delta$
$\kappa$ [W/m <sup>2</sup> -K]	12	26	+54%
$c$ [J/Kg-K]	450	600	+27%
$\alpha$ [10 <sup>-6</sup> K]	15	20	+25%
$E$ [GPa]	200	124	-38%
$\nu$ [-]	0.28	0.25	-10%

**(a)** Austenitic Stainless Steel 304

Property	@ $T_{room}$	@ $\sim T_{max} \simeq 3100K$	% $\Delta$
$\kappa$ [W/m <sup>2</sup> -K]	130	40	-70%
$c$ [J/Kg-K]	600	2200	+73%
$\alpha$ [10 <sup>-6</sup> K]	7	9.5	+26%
$E$ [GPa]	4.8	6	+25%
$\nu$ [-]	0.28	n/a	-

**(a)** Isostatic Graphite

Property	@ $T_{room}$	@ $\sim T_{max} \simeq 1600K$	% $\Delta$
$\kappa$ [W/m <sup>2</sup> -K]*	4.5	2.5	-45%
$c$ [J/Kg-K]	750	1300	+42%
$\alpha$ [10 <sup>-6</sup> K]*	7	8.5	+17%
$E$ [GPa]	92	65	-70%
$\nu$ [-]	0.21	n/a	-

\* Principle fiber direction

**(a)** OCMC

pressure as well as the specific impulse. Erosion modeling and prediction is not a simple task, since the phenomenon is not thoroughly understood. Literature ([1], [3], [21]) separates mechanical erosion from chemical erosion. They both cause throat enlargement and performance losses. The former is mostly due to the high prevailing shear-stress, occurring nearby the throat and promoting mechanical action by particles, while the latter is caused by chemical interaction of aggressive oxidizing species, such as  $H_2O$ ,  $OH$  and  $CO_2$  in the boundary layer, with the wall material. Chemical erosion affects thermal loading of the nozzle as well: if local reactions are exothermal, an increase in heat transfer rates has to be accounted for. Table 4.10 shows to what extent typical erosion rates for graphite - as taken from [1] - can affect the performance of our rocket for the prescribed burning time of 20 s. Values in table 4.10 are nothing but numbers to get an idea about the potential consequences of the phenomenon and it is important to stress the inability to obtain sufficiently reliable data to quantify

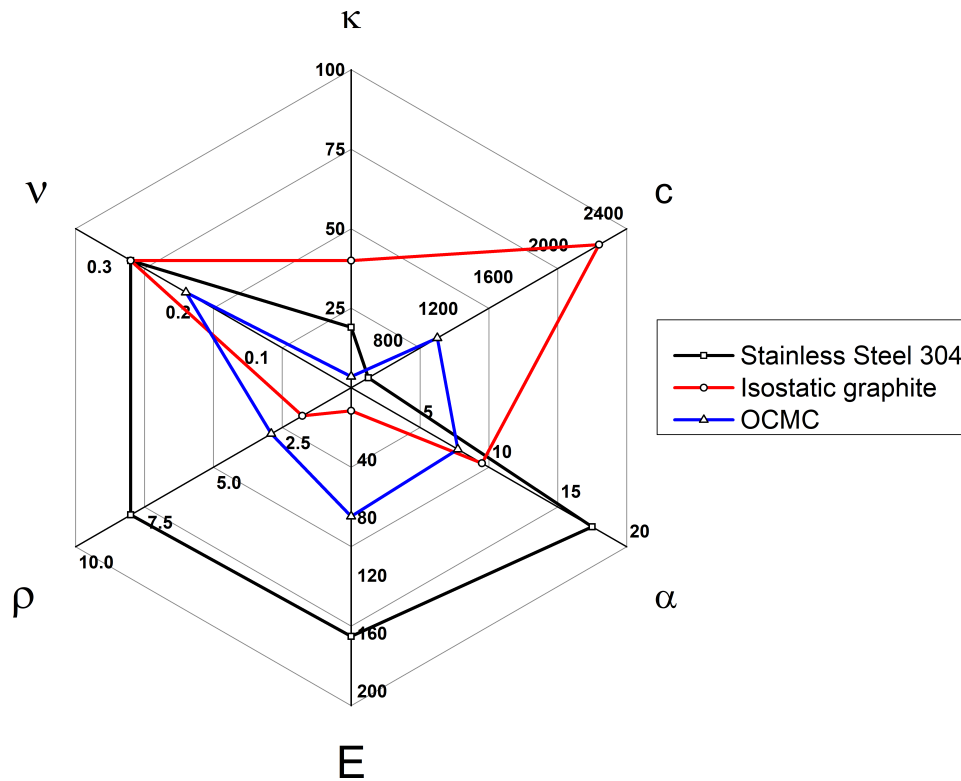


Figure 4.17: Materials' properties radar distribution

erosion by means of preliminary calculations only. We leave to the envisaged fire-test campaign the task to confirm or deny the above mentioned numbers.

$ER$ [mm/s]	$\Delta r_t$ [mm]	$\epsilon$ [-]	$I_{sp}$ [s]	$\Delta I_{sp}\%$
0	-	2.78	226.3	-
0.0254	0.5	2.49	225.4	-0.4
0.1524	3	1.56	215.3	-4.9

Table 4.10: Graphite erosion rates and effects on rocket's performance

#### 4.3.7 An analytical estimation of the temperature through the wall

Everything is set in order to feed the Ansys program with the required input data and get back the results of the thermal-mechanical analysis of the thrust chamber. But before proceeding, it is worth a try to estimate, via analytical formulation, the temperature profile through the wall at different stations, so as to get an idea of what we should expect from the ansys, for the input parameters so far determined and selected.

Let us start by the chamber faceplate. The local temperature profile is sketched

in Fig. 4.18. Temperature drops from  $T_{\text{gas}}$  associated to the hot gas flow in the chamber, down to  $T_{\text{coolant}}$ , as a result of a forced convection upon the hot side, conduction through the steel thickness  $L_{\text{steel}}$ , and again forced convection of the coolant flow on the cold side. We want to estimate the hot-side wall temperature  $T_{\text{HS}}$  as well as the cold-side temperature  $T_{\text{CS}}$  at the faceplate-coolant interface. Under the assumptions of steady-state, one-dimensional problem, homogeneous material (i.e. isotropic thermal conductivity), no mass transport and no internal heat source either, the general conduction energy equation introduced in Chapter 2 is simplified as follows:

$$k\nabla T = 0 \Rightarrow \frac{d^2 T}{dx^2} = 0$$

By approximation of the faceplate to a wall of thickness  $L_{\text{steel}}$ , the steel layer must satisfy the above written equation, whose solution is a linear function in  $x$ :

$$T(x) = a + bx$$

that is, the temperature profile across the steel layer. Now, in order to determine the constant  $a$  and  $b$ , the following boundary conditions on the hot-side wall and the cold-side wall are applied:

- convective boundary condition at  $x = 0$  (notice the direction of the normal versor  $\bar{n}$ ,  $\bar{n} = -\bar{i}$ ):

$$\begin{aligned} \bar{q} \cdot \bar{n} \Big|_{x=0} &= h(T - T_{\text{gas}}) \Big|_{x=0} \\ \Rightarrow \left( -\kappa \frac{dT}{dx} \bar{i} \right) \cdot (-\bar{i}) &= \kappa_{\text{steel}} \frac{dT}{dx} \Big|_{x=0} = \kappa_{\text{steel}} b = h_{\text{HS}} (T - T_G) \Big|_{x=0} \\ \Rightarrow \kappa_{\text{steel}} b &= h_{\text{HS}} (a - T_{\text{gas}}) \end{aligned}$$

- convective boundary condition at  $x = x_{\text{CS}}$  (notice the change in  $\bar{n}$  direction,  $\bar{n} = \bar{i}$ ):

$$\begin{aligned} \bar{q} \cdot \bar{n} \Big|_{x=x_{\text{CS}}} &= h(T - T_{\text{cool}}) \Big|_{x=x_{\text{CS}}} \\ \Rightarrow \left( -\kappa \frac{dT}{dx} \bar{i} \right) \cdot (\bar{i}) &= -\kappa_{\text{steel}} \frac{dT}{dx} \Big|_{x=x_{\text{CS}}} = -\kappa_{\text{steel}} b = h_{\text{CS}} (T - T_{\text{cool}}) \Big|_{x=x_{\text{CS}}} \\ \Rightarrow -\kappa_{\text{steel}} b &= h_{\text{CS}} (a + bx_{\text{CS}} - T_{\text{cool}}) \end{aligned}$$

Consequently we have two equations and two unknowns ( $a$  and  $b$ ) as follows:

$$\begin{cases} \kappa_{\text{steel}} b = h_{\text{HS}} (a - T_{\text{gas}}) \\ -\kappa_{\text{steel}} b = h_{\text{C}} (a + bx_i - T_{\text{cool}}) \end{cases}$$

Now, given:

$$\begin{cases} T_{\text{gas}} = T_g = 2566 \text{ K} \\ T_{\text{cool}} = 273.15 \text{ K} \\ h_{\text{HS}} = 507 \text{ W/m}^2\text{-K} \\ h_{\text{CS}} = h_c = 4359 \text{ W/m}^2\text{-K} \\ \kappa_{\text{steel}} = 19 \text{ W/m-K} \\ x_{\text{CS}} = L_{\text{steel}} = 0.004 \text{ m} \end{cases}$$

the system is readily solved for  $a$  and  $b$ . One can notice that the intercept  $a$  corresponds exactly to the wall temperature  $T_{\text{HS}}$ , being the y-axis coincident with the hot-side wall:

$$\begin{cases} a = \frac{T_{\text{gas}} \left( h_{\text{HS}} + \frac{h_{\text{CS}} h_{\text{HS}}}{\kappa_{\text{steel}}} x_{\text{CS}} + h_{\text{CS}} T_{\text{cool}} \right)}{h_{\text{HS}} + h_{\text{CS}} + \frac{h_{\text{CS}} h_{\text{HS}}}{\kappa_{\text{steel}}} x_{\text{CS}}} = T_{\text{HS}} = 691 \text{ K} \\ b = -50033 \text{ K/m} \end{cases}$$

Finally the temperature  $T_{\text{CS}}$  at the faceplate-coolant interface is known by evaluating the temperature equation at  $x = x_{\text{CS}}$ :

$$T_{\text{CS}} = T(x = x_{\text{CS}}) = T_{\text{HS}} - 51354 x_{\text{CS}} = 491 \text{ K}$$

The solution can be extremely simplified, by pointing out that, for one-dimensional, steady-state, no heat-sinks/sources heat flow, the heat flux must be a constant as it passes through the convective hot-gas layer on the left, through the stainless steel layer and finally through the convective coolant layer on the right. The heat-flux formula is thus expressed in the following simplified fashion:

$$q_x = -\frac{1}{R} \Delta T$$

where  $\Delta T = T_{\text{cool}} - T_{\text{gas}}$  is the overall temperature difference from one side to the other, and  $R$  is the summation of thermal resistances:

$$R = \frac{1}{h_{\text{HS}}} + \frac{L_{\text{steel}}}{\kappa_{\text{steel}}} + \frac{1}{h_{\text{CS}}}$$

Such a formula for the heat-flux calculation, originates from the the analogy between conductive heat transfer and electrical current flow, an analogy that is rooted in the similarity between Fourier's and Ohm's laws.

Let us now focus on the nozzle. This is an axysymmetric assembly, therefore the cylindrical-wall approximation better suits to it (see Fig. 4.18 for a qualitative sketch of the local temperature profile). Neglecting the convective air layer surrounding the nozzle, the local boundary condition consists in a constant temperature distribution equal to  $T_{\text{air}} = 273.15 \text{ K}$  on the external contour. Thus the overall temperature difference is:

$$\Delta T = T_{\text{air}} - T_{\text{gas}}$$

and the overall thermal resistance is given by the summation of the convective hot-gas resistance, the conductive graphite resistance and the conductive OCMC resistance:

$$R = R_{\text{wall}} + R_{\text{graph}} + R_{\text{OCMC}}$$

in particular the following expressions apply to the case of a cylindrical wall:

$$\left\{ \begin{array}{l} R_{\text{wall}} = \frac{1}{h_{\text{wall}} 2\pi r_w L} \\ R_{\text{graph}} = \frac{\ln(r_i/r_w)}{\kappa_{\text{graph}} 2\pi L} \\ R_{\text{OCMC}} = \frac{\ln(r_w/r_e)}{\kappa_{\text{OCMC}} 2\pi L} \end{array} \right.$$

$L$  being the nozzle length. Once the heat flux is calculated, temperatures at the prescribed points across the wall follow as:

$$\left\{ \begin{array}{l} T_{\text{wall}} = T_{\text{gas}} - qR_{\text{wall}} \\ T_{\text{int}} = T_{\text{gas}} - q(R_{\text{wall}} + R_{\text{graph}}) \end{array} \right.$$

The following data characterize any station situated along the chamber length:

$$\left\{ \begin{array}{l} T_{\text{gas}} = T_c = T_{\text{[AF]}} = 2913 \text{ K} \\ T_{\text{air}} = 273.15 \text{ K} \\ h_{\text{wall}} = 759 \text{ W/m}^2\text{-K} \\ \kappa_{\text{graph}} = 40 \text{ W/m-K} \\ \kappa_{\text{OCMC}} = 2.5 \text{ W/m-K} \\ r_w = 0.0425 \text{ m} \\ r_i = 0.0475 \text{ m} \\ r_e = 0.049 \text{ m} \\ L = 0.14113 \text{ m} \end{array} \right.$$

and lead to the estimation of the temperatures across the chamber wall:

$$\left\{ \begin{array}{l} T_{\text{wall}} = 1210 \text{ K} \\ T_{\text{int}} = 1048 \text{ K} \end{array} \right.$$

An attempt can be done to get similar predictions at the throat station, although the approximation of the local wall geometry with a cylindrical plane wall seems unsuitable for such a radius-varying, minimum-curvature region. Here follow the results for the throat station:

$$\begin{cases} T_{\text{wall}} = 1585 \text{ K} \\ T_{\text{int}} = 755 \text{ K} \end{cases}$$

As for the estimations obtained, it suffices to say that they include temperature values below the operational limits of the materials employed. Of course it does not mean the thrust chamber will survive the 20 s burning time (without mentioning the possible over-the-limit structural stress arising). Although quite realistic and comforting, the above predictions still originate from the steady-state heat-transfer assumption. It is reasonable and prudent to expect higher values of temperature, particularly at the chamber spot where no cooling strategy is adopted and for the intrinsic thermal characteristics of the wall materials (i.e. an insulating composite like the OCMC, housing a high heat-absorption material such as the graphite which the nozzle is made up of). Whether or not the temperature increase over the burning time will overcome the materials' limit is a question that only a computational transient analysis can answer to. Let us finally address the question with the Ansys software.

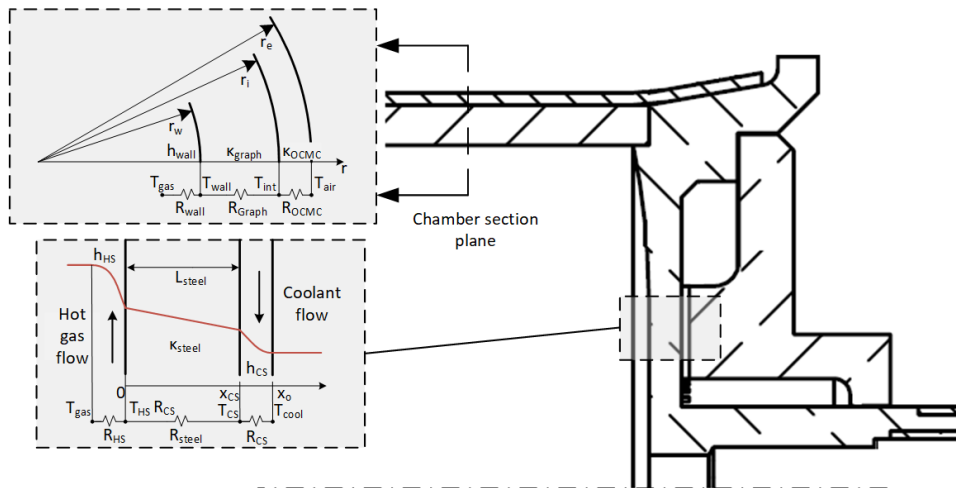


Figure 4.18: Temperature profiles estimation

### 4.4 Thermal-Structural Analysis

It is convenient to recap the problem we are dealing with, as well as the modeling scheme so far adopted. Basically a rocket thrust chamber has to be fired for 20 seconds. Before conducting actual testing on the engine, we are interested in predicting his thermal and structural behaviour for a given geometry and selected materials. The modeling of such a system reduces the problem to the thrust chamber being heated over the firing time by the hot gas flow resulting from the combustion. Forced convection has been identified as the driver

and predominant phenomenon in this heating process, thus no other loads but the convective heat fluxes at wall are taken into account. At the burnout instant, thermal and mechanical stress distributions are produced, the mapping of which by means of a FEM-based numerical analysis is what we ultimately aim for. In section 5.3 a series of preliminary calculations have laid the groundwork for the thermal-structural numerical analysis, providing us with the input data requested by the FEA program ANSYS, that is, the CAE tool employed in fulfilling the task. The model statement of Sec. 5.2.4 well sums up the choices so far made in modeling the problem.

#### 4.4.1 Boundary conditions and meshing process

In Fig. 4.19 the adopted geometry is represented together with the imposed boundary conditions. The geometry, acquired from the CAD model, consists of a plane section of the thrust chamber containing the axis of the engine, thus taking advantage of its axisymmetric layout. As for the boundary conditions, they comprise the following thermal BCs:

- convective BC1 along the inner wall of the nozzle. In Sec. 5.3.5 the convective heat transfer coefficients distribution has been determined - exploiting a method suggested by Schoenman and Block in [12] - for each of the 178 stations in which the nozzle inner contour has been discretized. Now, since in the ANSYS software the convective BCs must be specified on a *surface*, the previous stations discretization has been replaced with a surfaces discretization: by switching to 179 points indeed, the inner contour is split in 178 tiny faces, each one with its own heat transfer coefficient. For the sake of precision, it is pointed out that one value out of 178 in the heat transfer coefficient distribution is cut out: the first of the discretization surfaces is not exposed to the hot gas flow since it represents the horizontal contact surface of the nozzle and the faceplate (see detailed sketch in the figure, where the small surface is highlighted in red). Furthermore on the single surface, along with the convective coefficient, is required a reasonable value of the bulk temperature of the gas flow. The required temperature distribution is the one obtained in the convergent-divergent nozzle flow study of Sec. 5.3.4, with a slight, yet reasonable modification as one can spot in the temperature profile of Fig. 4.19: between surface 1 and surface 24, i.e. along the combustion chamber length, the temperature raises following a quadratic-like curve from 2566 K - an estimated value associated to the combustion gases in the proximity of the faceplate as obtained in Sec. 5.3.5 - up to 2913 K, which is the chamber temperature as given back by the CEA tool. This choice reflects the attempt to take into account the passive cooling strategy adopted in the combustion chamber.
- convective BC2 upon the vertical wall of the combustion chamber pertaining to the faceplate. In Sec. 5.3.5 a heat transfer coefficient of  $507 \text{ W/m}^2$

and a bulk temperature of 2566 K have been calculated for this boundary.

- convective BC3 on the borders of the coolant channel being part of the regenerative cooling system adopted on the injector plate. Again, in section 5.3.5 the local heat transfer coefficient has been quantified in  $4359 \text{ W/m}^2$ , while the bulk fluid temperature is the stagnation temperature of the ethanol coming from the tank, which ultimately is equal to the ambient temperature of 273.15 K, a value chosen accordingly to the average temperature for the month of february in Dresden (the upcoming test campaign is scheduled for mid-February).

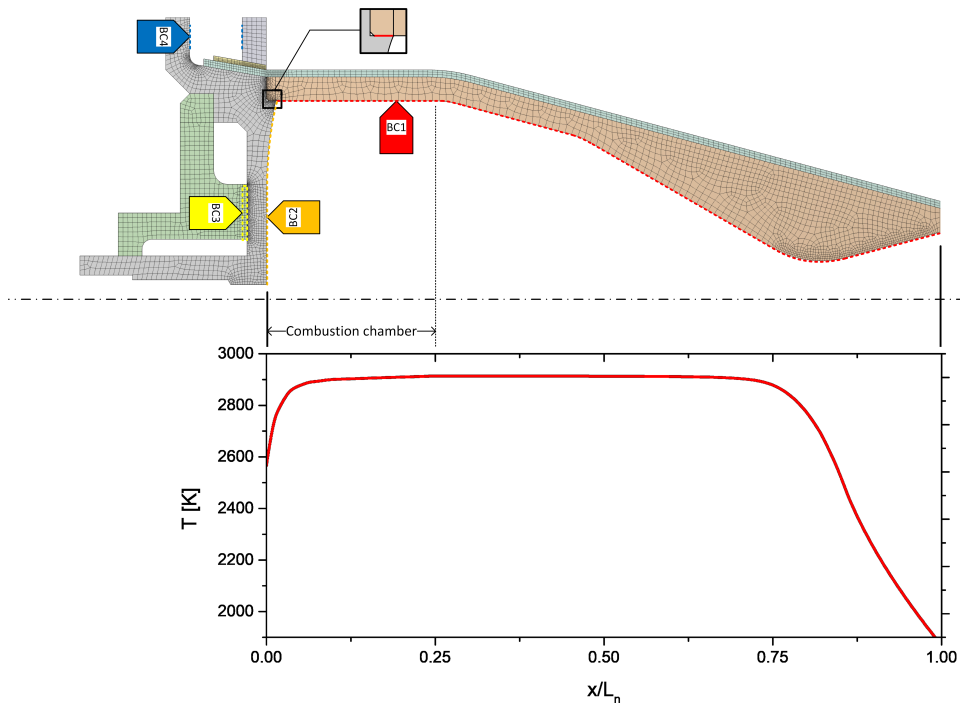


**Figure 4.19:** Applied boundary conditions on the thrust chamber and meshing process result

Besides the thermal BCs, an extra one is required in order to properly constraint the rocket engine structure, thus preventing rigid body motion. To this purpose, fixed support BC4 is applied on the fastening points of the assembly to the engine mount. No more structural constraints are imposed in order to assess no other stress field but the thermal one. Furthermore the contact between the different bodies of the assembly has been specified as:

- bonded for the faceplate-backplate interface, since they are brazed together with a nickel brazing paste

- no separation for the rest, meaning that separation of the geometries in contact is not allowed

In Fig. 4.19 is also showed the result of the meshing process for the selected geometry. In order to ensure a consistent and regular mesh, a method involving both quadratic and triangular bidimensional plane elements has been employed and the element size parameter has been varied until convergence in the results has been struck. One can notice that the mesh is denser in the near throat region: on the inner wall contour indeed, a matching with the 179 points contour discretization so far adopted is realized, so that the mesh follows the discretization, adapting to it. Other dense-mesh areas can be spotted on the injector plate as a result of a refinement aimed at finely scoping the local thermal stress field.

#### 4.4.2 Results and discussion

The two stage resolution of the problem operated by the program - first thermal, then structural - results in the transient response of the system, basically quantified in terms of four magnitudes of interest, namely temperature, heat flux, deformation and stress on the structure. During the transient state operation of the engine no thermal equilibrium is reached, for the time span of fire is too short: starting from the initial ambient value of 273.15 K, temperature can do anything but raise, and so will do the other magnitudes involved. For this reason, the results of the thermal-structural analysis are presented at the supposed tail-off instant  $\tau = 20\text{s}$ , which plainly corresponds to the peak in thermal-mechanical stress for the system.

##### Thermal response

The temperature distribution comes to view in Fig. 4.20. What catches the eye at the very first sight is the net separation between the nozzle body on the left and the injector head on the right, marked in terms of colour shades associated to the temperature field: reddish the former, while deep bluish the latter, meaning that most of the heat is generated on the wall of the nozzle and therein stored, with the injector plate kept relatively cool over the burning time. Such a distribution mirrors accurate design choices - the heat-sink configuration adopted for the thrust chambers as well as the regenerative cooling strategy implemented on the injector plate - and makes perfect sense when analyzing it from the selected materials' viewpoint. Indeed a comparison between the graphite of the nozzle and the steel of the faceplate in terms of the thermal diffusivity  $D$ , reveals that the former has a as much higher as twice heat diffusion capacity than the latter, which means a faster heat propagation in the nozzle over the firing time:

$$D = \frac{k}{C\rho} \Rightarrow \frac{D_{Graph}}{D_{Steel}} = \frac{10^{-5}\text{m}^2/\text{s}}{0.45 \cdot 10^{-5}\text{m}^2/\text{s}} \approx 2$$

One last detail from Fig. 4.20: it can be noticed that the iso-temperature map over the straight cylindrical portion of the chamber, exhibits a "redshift" as the convergent-starting point is approached from the faceplate, resulting in the orange region covering the 15 deg convergent tract of the graphite nozzle. This is a consequence of the temperature distribution in Fig. 4.19 - with particular reference to the increasing tract of the curve - adopted in the attempt to take into account the passive cooling strategy in the combustion chamber, involving the outer cone of fuel sprayed out from the injector.

Fig. 4.21 shifts attention to the injector head. The uniform low-temperature field in the rear part of it is basically perturbed by two sources of heat, i.e. the combustion and the resulting chamber-wall convection on the one hand and the heat transmitted by conduction at the nozzle-faceplate interface on the other hand. These two sources combine in a hot front trying to make its way through the injector head counteracted by the breaking action - appearing clear in Fig. 4.21a - exerted by the cold ethanol flowing in the coolant channel after being gathered in the outer collector ring. On the same figure, a magnified detail of the temperature associated to the walls wetted by the ethanol can be observed: temperature ranges from 284 K up to a maximum of 531 K. Given a tank-chamber pressure differential of 10 bar, the ethanol boiling point of  $\sim 450$  K is nowhere exceeded to such a point that film boiling phenomena take place (Huzel et al. [3] indicates an excess of at least 278 K in order to trigger film boiling).

Temperature profiles across the wall at three different stations are graphed in Fig. 4.22. They feature numerical results as given back by the ANSYS as well as the theoretical steady-state estimations of subsection 5.3.7. The red horizontal lines crossing the wall in its whole thickness, marks the materials limit in terms of maximum service temperature. Then, the first thing to point out is that the limit is nowhere overcome, with a margin of 50% at least. As predictable, forced convection at wall plays the key-role in temperature abatement and in the near throat zone the temperature field reaches its peak. Focusing on the thrust chamber, one should note how the linear temperature profile becomes steeper across the ceramic thickness, indicating a more insulative behavior of the OCMC. The throat station is a well defined spot on the thrust chamber, whereas the other two stations have been chosen so as to match the locations of temperature sensors TC $\emptyset$  (on the chamber), TC6 and TC7 (on the faceplate). Once experimental data will be available, a temperature comparison with numerical solutions over these spots will confirm or deny our predictions.

In Fig. 4.23 the heat flux density over the nozzle is mapped in the form of a vectors distribution. As one could already infer by inspecting the temperature distribution, there are two main critical zone with regard to the heat transfer. The first one is of course the throat region where the maximum heat flux is registered. The other one is the nozzle-faceplate attachment. Indeed the heat flux acting upon the nozzle has a predominant radial component, except on the interface surface with the injector head where the heat flux becomes mainly axial in direction. As expected, on the injector plate the heat flux becomes significant

along the coolant channel, particularly beside the inlet and outlet sections. Finally the total heat flux and temperature distribution are plotted against the normalized nozzle axial distance in Fig. 4.24. Both the curves reach their peak at a station located slightly before the throat. The local peak of around  $1.8 \text{ MW/m}^2$  at  $x = 0$  represents the heat flux transferring from the heated-through nozzle into the faceplate. Another local peak, this time pertaining to the temperature curve, is localized on the 15 deg convergent tract of the nozzle. The corresponding hill is explained by the way the gas temperature is modeled along the straight cylindrical portion of the nozzle, that is, an increasing function from 2566 K on the faceplate up to 2913 K at the end of the combustion chamber (see Fig. 4.19), which also causes the "redshift" in the temperature map over the same region, mentioned earlier while describing the temperature distribution in Fig. 4.20.

### Structural response

The thermal field analyzed in the previous section affects the structural response of the system (but not contrariwise, given the unidirectionality of the thermal-structural analysis performed). Particularly the temperature distribution after the 20 s of firing induces deformation on the structure and consequently thermal-mechanical stress arises.

The total deformation is depicted in Fig. 4.25. Basically the nozzle assembly seems to expand with the injector plate supporting its deformation. During the firing time, the large heat fluxes acting upon the nozzle wall promote a fast heat accumulation within the structure, as well as a rise in temperature which ultimately feeds its deformation, both in the radial and in the axial direction. The maximum deformation of  $\sim 1.5 \text{ mm}$  is experimented by the free end of the nozzle. On the other hand, only the lower part of the injector plate undergoes significant deformation with a local maximum of less than half a millimeter occurring on the injector bay.

Let us now focus on the stress distribution in Fig. 4.26. The steel injector plate appears to be the most stressed area. Now, for a given average temperature of 495 K acting on it at  $\tau = 20 \text{ s}$ , the austenitic stainless steel which the injector head is made up of, presents a tensile strength of  $\sim 500 \text{ MPa}$ , which never gets exceeded. The only exception could be a critical zone on the faceplate as one can see in Fig. 4.27 - namely the only filleted concave corner present on the faceplate, where the stress locally increases up to its maximum of 591 MPa - a value dangerously above the ultimate strength aforementioned. The local stress concentration is explained by describing the way the assembly deforms under thermal loading for the imposed structural constraints. Basically it behaves like an L-shaped cantilever clamped on its shorter side (see Fig. 4.30): the net result of the materials' expansion under the calculated thermal loading is a clockwise rotation of the structure and consequently, a concentration of compressive stress in the rounded corner, for the imposed structural constraints. But when extrapolating the local temperature, one finds out it varies in the range 290 – 320 K,

with an average value of 305 K, a typical room temperature, at which the faceplate material performs at its best (datasheets ensure a tensile strength up to 750 MPa). This spot apart, no other regions in the stress field are reported as remarkable enough to threaten the structural integrity of the injector head.

Needless to say that the near-throat region undergoes the maximum stress when considering the sole graphite inlay as in Fig. 4.28. The stress peak, amounting to  $\sim 42$  MPa, is well above the 35 MPa tensile limit of the material, as measured at room temperature. It has to be pointed out that graphite has the unique feature in the realm of engineering materials of exhibiting a growing tensile strength as temperature increases. This change in the mechanical characteristics of the material can be dramatic with a 100% increase. At any rate graphite is also brittle in nature and the strong thermal loading in the near-throat region might enhance erosion.

No concerning spots are reported on the ceramic shell in Fig. 4.29. The selected OCMC material presents an ultimate strength amounting to  $\sim 200$  MPa, which is never exceeded. The maximum strength is located on the interface with the clamping ring, where the ceramic shell is locally squashed by the graphite inlay and the steel faceplate expanding in concert on the bottom border and the clamping ring on the top, while trying to expand itself, subject to thermal loading.

#### 4.4.3 A tridimensional analysis focused on the injector plate

The axisymmetric shape of the assembly allowed us to run a bidimensional analysis, thus favourably trading a tiny loss in precision for large computational savings. As already mentioned before, this not applies to the injector plate, where a single sided ethanol inlet breaks its rotational symmetry. As a consequence, the temperature field itself is not axisymmetric. Furthermore a bidimensional analysis does not allow to exactly reproduce the way the engine is fastened, which undoubtedly affects the stress distribution over the faceplate. In order to investigate the effect of the ethanol inlet as well as the effect of the actual fastening system, an additional tridimensional analysis has been performed. The geometry switches from 2D to 3D, while materials' properties and meshing parameters remain unchanged. An additional convective boundary condition on the inner wall of the inlet is required. Given the geometry of the section and the ethanol's mass flow and dynamic viscosity, the local Reynolds number is readily estimated as follows:

$$\left\{ \begin{array}{l} D = 0.004 \text{ m} \\ \dot{m}_c = 0.11136 \text{ Kg/s} \\ \mu_c = 1.792 \cdot 10^{-3} \text{ Ns/m}^2 \\ Re = \frac{4\dot{m}_c}{m u_c \pi D} = 20179 \Rightarrow \text{turbulent flow} \end{array} \right.$$

Then the Gnielinski correlation for turbulent flow allows an estimation of the Nusselt number:

$$Nu = \frac{f/8(Re_{RC} - 1000) Pr}{1 + 12.7(Pr^{2/3} - 1)(f/8)^{1/2}} = 234$$

where the Prandtl number for the ethanol is fixed on 23, as in the previous calculations involving the coolant, while the friction factor is obtained from the following correlation provided by Petukhov:

$$f = (0.79 \ln(Re_{RC}) - 1.64)^{-2} = 0.0261$$

The following convective coefficient is the final result of the heat transfer modeling in the ethanol inlet:

$$h = \frac{Nu K_c}{D_H} = 10200 \text{ W/m}^2$$

Since extra steel-made bodies have been created and added - namely the sixteen bolted joints which fasten the engine to a fixed square panel - new contacts between bodies had to be defined. Particularly on the square panel's surfaces facing the clamping ring on one side and the faceplate on the other, frictional contacts have been introduced with a coefficient of 0.2, a typical value for steel-on-steel friction. As for the rest of the contacts, they contribute, along with a bolt pretension BC on each of the bolts, to model the bolted joints. The additional boundary conditions can be visualized in Fig. 4.31.

In Fig. 4.32 is shown the resulting temperature distribution on the injector plate. When compared with the two-dimensional distribution in Fig. 4.21, the two isotherm lines map could overlap in a perfect matching. Focusing now on the ethanol inlet zone, it is plain that the temperature distribution appears perfectly axisymmetric. By visual inspection seems that no significant effect is produced by the ethanol flow in the inlet on the temperature field, not even locally. This is confirmed by the temperature values in the near-inlet zone, which differs by approximately ten degrees Kelvin from its diametrically opposed counterpart on the backplate. In conclusion, the backward position of the inlet - too far from the combustion chamber border on the faceplate - does not allow it to affect the temperature field on a remarkable extent, not even on a local radius. In addition the stagnating ethanol in the outer collector ring in between, plays an insulating role, thus inhibiting any heat removal by the inlet.

Remarkable instead is the extent to which the tridimensional modeling of the fastening system affects the faceplate stress distribution, in Fig. 4.33. The peak of 329 MPa does not take place anymore on the rounded corner of the backplate, but rather on the border of the clearance holes. The steel panel between the faceplate and the clamping ring allows a partial absorption and redistribution of the stress, which is locally lowered in comparison with the bidimensional case. A local peak is located on the outmost circular border of the combustion

chamber, at the interface with the nozzle, where local large fluxes introduce heat into the faceplate. For a local temperature of 820 K, the stainless steel ensures a tensile strength of  $\sim 400$  MPa, which is not exceeded by an encouraging margin of more than a hundred megapascal. On the hot gas side, one can clearly spot the trace of the forty coolant channels system - which lowers the temperature and consequently the stress - consisting in the pale-blue circular strip between the combustion nucleus, surrounding the injector housing, and the outer yellowish stripe, where the cooling effect fades and the heat transmission operated by the hot gas convection becomes predominant, culminating in the local maximum stress on the outmost border of the chamber, where, again, the greatest contribution to local stress rise, lies in the heat fluxes moving from the nozzle into the faceplate.

Additional effects of the fastening system as modeled in the tridimensional analysis, include a total deformation of the nozzle which is globally smaller than the one pertaining to the 2D case, with a maximum of  $\approx 0.82$ mm occurring again on the nozzle exit, and a stress peak on the ceramic shell of  $\approx 123$ MPa, 23% higher than its 2D equivalent on the same spot, but still well below the tensile limit of the OCMC material.

#### 4.4.4 Highlights and conclusions

We started this chapter by addressing the following question: for the given geometry and the selected materials, will the engine withstand the thermal-mechanical loads and the resulting stresses without critical failure?

Yes, it will. In general the observed thermal stress fields confirm that the whole structure would operate within a reasonable thermal and structural envelope, meaning that crucial design choices, such as the adoption of a heat-sink layout for the thrust chamber - and the consequent materials selection - as well as the cooling strategies implemented on the injector plate and the chamber walls, have been numerically validated under reasonable assumptions. There could be an underside, hidden among our assumptions, as one could argue that the radiative heat transfer neglects cuts out the heat added by radiation from the combustion gases, which usually accounts for the 5% – 32% of the total heat transferred to the wall. But, on the flip side, no heat is supposed to radiate in the ambient as well - and it would partially relieve the thermal loading on the thrust chamber - and this hypothesis along with the worst-case scenario values picked for the graphite thermal properties, compensate for the expected radiative flux in the combustion chamber. Thus the adopted assumptions auto-balance all together in the model. It is also stressed a point not mentioned so far: the maximum service temperature and the properties of the selected materials are referred to a long-term exposure to high temperatures (e.g. in [23], it is explained how the degradation of oxide-oxide composites occurs quickly at 1200°C, *well within 100 hours*). Our rocket engine is fired for few seconds, ensuring further confidence in the structure's durability.

What seemed to jeopardize the structural integrity was the highly stressed spot localized on the faceplate, where local stress exceeded the ultimate limit of the material. But the subsequent tridimensional analysis - with an overall geometry and fastening system closer to the ones actually adopted on the rocket engine - made us confident that the material will not undergo any critical rupture. As for the rest of the engine, on the injector plate some plastic deformation is expected - particularly on high-heat flux areas such as the nozzle-faceplate interface and along the border in contact with the coolant channel - and the throat region might undergo erosion, although it is barely predictable. At any rate, nowhere the local temperature is high enough to lower the mechanical properties of any of the employed materials, down to a failure point.

To sum up, the achieved results are first of all plausible, that is, in line with the expectations from the functioning of a properly-designed rocket thrust chamber. In addition, when analyzed in detail, they have proved to be consistent with design choices adopted specifically for our rocket. Finally, focusing on the numbers, they are not alarming, in the sense that, although drawing attention to some (in any case predictable) hotspots, they do not represent a real threat for a safe operation of the rocket and even if an optimization process was started for enhancing the thrust chamber response in terms of thermal stress, it would not impact the design in an expensive way.

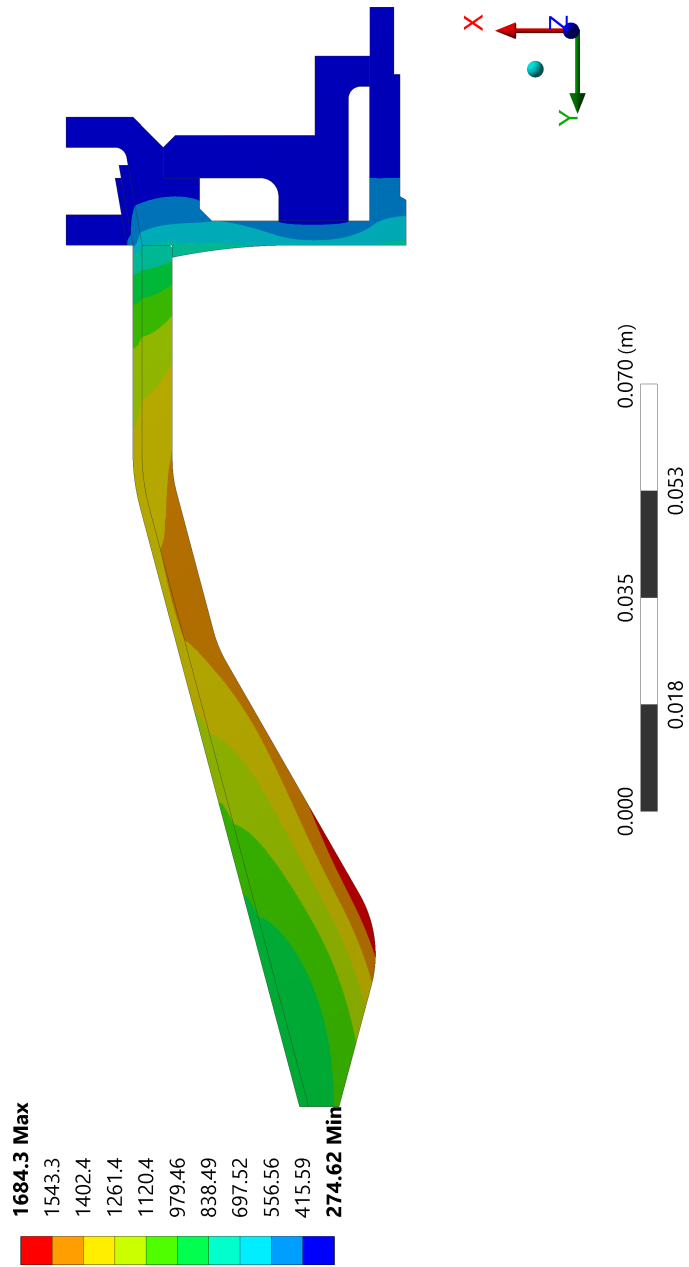
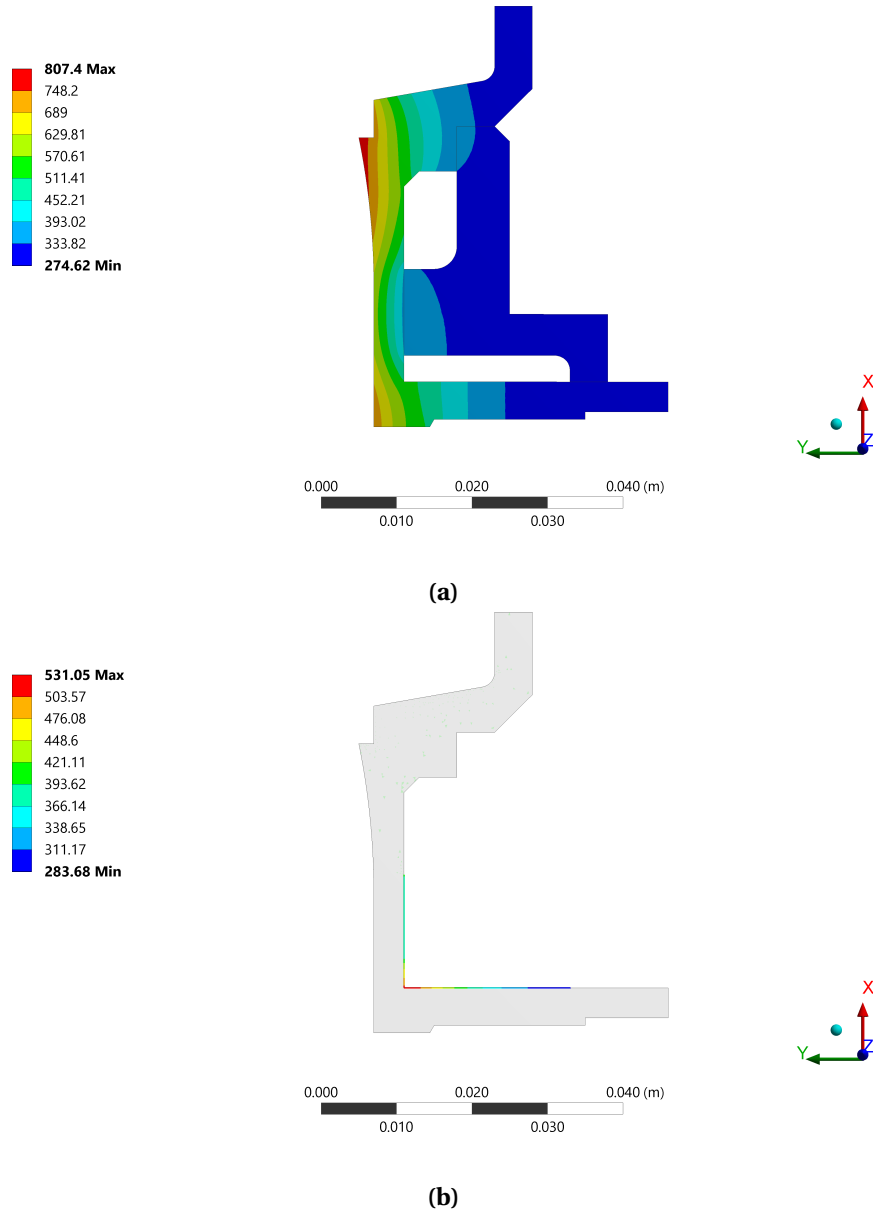
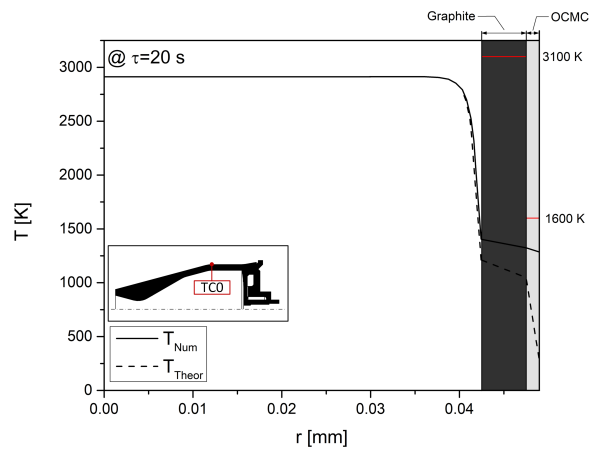


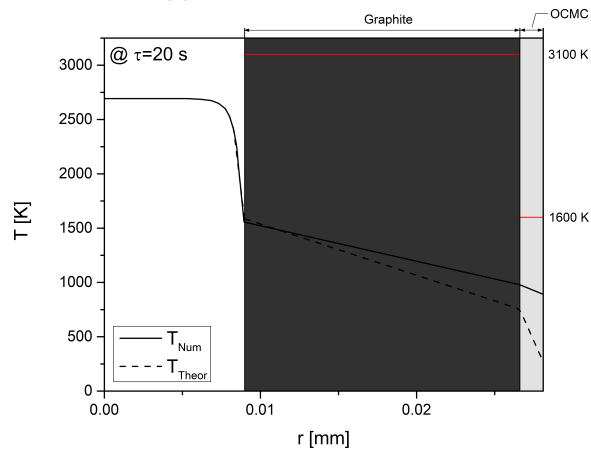
Figure 4.20: Temperature distribution [K] at  $\tau = 20s$



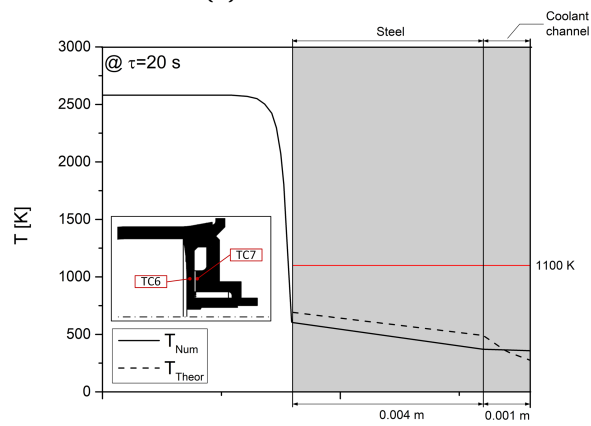
**Figure 4.21:** Temperature distribution [K] on the faceplate at  $\tau = 20$  s



(a) Chamber station TCØ



(b) Throat station



(c) Faceplate station TC6 and TC7

Figure 4.22: Temperature profiles [K] in different stations

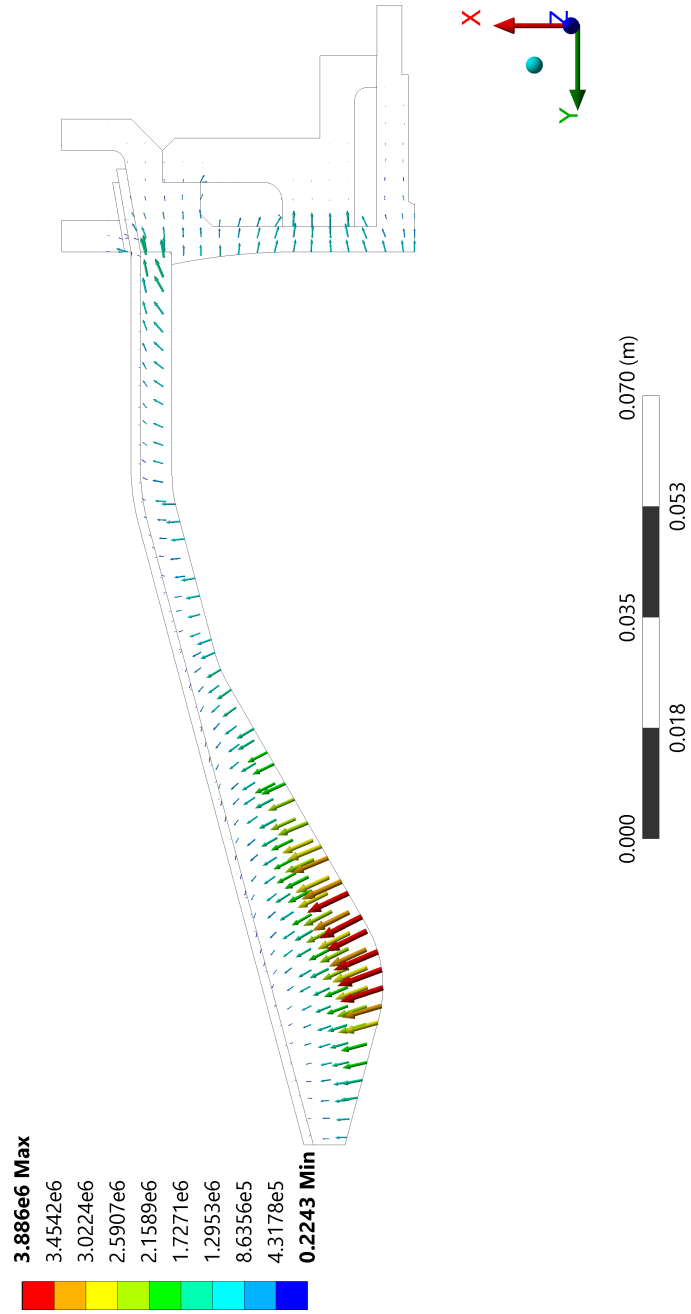
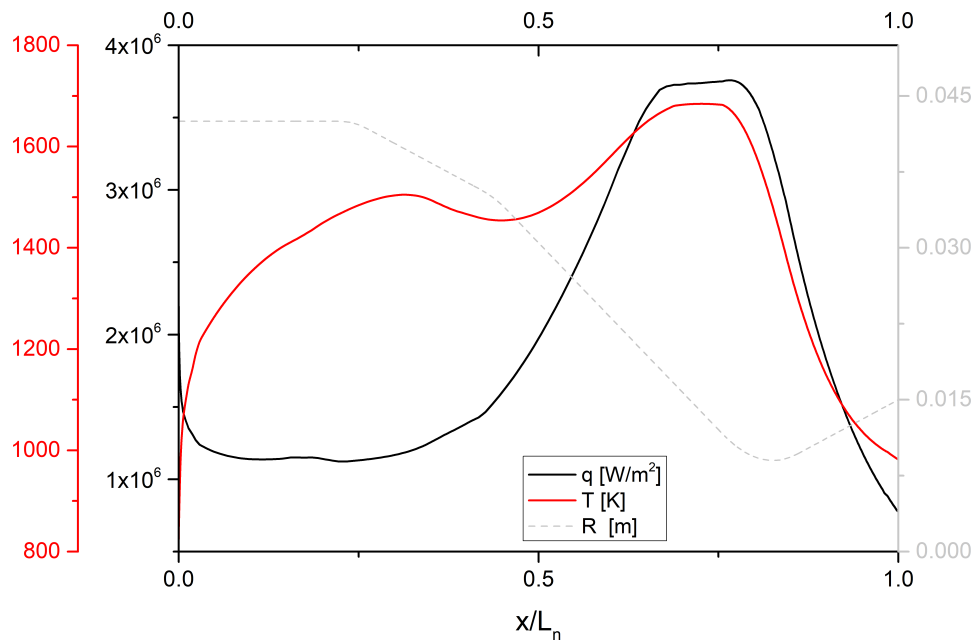
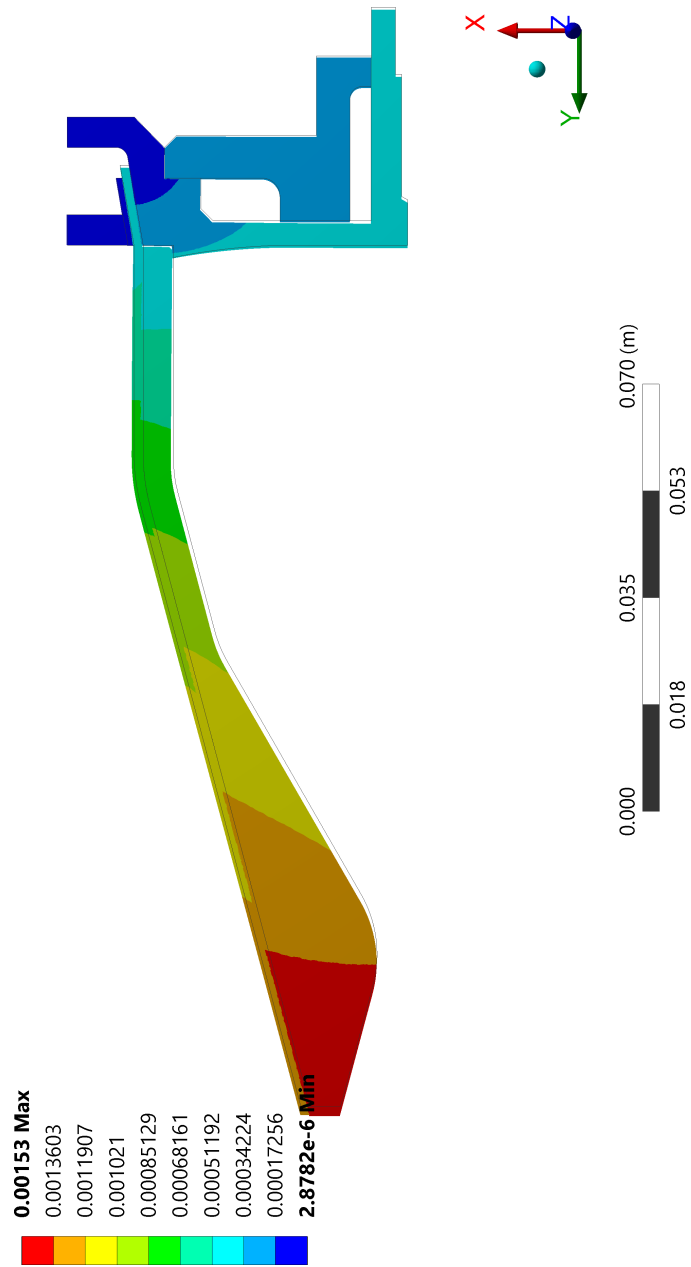


Figure 4.23: Heat flux density mapping [W/m<sup>2</sup>] at  $\tau = 20s$



**Figure 4.24:** Temperature and total heat flux distribution along the nozzle at  $\tau = 20s$



**Figure 4.25:** Total deformation of the structure [m] at  $\tau = 20$ s

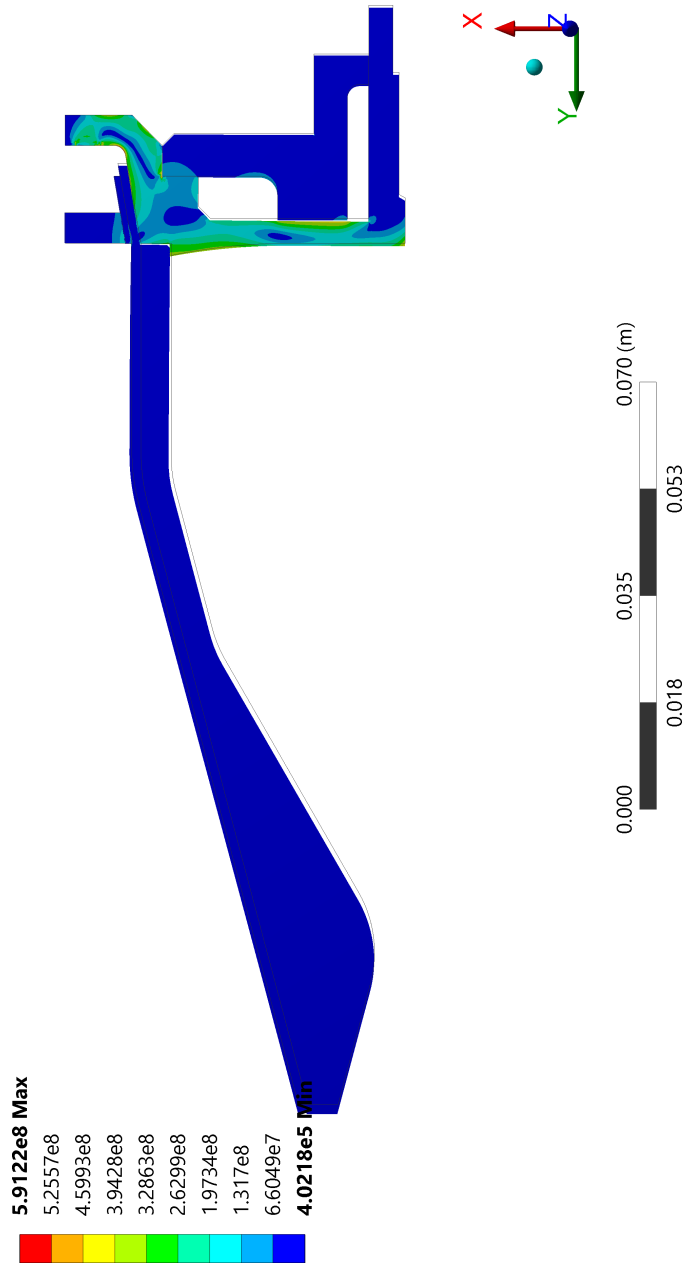


**Figure 4.26:** Von Mises stress distribution [Pa] at  $\tau = 20s$

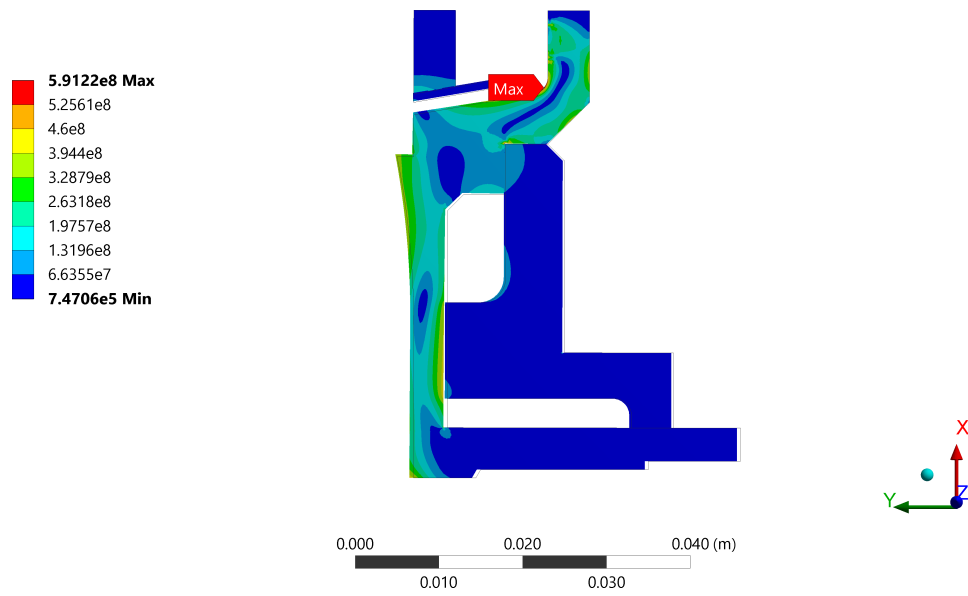


**Figure 4.27:** Steel injector plate stress distribution [Pa] at  $\tau = 20s$

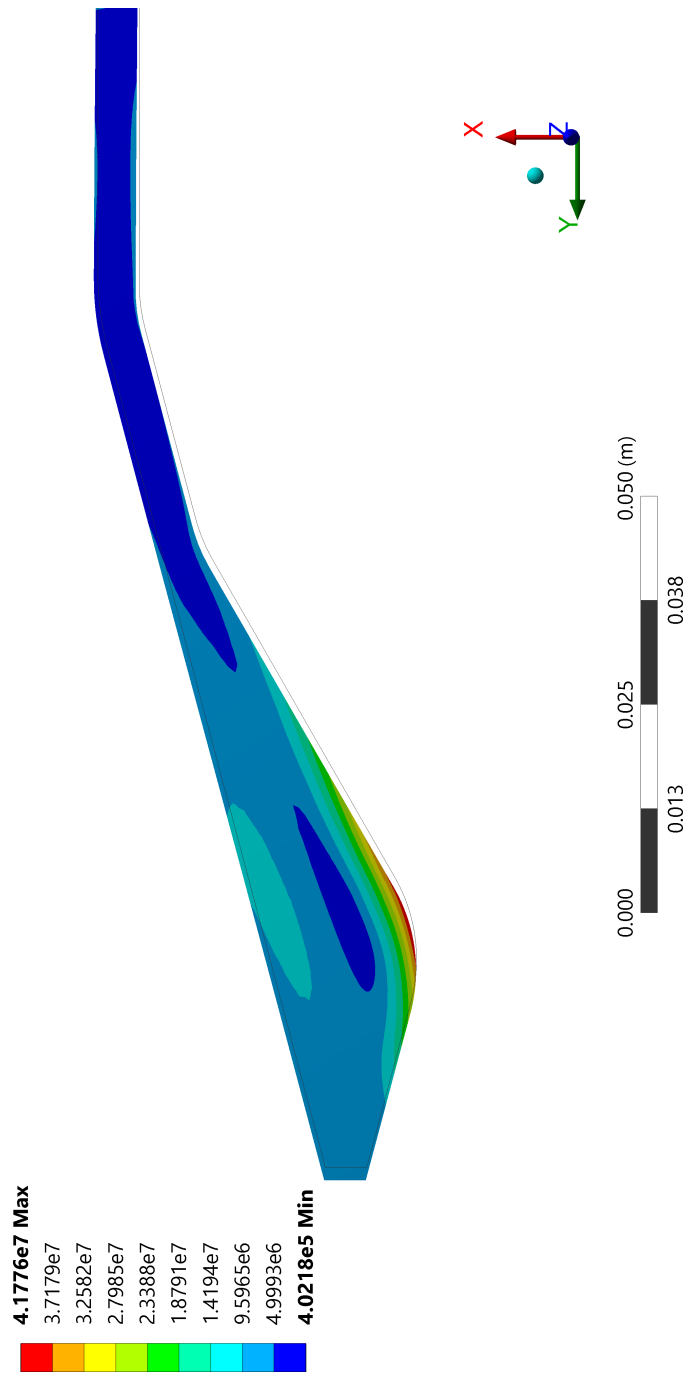


Figure 4.28: Graphite inlay stress distribution [Pa] at  $\tau = 20s$

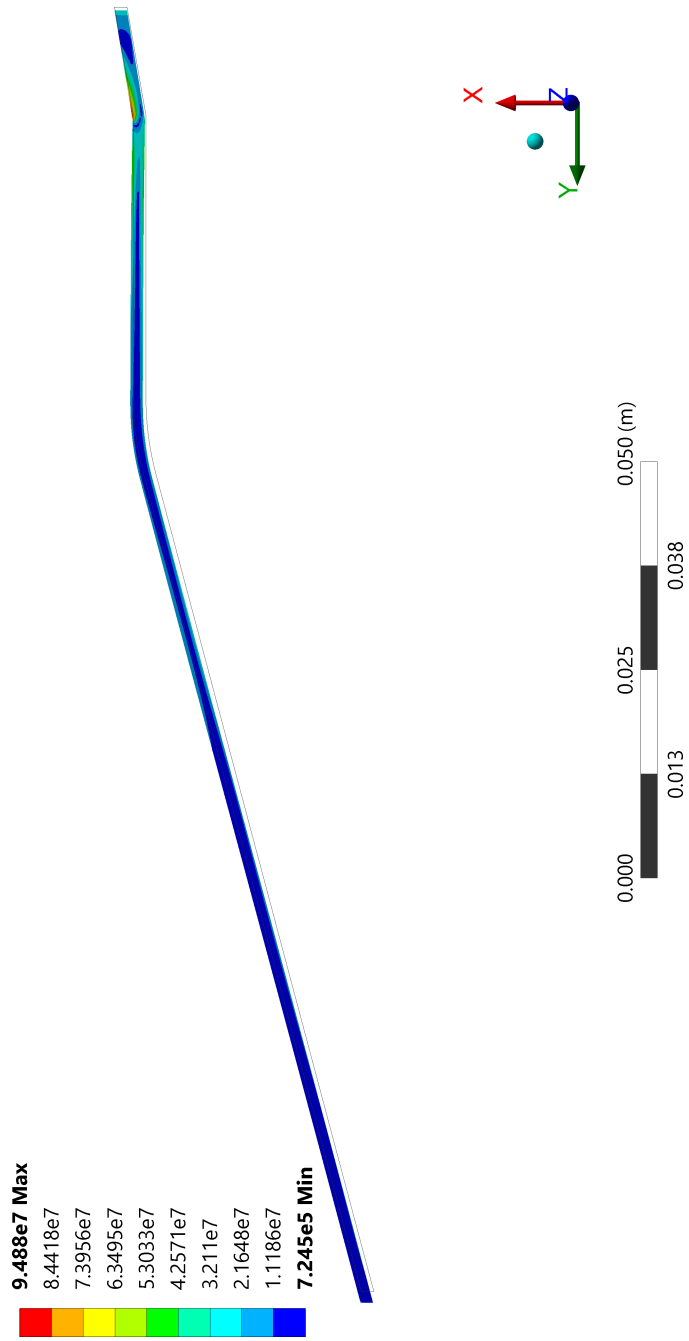
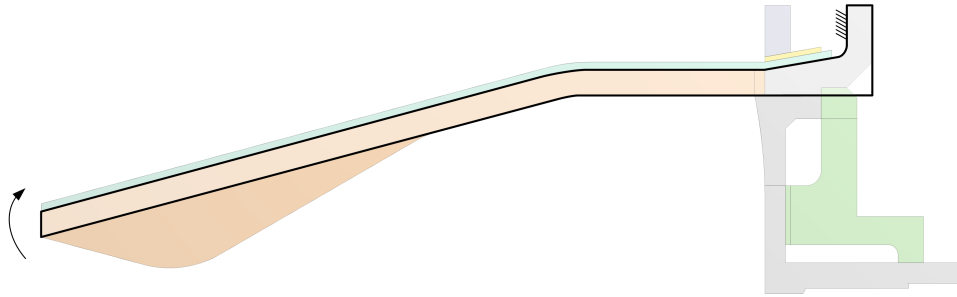
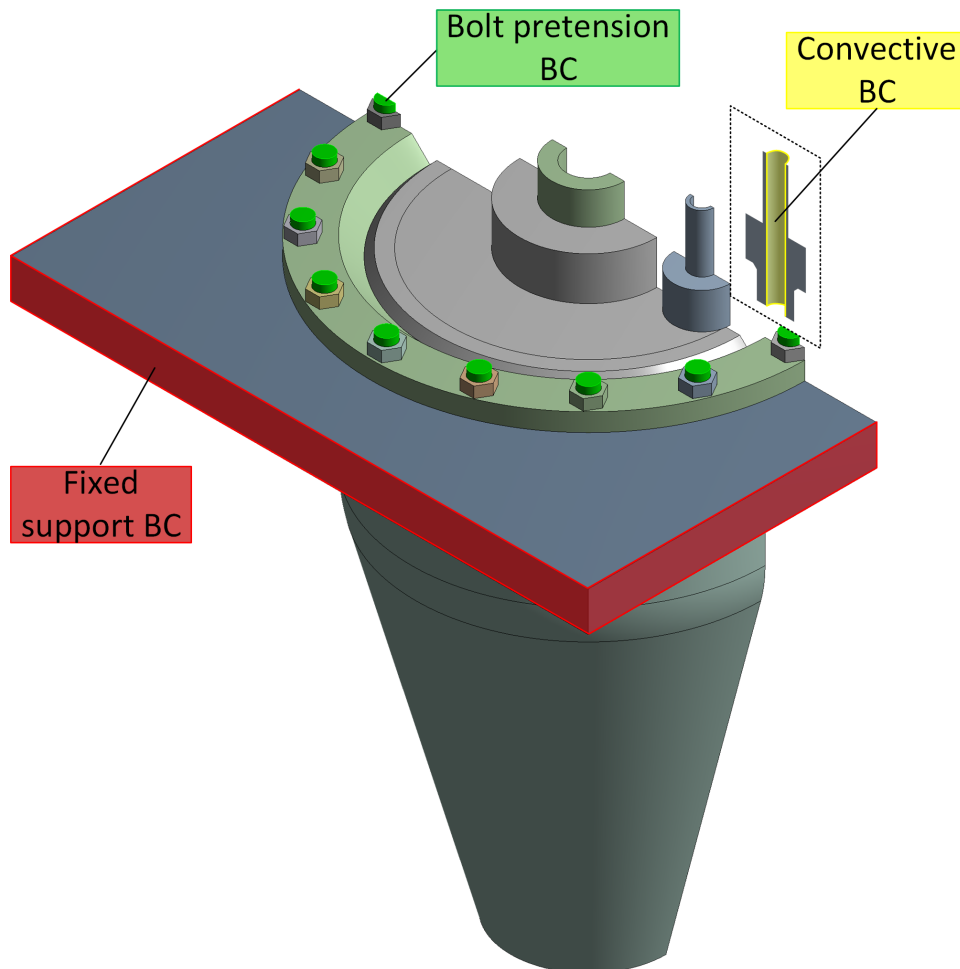


Figure 4.29: Ceramic shell stress distribution [Pa] at  $\tau = 20$ s



**Figure 4.30:** Global deformation of the assembly under thermal loading



**Figure 4.31:** Additional boundary conditions for the tridimensional analysis

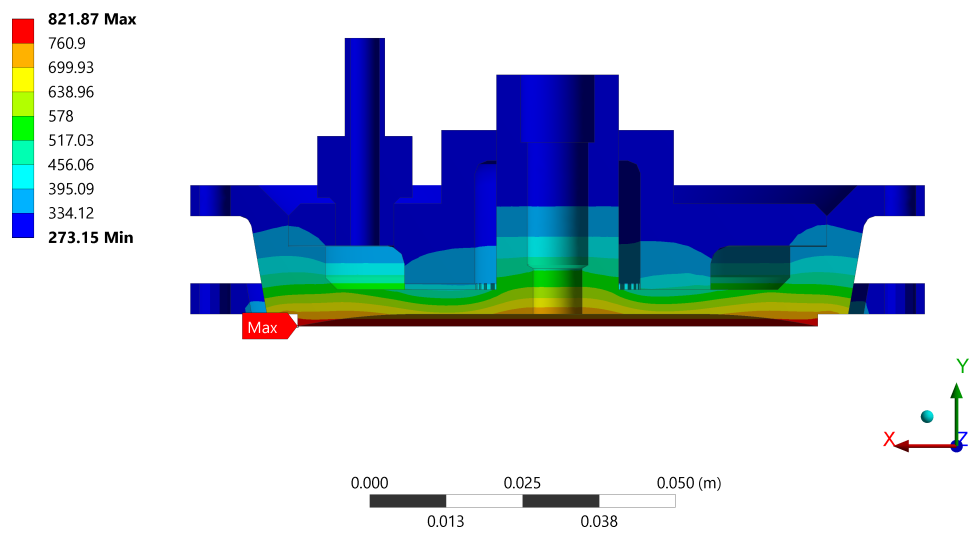


**Figure 4.32:** Temperature distribution [K] on the three-dimensional injector plate at  $\tau = 20\text{s}$

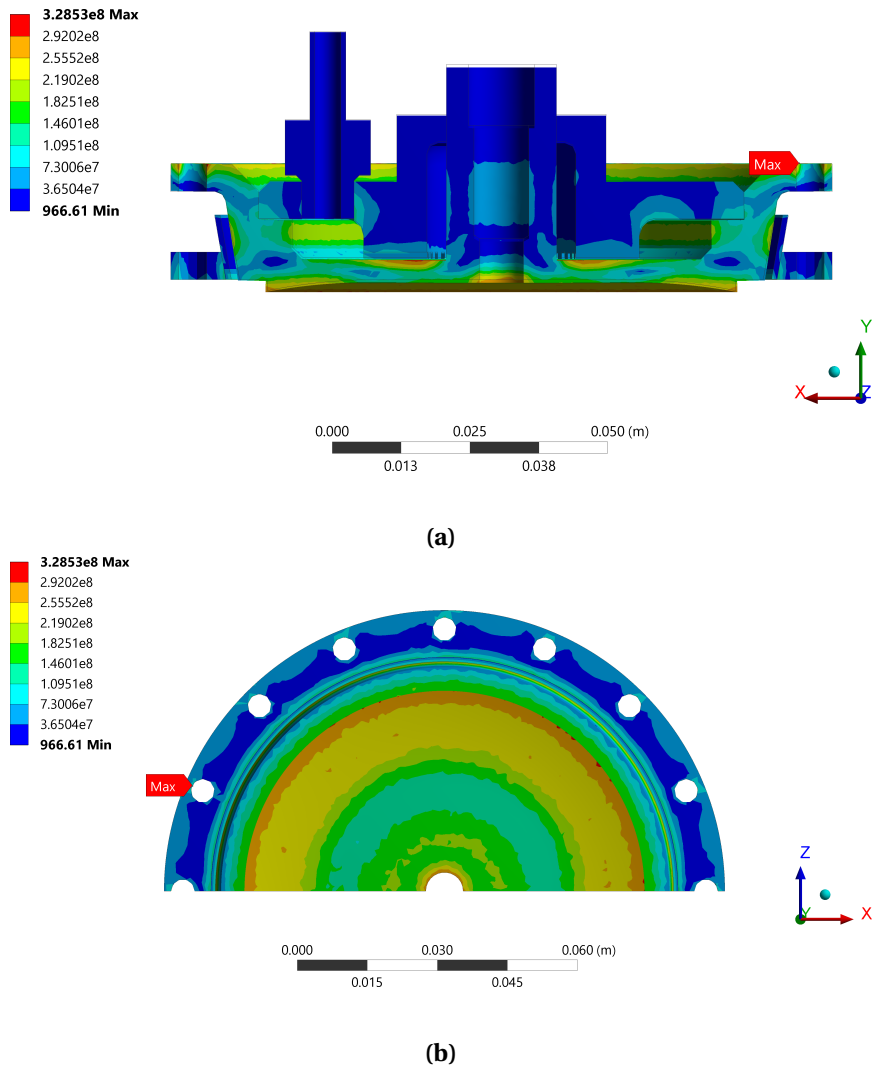


**Figure 4.33:** Stress distribution [Pa] on the three-dimensional injector plate at  $\tau = 20s$



## Chapter 5

# Test-firing the flight model of the engine

The upcoming test campaign represents a crucial step in the overall design and development process of the engine, which culminated in the manufacturing of its flight model, i.e. the hardware that - once satisfactorily test-proven - will actually equip and propel the rocket. Particularly, the series of fire tests is aimed at verifying the capability of the engine to deliver performance in line with the expected values, predicted via theoretical calculations involving well-established design parameters. Furthermore, the predictions on the thermal-structural behaviour of the engine, which originate from the numerical analysis performed in the previous chapter, are pending reliable test data, in order to get verified.

### 5.1 Flight model concept

The achievement of a flight readiness status for the flight model of the engine, depends upon the outcome of the envisaged fire tests. The last campaign, dating back to November 2015, has already test-verified the basic flight configuration, comprising a graphite nozzle housed by an OCMC shell and backed by a stainless steel injector plate. Particularly, firing #122 from that test series, registered the highest value of thrust of 470 N, given a mixture ratio of 1.1 resulting from mass flows of 0.120 Kg/s and 0.135 Kg/s, for ethanol and LOX respectively, thus proving the ability of the engine to produce the expected thrust level and validating the graphite-OCMC-steel trio of selected materials for the flight hardware. In the meantime, the engine design has evolved towards the flight model: the materials involved are the same as in the last concept tested, while modifications affected the geometry as well as the mixture ratio. Specifically, the current geometry features:

- a shorter overall thrust chamber length

- a double cone profile (15 deg and 30 deg apertures) on the convergent portion of the nozzle
- a larger combustion chamber cross section area - as a consequence of a wider aperture angle for the first cone - i.e. a higher contraction ratio given the fixed throat section

The current geometry, as a matter of fact, globally implies a decreasing characteristic length and consequently, being  $L^*$  essentially a function of the stay time  $t_s$ , a shorter dwell time for the combustion gases in the chamber. So potentially, the risk of incomplete combustion and poorer performance has increased. As stated in [3], small chambers typically employ a large contraction area ratio -  $A_c/A_t = 23$  in our case - with a shorter length, while still providing sufficient  $L^*$  for adequate vaporization and combustion dwell-time. Then how much is 'sufficient'? Huzel et al. in [3] plotted the chamber length as a function of the throat diameter for several previously successful design. The plot is reproduced in Fig. 5.1, where the curve point corresponding to our engine's throat diameter is marked with a black triangle: our engine, according to Huzel's interpolation, should feature a 9.3 cm chamber in place of the current design's 3.85 cm. Already in 1956 [28] was known that, as a rule of thumb, for a very squat chamber the maximum efficiency is reached at a high value of the characteristic length. In conclusion, a comparison with historical data, seems to suggest an increase in the chamber length, for the sake of performance. As for the mixture ratio, switching to a less fuel-rich value, on the one hand implies a performance closer to the optimum, but on the other hand means the chamber shall withstand a higher combustion temperature. One last design change concerns the thickness and diameter of the injector head, which have both been reduced. Fig. 5.2, well summarizes the modifications which affected the last engineering model tested, thus resulting in the current flight model design.

Now given the above discussed design, the upcoming test campaign shall verify it in terms of performance by actual firing of the hardware. One crucial objective is the achievement of a thrust of 500 N by realizing the prescribed 1.2 mixture ratio for the propellants. Furthermore the current configuration layout will be tested against the increasing heat load resulting from switching to a less fuel-rich mixture ratio, although results from the thermal-mechanical analysis in the previous chapter seem promising in that sense.

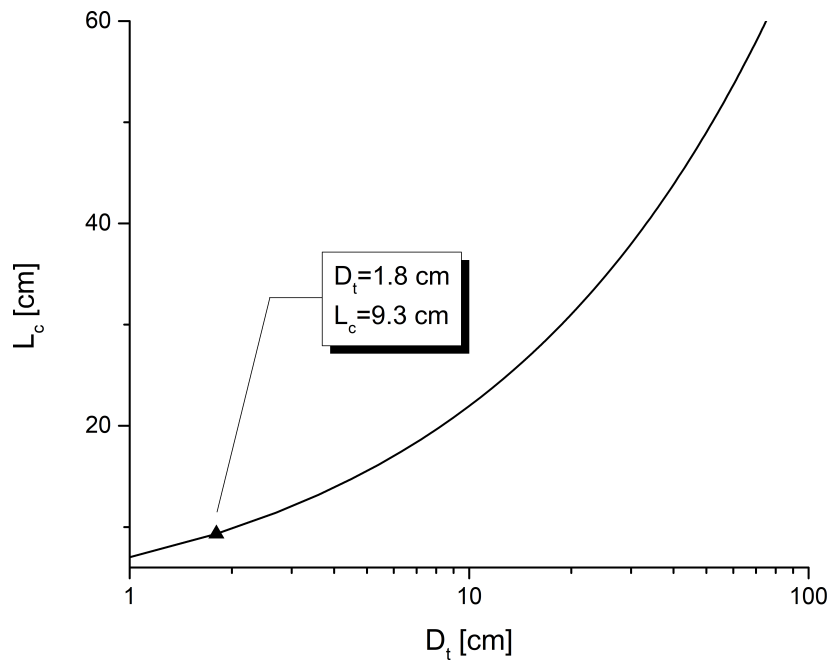


Figure 5.1: Chamber length as a function of throat diameter

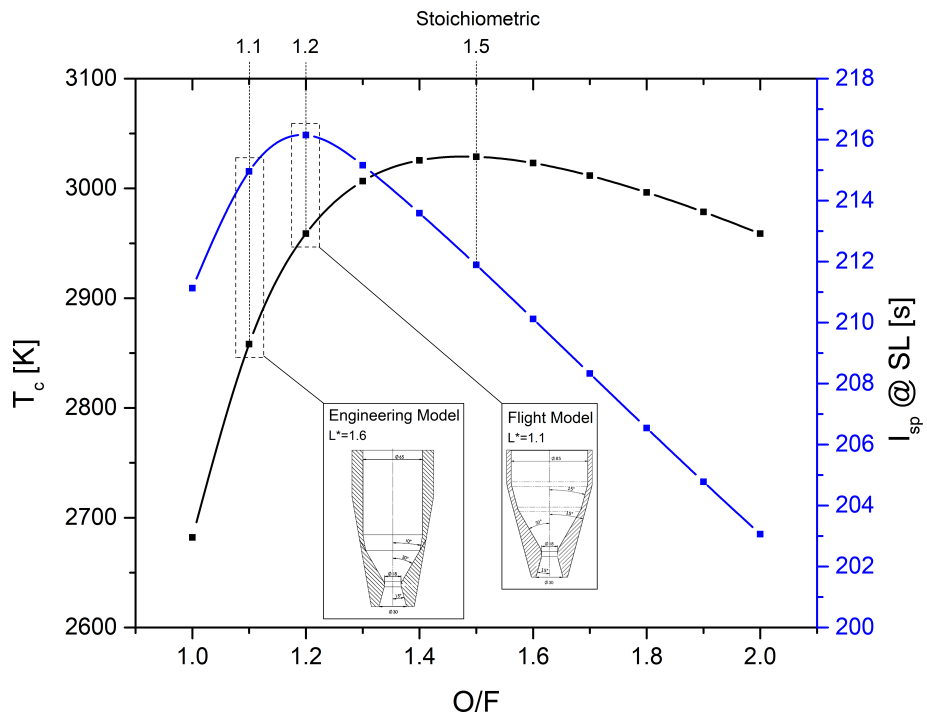


Figure 5.2: Comparison: engineering model vs flight model

## 5.2 Test campaign for the flight model

The last test campaign, which took place, under winterly conditions, between february and march 2017, started the qualifying iter of the 500 N LOX/Eth70 rocket engine in its flight configuration. The test session opened with cold flow tests, followed by open combustion firings, and eventually closed with a series of firings involving the complete flight hardware.

### 5.2.1 Highlights from the campaign

The actual starting of the series of tests on the engine, was preceded by a preparatory phase, during which the test facility was set up, including the data acquisition system - comprising the sensors suite described in Chapter 4 - and the test bench, both connected to the injector plate, fastened to the mount in its under-test configuration. Once the proper connection and integration of the whole test hardware has been checked, the first flow tests were conducted. The intent was to ensure that the system will not leak during pre-launch and flight operations and to verify the ability of the control system to perform mixture ratio excursions, in order to tune the propellants' mass flows, thus proving that their values fall within requirement limits. Thereafter, open combustion tests have followed for hot-fire verification of the ignition system and subsequently the thrust chamber assembly has been mounted, thus readying the engine unit for performance-evaluation firings. A total of seven firings was performed, numbered from #130 to #136. During test #131 the engine experienced a failure of the clamping ring which resulted in a separation of the thrust chamber from the injector plate. The consequent, violent impact with the ground permanently damaged the OCMC shell, forcing the team to put the test-campaign on hold. The quick redesign of the ring in order to more tightly hold the thrust chamber against the injector plate, allowed the campaign to safely progress, shortly after one week, until test #134, when the engine did not fire. Then tests #135 and #136 closed down the qualification test-campaign.

Besides firings #131 and #134, which make no data recording possible, all the necessary data have been collected for the post-processing of the remainder of the tests. Table 5.1 gathers the parameters of interest, as measured or estimated from measurement data, for each of the firings, as well as the theoretical performance expected from the flight model. Here follow some general considerations about the test campaign and the data in the table:

- test #132 could not reproduce the exact conditions of test #130 preceding the clamping ring failure in test #131 in between
- a quick look at key parameters - such as thrust and mixture ratio - and their evolution throughout the campaign indicates that the series of tests gradually shifted the working point of the engine, firing by firing, closer to

the prescribed design point although the performance requirements have not been met completely

- basically, chamber pressure and mixture ratio have been increased in order to strike the expected performance. Measured data in the chamber indicate a decrease in pressure which is readily proven wrong by the increasing measured values of thrust first, and by the theoretical predictions for the same magnitude then. It seems like the pressure sensor did not work properly or somehow a correct pressure evolution in the chamber has been perturbed. As for the mixture ratio, already the open combustion tests had shown the difficulties in tuning it when both propellants are operated
- the displayed values of chamber temperature are not representative of the actual temperature of the gas mixture within the chamber. They rather relate to the adiabatic flame temperature of the combustion process
- the graphite nozzle exhibited clearly signs of erosion. In particular the diameter at throat station underwent a 28% increase

A detailed analysis of test #136 - which, being the campaign-closing firing, pushed the performance closest to theoretical predictions - will further clarify the data-reduction process as well as the above mentioned points.

### 5.2.2 Test #136: full data reduction

The starting point in test-data reduction is the spreadsheet generated by exporting the recorded data from LabVIEW. Of particular interest, for the sake of performance evaluation, are the informations produced by the thrust load cell, the two mass flow meters and the pressure transducer. In post-processing the data, the scheme in Fig. 5.4 will be followed.

So, the first step is the thrust versus time plot, shown in Fig. 5.5. By cutting the build-up and tail-off transients out of the firing time, and considering a time interval upon which thrust oscillations compensate each other, thus making thrust constant on average, a convenient time of "constant" thrust  $t_{CT}$  is defined. The area under the curve tract delimited by  $t_{CT}$  (grey coloured in Fig. 5.5) is by definition the total impulse:

$$\begin{cases} t_{CT} = 19.42 \text{ s} \\ I_t = 8194.95 \text{ Ns} \end{cases}$$

Then, again by definition, the delivered thrust follows as:

$$F_T = \frac{I_t}{t_{CT}} = 422 \text{ N} \quad (1)$$

The mass flow meters recorded the mass flow rate of each propellant over the firing time, as one can see in Fig. 5.6. Although the subject of measurement is the same, still the curve shape differs from one propellant to the other. Indeed different the measurement sensors, different the shape of the curves. The ethanol characterization in terms of mass flow rate is accomplished (as already stated in Chapter 4, § 4.2.2) through an orifice flow meter, whereas a Coriolis-type meter measures the liquid oxygen flow. If the former device, under the sudden shock following the valve opening, experiences a bending of the measuring orifice, ultimately resulting in a mass flow increase - which explains the ethanol curve hiking vertically, up to a local peak, before setting on a steady value - the slower reaction time of the latter causes a tardive yet more gentle rise in the LOX mass flow, which in the end results in an overall shift of the LOX curve. In order to correct for this measurement delay, the LOX curve has been shifted back by a time interval of 3.59 s corresponding to the distance between the maxima of each curve. The maximum point of each curve is reached at the valve-closing time and, unlike the response to the valve-opening command, the response of each device to the sudden flow stop is the same: an instantaneous drop in the mass flow, right after the maximum. In this way the evaluation of the LOX mass flow rate, averaged over  $t_{CT}$ , makes sense. Hence the overall propellant mass flow rate and the oxidizer to fuel mixture ratio are readily calculated:

$$\left\{ \begin{array}{l} \dot{m}_P = \dot{m}_O + \dot{m}_F = 103\text{g/s} + 132\text{g/s} = 235\text{g/s} \\ O/F = 1.28 \end{array} \right.$$

The delivered thrust and the propellant mass flow rate, along with the local value of gravitational acceleration ( $9.83537 \text{ m/s}^2$  in Dresden) allow the calculation of the specific impulse, followed by the effective exhaust velocity:

$$I_{sp} = \frac{F_T}{g\dot{m}_P} = 183 \text{ s} \quad (2)$$

$$c = I_{sp}g = 1796 \text{ m/s} \quad (3)$$

One last data is missing in order to complete the set of performance parameters for the engine, that is, the pressure in the combustion chamber, the evolution of which, over the firing time, is presented in Fig. 5.7. Generally speaking, the recorded values of pressure are quite low and its trace over the firing time is unique among the series of tests, in the sense that it exhibits a quite unusual evolution:

- after a peak of  $\approx 0.9 \text{ MPa}$  following the combustion starting, pressure evolves steady for the next few seconds, maintaining a slightly above  $0.8 \text{ MPa}$  value
- afterwards, pressure drops down to a few seconds steady minimum of  $\approx 0.25 \text{ MPa}$  before rising up again to  $\approx 0.75 \text{ MPa}$  until engine shutdown

- the same concave tract of the pressure trace exhibits clear oscillations of increasing amplitude

As mentioned earlier in this chapter, the graphite liner underwent erosion throughout the campaign, which resulted in a  $\approx 5$  mm throat-area enlargement at the end of test #136. Furthermore test #136 represents the highest mixture-ratio firing throughout the campaign with an average value of 1.28 (test #132 aside, the levels of pressure and thrust of which are considerably below the design point). Now putting the pieces together, it is clear that the engine operated in off-nominal conditions during test #136 with a throat probably already enlarged by previous firings, an erosion-enhancing mixture-ratio excursion towards less fuel-rich values and the consequent erosion-related pressure lowering in the chamber. The concurrence of multiple off-design conditions seems somehow to have triggered a combustion instability in the chamber. In support of this scenario is Fig. 5.8. By applying a noise-cleaning Savitzky-Golay filter, the pressure trace becomes more clear, revealing plain signs of what appears to be a rough combustion at least. The initial ignition and combustion-starting transient is followed by a short horizontal steady tract, which is interrupted by a downward spike marking the entering of chamber pressure in an unstable condition, since it causes a 13% decrease in pressure, whereas in literature a  $\pm 5\%$  variation is reported as the stability limit. Afterwards, the amplitude of pressure fluctuations is clearly increasing along the downhill tract, indicating a deepening departure away from stability. Then the trace reaches a minimum of  $\approx 0.25$  MPa, "maintained" for  $\approx 3$  s, along which the amplitude, although still being high-frequency, stabilizes. Finally the uphill tract comes, with a rise bringing pressure back to a  $\approx 0.75$  MPa steady tract for the following  $\approx 1.5$  s preceding shut-down, marking a recovery from the unstable condition with oscillation damping. Interesting and revealing is the correlation between chamber pressure and the mixture ratio evolution over the instability rising and recovery duration. The two magnitudes are plotted together in Fig. 5.9. The instability initiation time  $t_i = 8.37$  s - corresponding to the last peak in pressure within 5% of the local average value - is characterized by the mixture ratio  $O/F(t_i) = 1.3192$ . The downhill increasing-amplitude tract of the pressure curve ends at the recovery initiation time  $t_r = 15.61$  s. At the same instant the mixture ratio curve has reached its maximum and starts decreasing. Pressure is averagely stable until the damping initiation time  $t_d = 18.78$  s, when mixture ratio is back to a 1.3192 value:

$$O/F(t_i) = 1.3192 = O/F(t_d)$$

In conclusion, the observed pressure instability along with the mixture ratio evolution are interdependant.

We have already mentioned erosion and the role it played in lowering the chamber pressure, but we omitted its effect on the engine performance. For fixed-area injectors and fixed propellant supply pressures - both conditions were encountered during test #136 execution - erosion in the near-throat region results in a

propellant mass flow increase with time, which in turn causes a thrust augmentation and a specific impulse decrease over the firing time (see Fig. 5.10, where thrust and specific impulse values have been averaged for the sake of the trend visualization).

Alternative estimations of the pressure in the chamber have been given through a procedure involving the calculation of chemical equilibrium of the combustion gases, performed with the CEA tool. The isentropic one-dimensional nozzle theory, allows to express the mass flow rate per unit area as the pressure in the chamber times a function of several properties of the gas mixture, namely temperature, molecular mass and specific heat ratio:

$$\frac{\dot{m}_P}{A_t} = p_c \left( \frac{\gamma \sqrt{\gamma R T_c}}{\sqrt{\left[ \frac{2}{\gamma+1} \sqrt{\frac{\gamma+1}{\gamma-1}} \right]}} \right)$$

The left member is readily calculated as follows:

$$\frac{\dot{m}_P}{A_t} = \frac{0.235 \text{ Kg/s}}{\pi(0.009 \text{ m})^2} = 923 \text{ Kg/s-m}^2$$

The throat radius is set to the design value of 0.009 m, not taking into account erosion from previous firings. As for the product to the right, given the previously calculated mixture ratio for test #136, pressure is varied - and mixture properties at chemical equilibrium along with it through the CEA tool - until convergence is achieved. In this way, the chamber environment is characterized in terms of the following pressure and temperature values:

$$\begin{cases} p_c = 1.505 \text{ MPa} \\ T_c = 3000 \text{ K} \end{cases}$$

It has to be pointed out that the above value of temperature does not represent the actual temperature in the chamber, which is lower due to the diabaticity of the combustion process to a certain extent and to the passive cooling strategy implemented in the chamber. It rather represents the adiabatic flame temperature for the combustion reaction as modeled through the CEA tool with the experimental 1.28 mixture ratio as input. The chamber temperature estimation formula adopted in Chapter 5, § 5.3.5 while modeling convection on the faceplate, would now result in a more realistic 2737 K value.

Finally, the chamber pressure estimation unlocks the calculation of the last two performance parameters, that is, characteristic velocity and coefficient of thrust:

$$c^* = \frac{p_c A_t}{\dot{m}_P} = 1630 \text{ m/s} \quad (4)$$

$$C_T = \frac{F_T}{p_c A_t} = 1.1 \quad (5)$$

### 5.2.3 Post-processing of temperature data

Additional data, available for post-processing, come from the temperature sensors. Of particular interest - in order to validate the thermal-mechanical analysis of Chapter 5 - are the temperature values registered by thermocouples (see Fig. 5.11):

- TC $\emptyset$ , located on the outer surface of the ceramic shell, precisely at the end of the combustion-chamber cylinder
- TC6 and TC7, installed in the injector head, in the middle of one of the ribs separating the forty cooling channels. Precisely, the former is situated on the back side of the front plate and the latter two mm deeper in the middle of the front plate, half way in the exhaust direction.

Figures 5.12, 5.13, 5.14, compare the experimental values of temperature, as sampled over the total firing time of 26 s defined for test #136, with numerical predictions outputted by the ANSYS software and calculated over a numerical burning time of 20 s, at each of the spots of interest. Now, provided that the thermocouples flawlessly functioned during the test, whatever the measuring spot considered, generally speaking, a good agreement in terms of trend and ranges of temperature can be observed between measured data and numerical estimations. Starting from ignition and throughout the firing time, temperature rises monotonically since no thermal equilibrium is allowed, as one would expect from a heat-sink thrust chamber. Focusing on the numbers, numerical predictions slightly overestimate the temperature on the two injector plate spots by +11% for TC6 and +9% for TC7. Overestimation becomes more important on the ceramic shell spot with a +35% gap. Since the temperature value registered by sensor TC $\emptyset$  results from a temperature drop by means of conduction - through graphite first and OCMC then - and forced convection at the gas-wall interface, that +35% gap between numerical prediction and experimental datum on the same spot, means that the combustion gas temperature, as well, has been overestimated, which ultimately suggests, either that the shielding effect of the ethanol outer cone is much more effective than the way it has been modeled numerically, or the maximum temperature value within the chamber - achieved, in our model, at the end of the cylindrical section, when the shielding effect is over, and corresponding to the adiabatic flame temperature of the LOX/Eth70 combustion - is unrealistically too high. This represents a crucial point, since temperature values (and therefore heat transfer coefficients, heat flux and stress in cascade) for the points downstream of the maximum chamber-temperature spot, depend on that maximum value of temperature. Furthermore, performance evaluation in the previous paragraph has shown that the engine operated in off-design conditions. The consequent combustion instability (and additional erosion to a minor extent), might have enhanced heat fluxes and temperatures. Hence lower values of temperature are expected for the engine operating on the prescribed design conditions. This further enlarges, potentially,

the gap between measured and numerically estimated temperatures. The last considerations suggest a change in the way the temperature evolution in the chamber is modeled, in order to ensure a higher adherence of the model to reality. Now recalling Fig. 4.19, which shows the adopted gas-temperature profile, in order to preserve a minimum level of conservativity of the model itself, the modification should only affect the maximum value reached by temperature at the peak of its quadratic-like raise starting from the injector plate, since the few percentage points distance on measuring spots TC6 and TC7 can be regarded, indeed, as a conservative margin. To this purpose, the maximum temperature could be lowered until the gap between experimental and numerical datum on spot TC $\emptyset$  falls in the order of, say, 10%, just like on spots TC6 and TC7. Further improvements that could contribute to perfect the numerical model, might include the introduction of non-linear behavior for the materials (the local value of which would be influenced by the temperature on a considered spot, through the local, temperature-dependant materials' properties), a finer modeling of the OCMC material (through the definition of plies, stacking sequences, as well as material orientation and orthotropic properties) and the inclusion of radiative heat fluxes.

### 5.3 Conclusions

The engine cannot be designated as ready-for-flight hardware. Not because any design flaw came to light under test, nor because any dramatic failure occurred imposing a drastic redesign of the engine, but simply because of unmatched design conditions throughout the test campaign. Indeed our reference in assessing the performance delivered by actual hardware is test #136, which undoubtedly pushed the performance closest to theoretical predictions, but did it under off-design conditions. Particularly:

- a less fuel-rich mixture ratio (eight tenth above the design value), resulting in an overall more severe heat load
- erosion in the near-throat area, which reduced the pressure in the chamber to values not large enough to achieve the thrust level prescribed by requirements
- a nonstable combustion in the chamber, likely related to the mixture-ratio excursion during the test

As a consequence, the recorded values of thrust, mass flows, pressure as well as temperature on well-defined spots, are not representative of the functioning of the engine on the prescribed design conditions.

It would be enough to say that design parameters values as set by requirements - 500 N of thrust, 15 bar of chamber pressure, a 1.2 mixture ratio, along with

250 g/s of propellant mass flow - have not been met completely. But let the numbers talk, by introducing the following correction factors, as defined by Huzel et al. [3], thus quantifying how distant the engine is from its ideal counterpart:

$$\eta_{F_T} = \frac{\text{actual thrust}}{\text{ideal thrust}} = \frac{422}{500} = 0.84, \quad \eta_{F_T} \in [0.92; 1]$$

$$\eta_{I_{sp}} = \frac{\text{actual sp. impulse}}{\text{ideal sp. impulse}} = \frac{183}{225} = 0.81, \quad \eta_{I_{sp}} \in [0.85; 0.98]$$

$$\eta_{\dot{m}_p} = \frac{\text{actual prop. mass flow}}{\text{ideal prop. mass flow}} = \frac{0.235}{0.250} = 0.94, \quad \eta_{\dot{m}_p} \in [0.98; 1.15]$$

None of the above values is within the typical ranges suggested by the authors, not even the specific impulse-related efficiency, despite presenting the smallest lower limit of 0.85 among the three ranges.

Even though the design values for the performance parameters were not struck with sufficient margin, important lessons have been learned and will be actively taken into account for future testing of the engine.

**Table 5.1:** Comparison between expected and under hot-fire test delivered performance

Parameter	FM design	#130	#132	#133	#135	#136
Thrust [N]	508	236	192	305	303	422
Firing time [s]	20	7	15.5	18.7	18.4	19
Oxidizer mass flow [Kg/s]	0.1364	0.086	0.103	0.096	0.099	0.132
Fuel mass flow [Kg/s]	0.1136	0.081	0.062	0.094	0.092	0.103
Mixture ratio [-]	1.2	1.06	1.66	1.02	1.08	1.28
Specific Impulse [s]	225	144	118	163	161	183
Chamber pressure [MPa]	1.5	0.75 <sup>a</sup>   1.055 <sup>b</sup>	0.8   1.02	0.7   1.19	0.7   1.21	0.6   1.505
Chamber temperature <sup>b</sup> [K]	2913	2782	2981	2717	2819	3000
Characteristic velocity <sup>b</sup> [m/s]	1657	1606	1573	1594	1612	1630

<sup>a</sup> Measured value<sup>b</sup> CEA estimation



**Figure 5.3:** Test #131: thrust chamber detachment and consequent impact damage

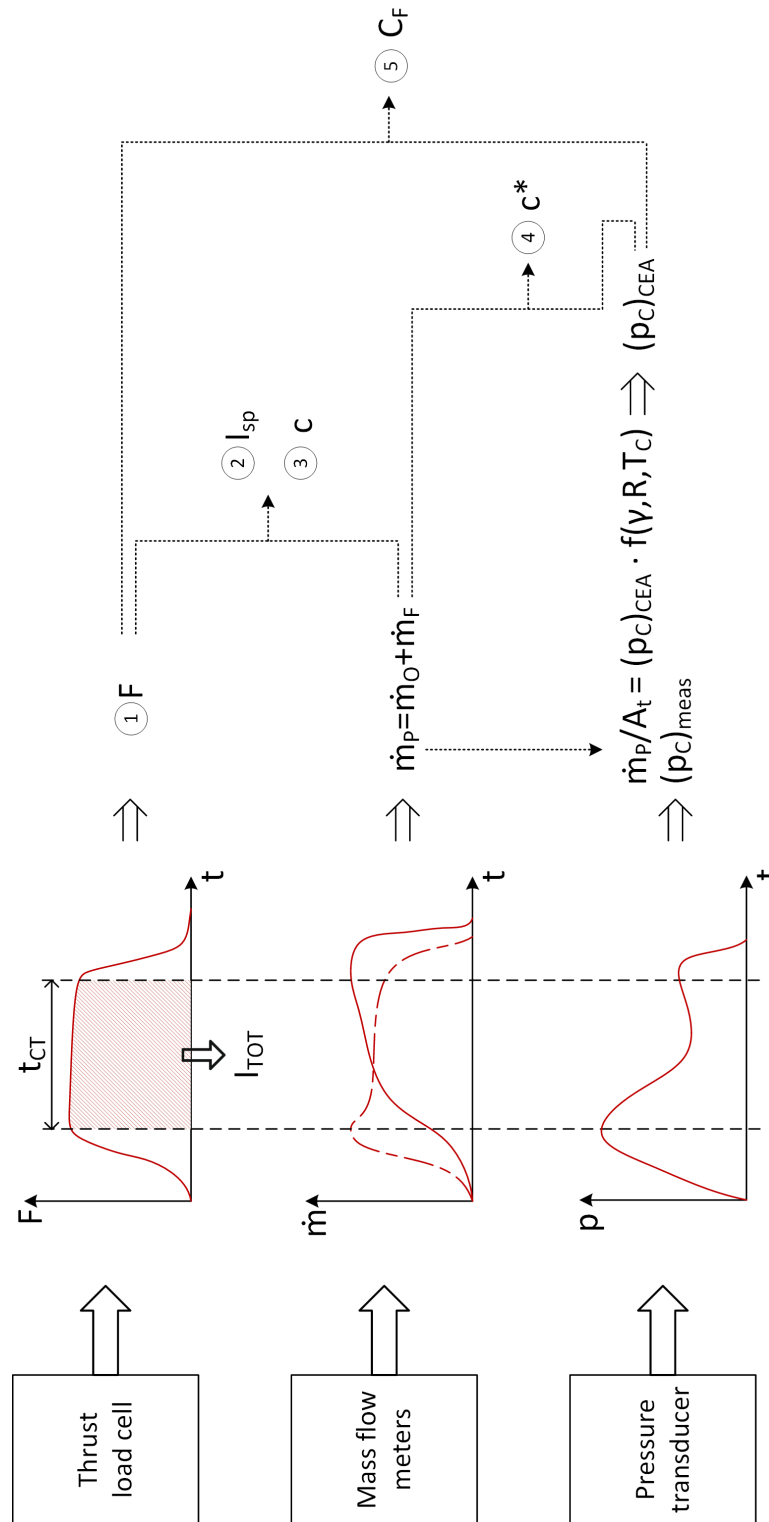
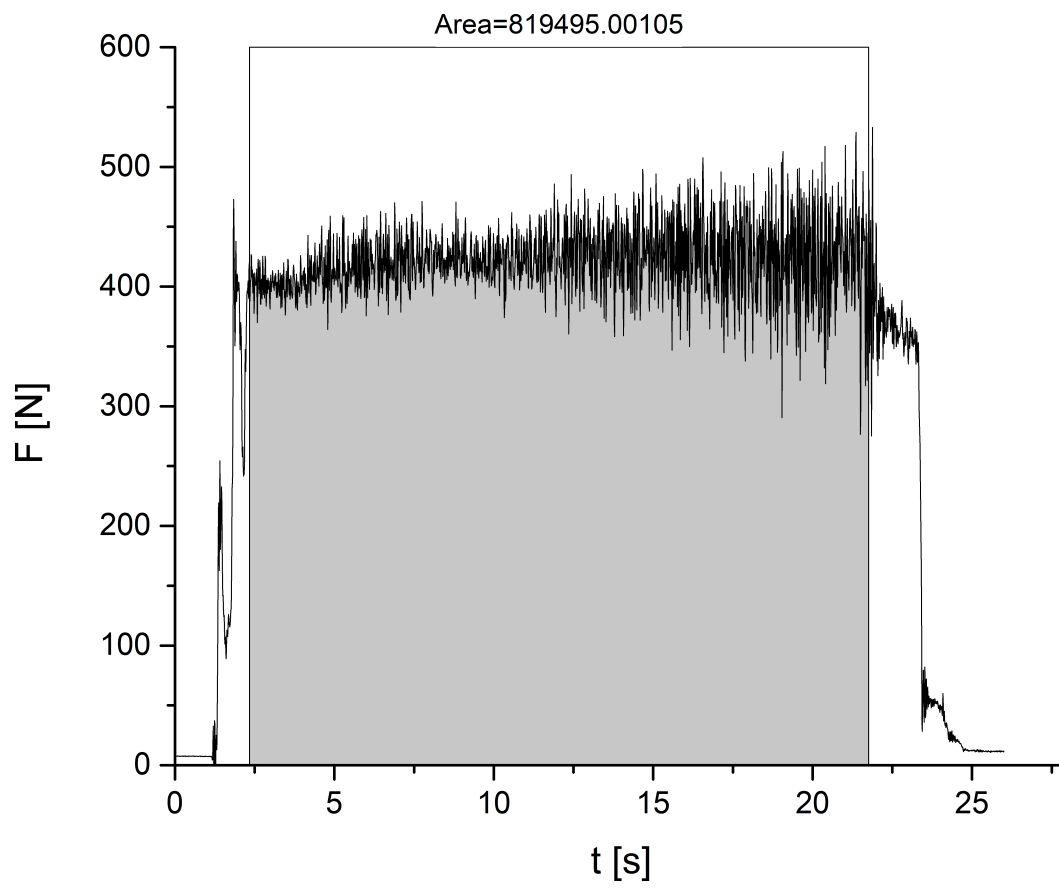
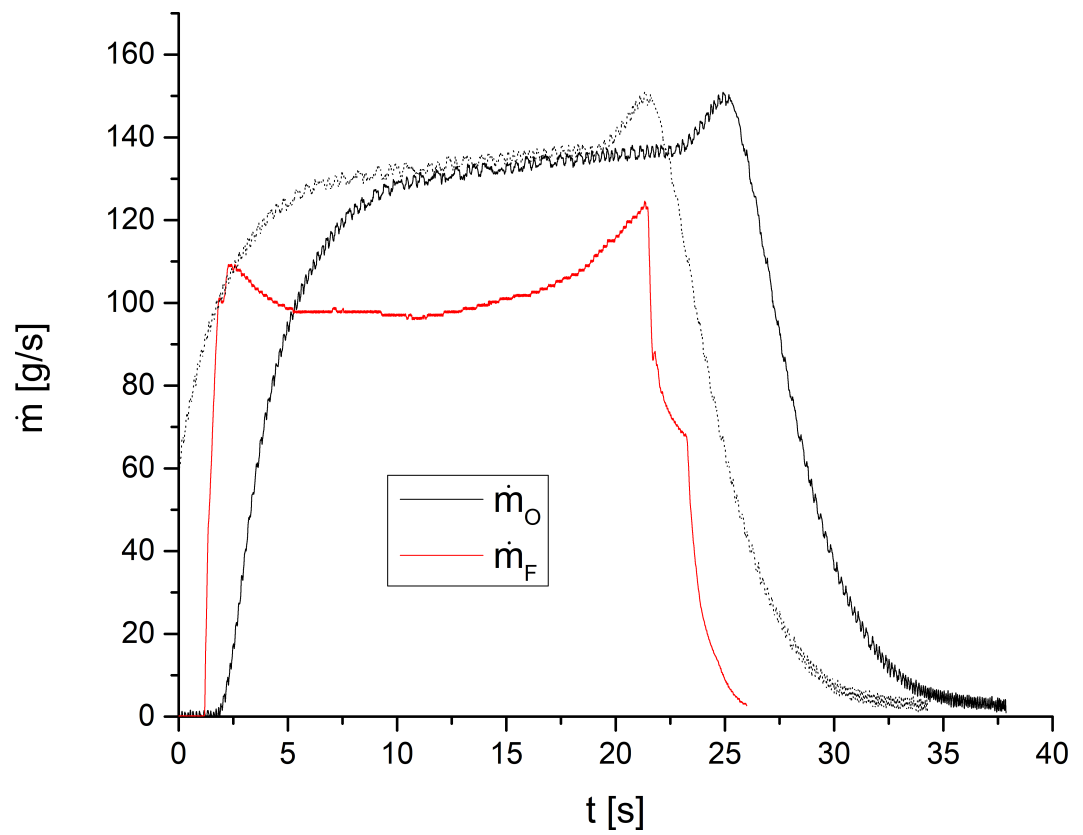


Figure 5.4: Data reduction scheme



**Figure 5.5:** Thrust vs time curve



**Figure 5.6:** Mass flow rate over burning time

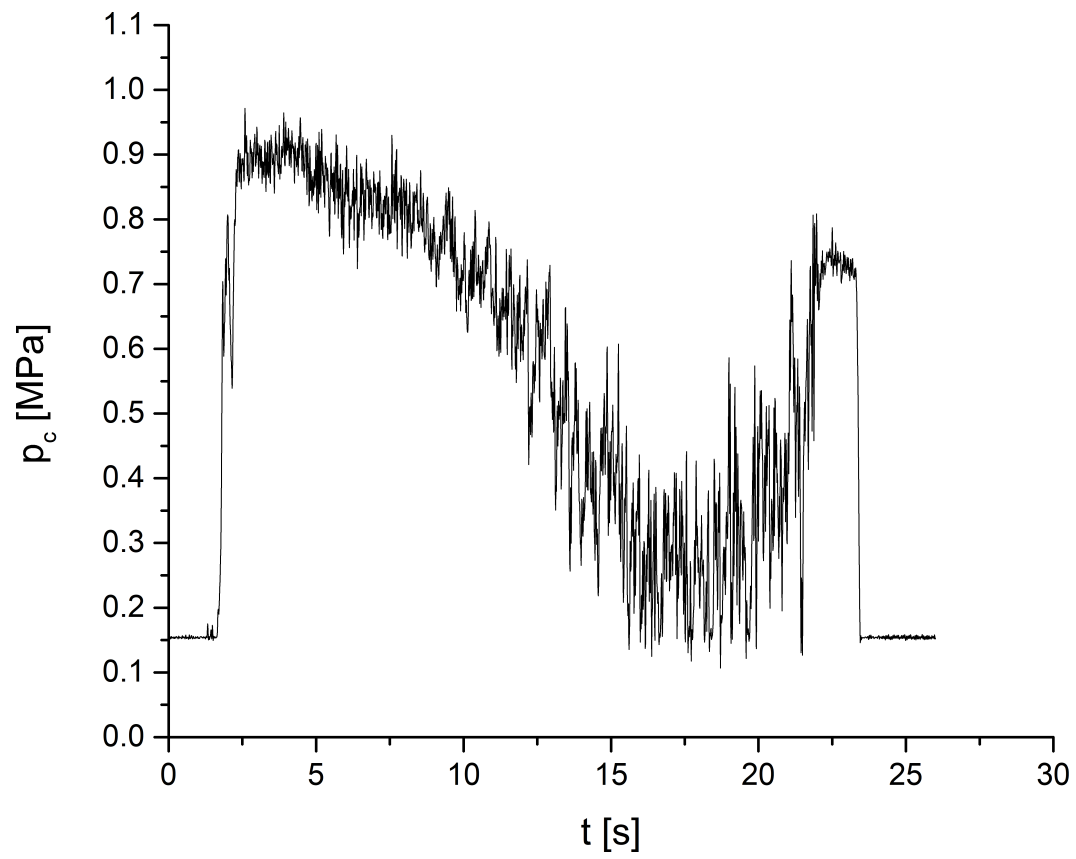


**Figure 5.7:** Pressure in the combustion chamber over the burning time

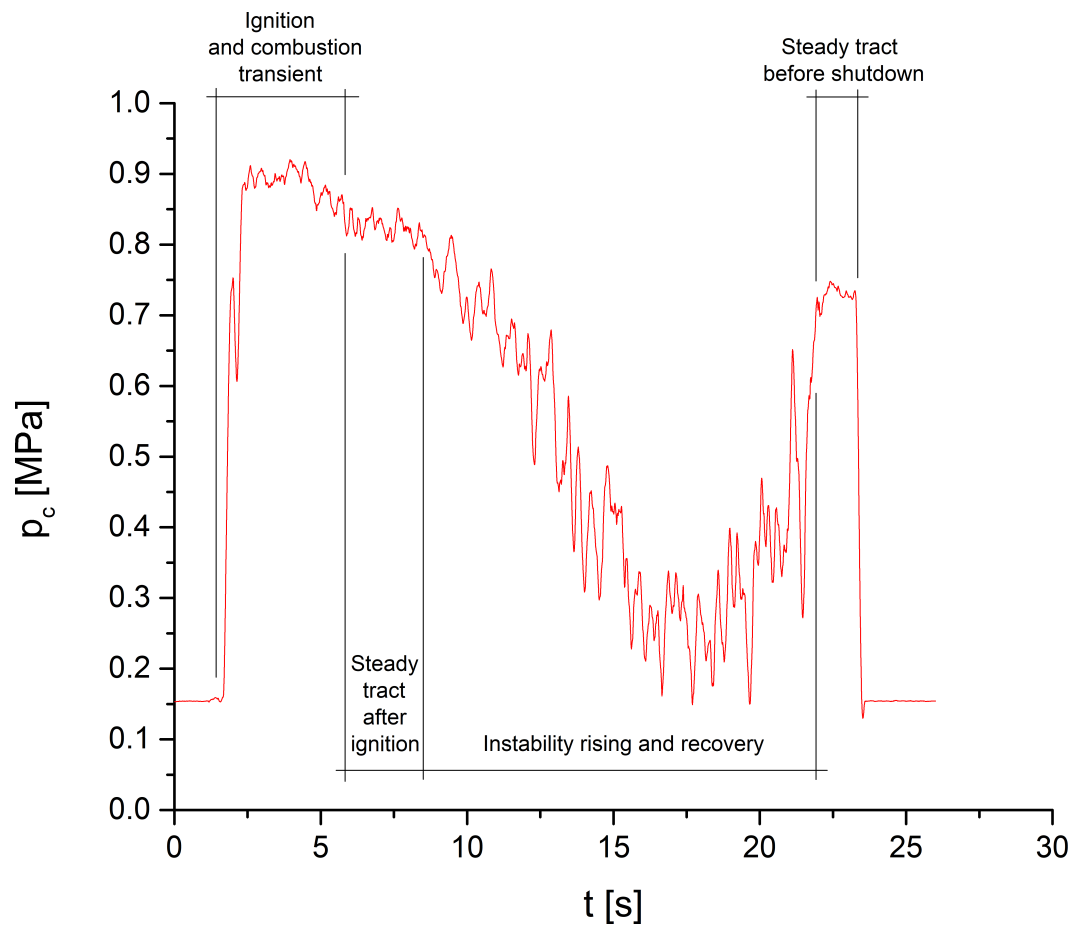


**Figure 5.8:** A detailed analysis of chamber pressure evolution

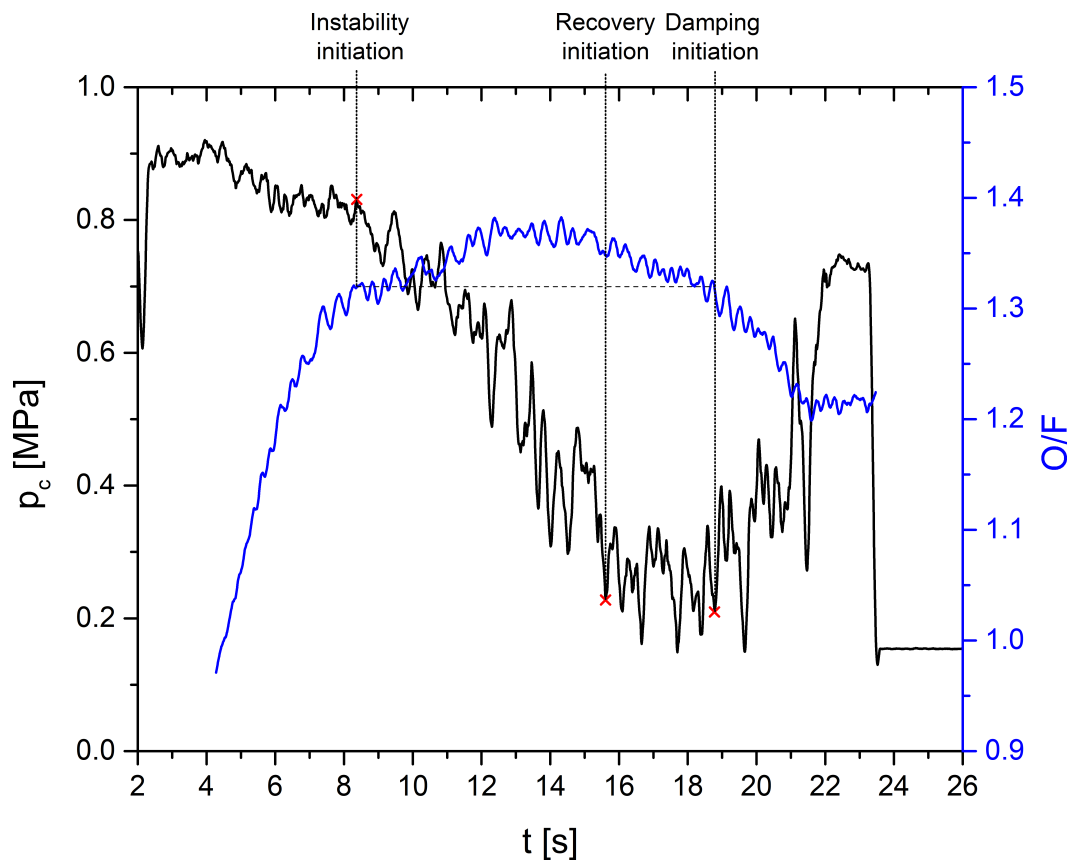


**Figure 5.9:** Correlation between pressure instability and mixture ratio

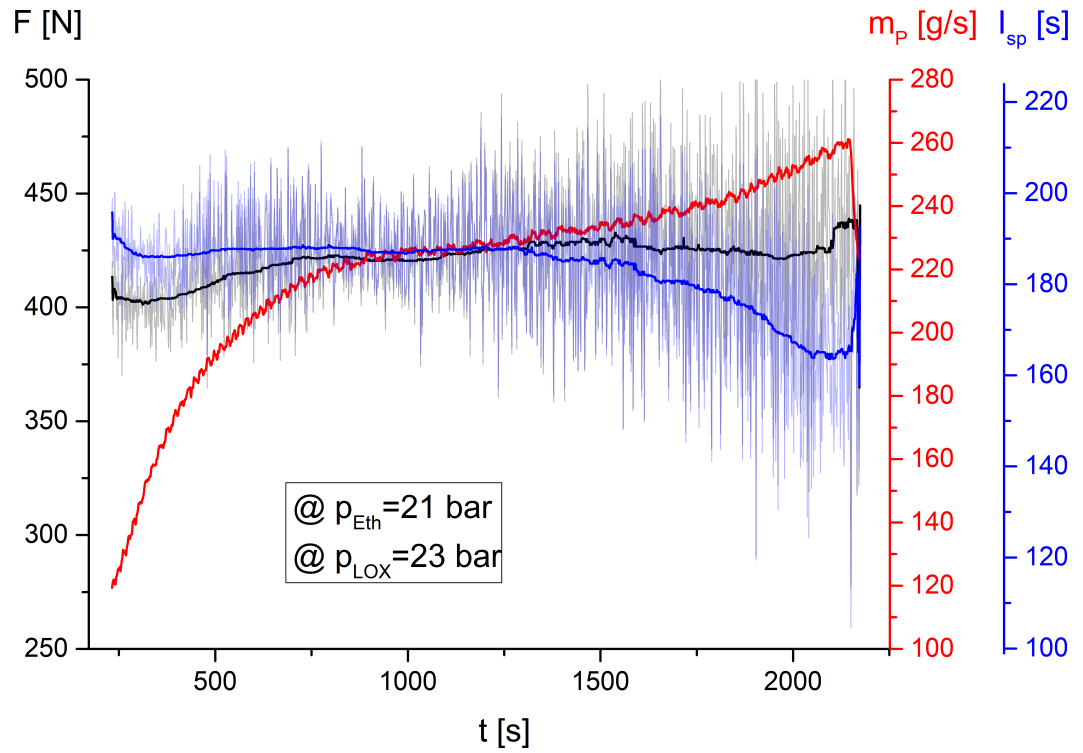


Figure 5.10: Effects of erosion on the engine performance

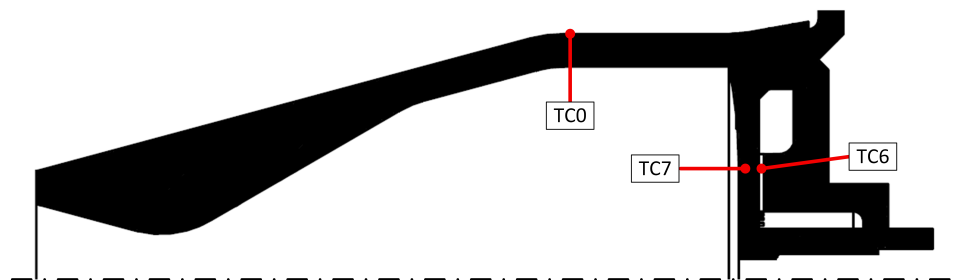
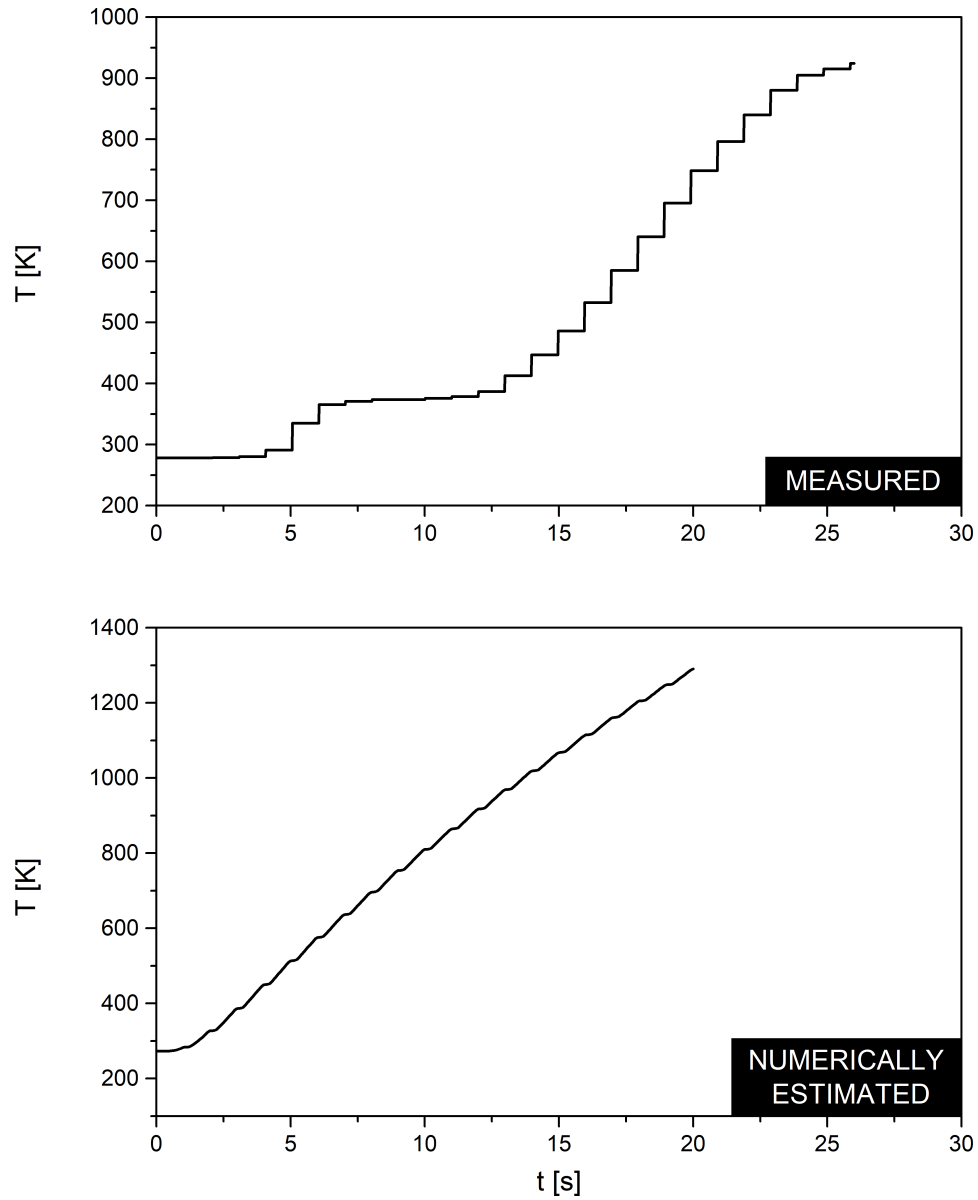
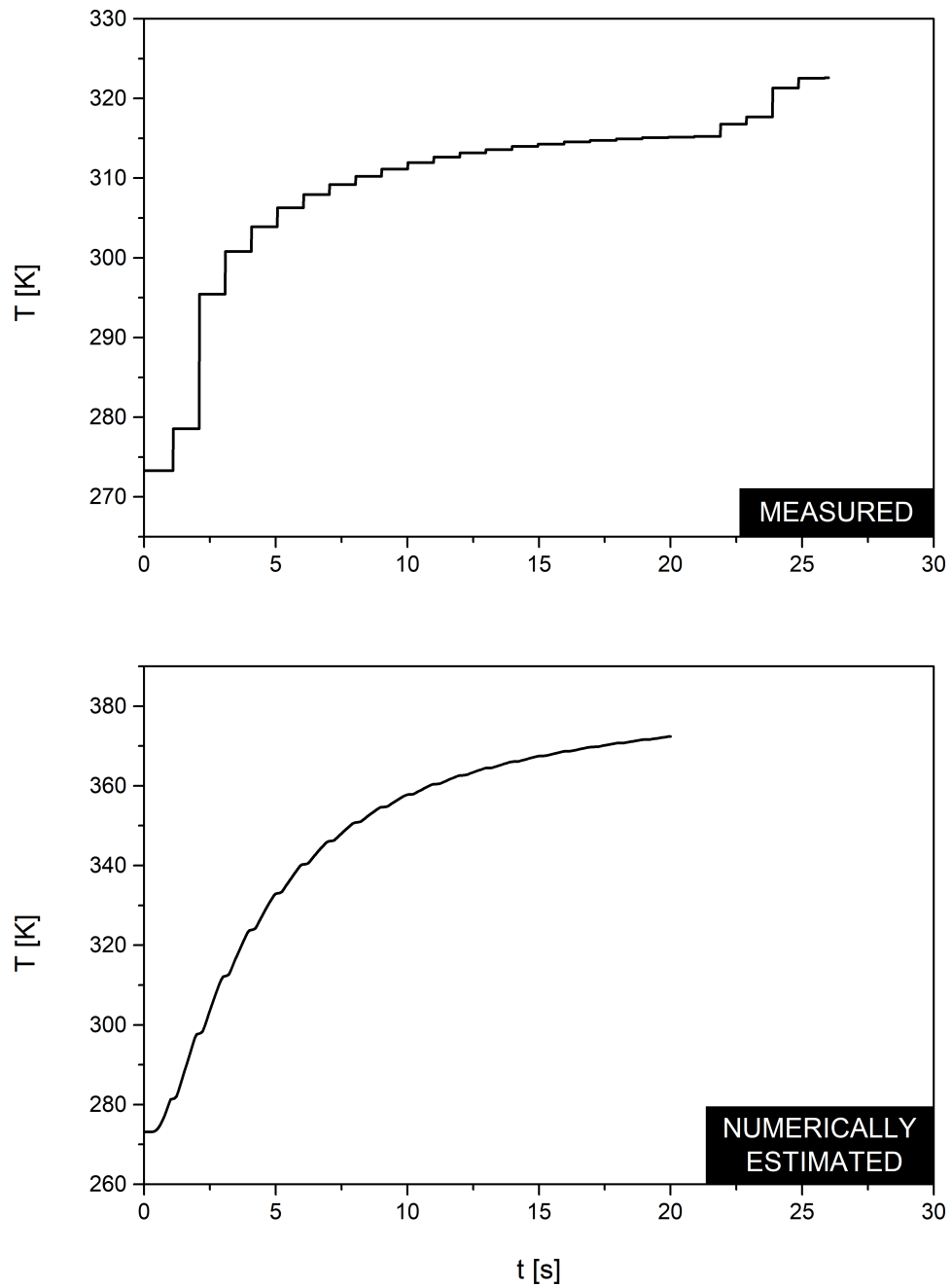


Figure 5.11: Thermocouples positions



**Figure 5.12:** Temperature evolution over the firing time at TC $\emptyset$  measuring point



**Figure 5.13:** Temperature evolution over the firing time at TC6 measuring point

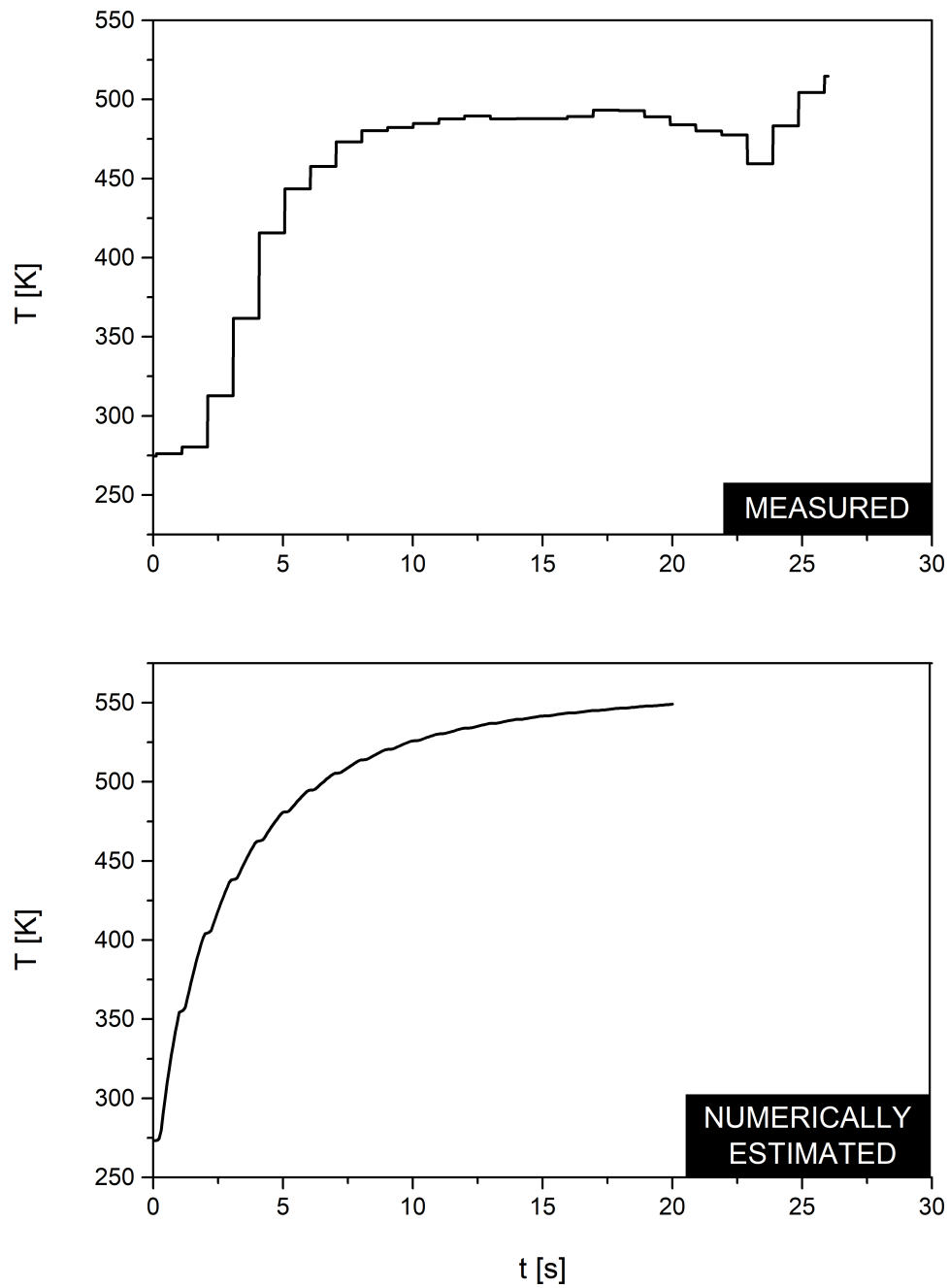


**Figure 5.14:** Temperature evolution over the firing time at TC7 measuring point



## Chapter 6

# Switching to a 700 N thrust chamber

The lack of success in the last test campaign comes along with a series of lessons learned to put into effect in the next firing session, which will test an improved version of the engine, capable of delivering 700 N of thrust. This last chapter is devoted to derive minor design changes aimed at switching to such a thrust-level capable chamber.

### 6.1 Taking the engine to the next thrust level

Whatever the engine version so far tested by the team, the thrust level has been kept anchored to 500 N, thus meeting requirement PR-3000-FPAM-002 ("The rocket engine shall produce a thrust of at least 500 N.") on the borderline. Furthermore, according to requirement PR-0000-FP-AIT-017, the maximum lift-off weight is expected to fall within 25 Kg, a weight limit beyond which the rocket should be flight-certified as imposed by the german civil aviation authority. Now, a 500 N thrust rocket weighing 25 Kg would provide a thrust-to-weight ratio of roughly 2, not enough to ensure an adequately safe stability as soon as it leaves the launch rail. Here comes the necessity to switch to 700 N of delivered thrust:

$$\text{Thrust-to-Weight} = \frac{700}{25 \cdot 9.83537} \approx 3$$

We are looking for the cost-effective, weight-penalty free solution to achieve the desired level of thrust. The starting point is the last test campaign and to what extent its outcome affects the forthcoming development of the engine.

#### 6.1.1 Post-campaign lessons learned

During the last test campaign, besides the quick in-campaign recovery from the clamping ring rupture, the engine survived four firings in a row without suffering any critical failure which could have impacted the redesign of the thrust-

chamber in an expensive way. For this reason the overall layout of the engine - namely a heat-sink thrust chamber backed by a regeneratively cooled injector plate - as well as the selected materials, stay unchanged and confirmed, provided that the mixture ratio excursion is limited to values not greater than 1.2. Indeed the extreme post-run erosion experienced by the graphite nozzle in the near throat region, set off alarm bells among the team members. Further post-processing of test #136 data in Chapter 6, has shone a spotlight on the mixture ratio as the main cause behind erosion. Its 1.28 value increased the oxidizer content and the temperature in the chamber. The graphite nozzle experienced higher heat fluxes, which in turn increased the reactivity of the graphite material, thus favoring reactions with oxidizing species being part of the combustion gases. In addition to thermo-chemical erosion, a mechanical erosion mechanism could also have contributed to the nozzle's walls regression, due to the high-prevailing shear stress upon the near-throat surface as well as the high mechanical stress arising in the graphite, locally inducted by significant heat fluxes. Now, in order to prevent such a performance-lowering operating condition from occurring again, the following two countermeasures could be adopted by either modifying the nozzle material or by acting upon the mixture ratio. Specifically, one could:

1. redesign the nozzle to accommodate a throat insert, which would allow to keep the mixture ratio set on 1.2
2. simply step back to a 1.1 mixture ratio

Let us weigh pros and cons of each solution. The former would certainly preserve the performance (i.e. the specific impulse) by keeping the mixture ratio the same as in the last test campaign; but this choice would implicate a redesign process (material selection, sizing, integration and test of the insert), which means cost increase and weight penalty. The latter would trade performance for safety: lowering the mixture ratio within already test-proven excursions at the cost of a slight performance reduction. Considering the current advanced status of the project (a Production and Qualification D phase in ESA-ese), it seems a wise compromise to accept a few seconds reduction in specific impulse, rather than embarking on a potentially expensive and time-consuming redesign process.

### **6.1.2 Thrust-to-Weight ratio augmentation**

As mentioned above, a safer thrust-to-weight ratio value is struck through a thrust-level augmentation from the 500 N of the current design to the envisaged 700 N of the improved flight model. In practice, since the propellant combination and the geometry are frozen, the overall propellant mass flow is the key parameter to modify in order to regulate the thrust level, as one can see from the expression for the net thrust delivered by a rocket, eq. 2.1:

$$F = \dot{m}_p u_e + A_e(p_e - p_a)$$

In particular, an increase in  $\dot{m}_p$  results in a quasi-proportional pressure raise in the combustion chamber according to the following relationship derived from a transformation of eq. 2.3:

$$p_c = \dot{m}_p \frac{c^*}{A_t}$$

Indeed, for fixed propellant combination and nozzle geometry (in particular the throat section area  $A_t$  in the formula), the mass flow increase in the improved design will slightly reduce the characteristic velocity. To this fact is due the non exact proportionality of the relationship between pressure and mass flow. Furthermore the increase in chamber pressure will produce a temperature raise in the chamber, at any rate more than compensated by the switch to a more fuel rich mixture ratio in contrast with the current design. Finally, the chamber pressure raise will in turn result in a proportional augmentation of the thrust delivered by the engine.

What have been discussed so far in the present section is confirmed by data in Table 6.1, which compares one design to the other in terms of classical parameters and theoretical (ideal) performance of a rocket engine. In order to quantify the propellant mass flow increase requested to achieve the desired level of thrust, the Chemical Equilibrium and Application (CEA) tool has been employed. The input data required by the program include:

1. chamber pressure
2. geometry, i.e. expansion area ratio and contraction area ratio
3. propellant specification in terms of fuel's and oxidizer's species, moles and temperatures of reaction
4. oxidizer to fuel mixture ratio

Starting from the CEA model pertaining to the 500 N design, geometry as well as propellant combination (the only exception being the moles of reactants to update after the requested propellant mass flow has been defined) are kept frozen as already stated, the mixture ratio is lowered from 1.2 to 1.1 and the chamber pressure is raised until the desired thrust level is struck in output with sufficient margin. The effective exhaust velocity is outputted as well and allow a calculation of the corresponding propellant mass flow through formula 2.6:

$$\dot{m}_p = \frac{F}{c}$$

The mass flow so obtained, is then used along with the new mixture ratio to update the moles of reactants by following the same procedure as in Chapter 5,

§ 5.3.3. Finally one last run of the program will produce the numbers in Table 6.1, third column.

### 6.1.3 Combustion chamber lengthening

Already in Chapter 6, § 6.1 the appropriateness of the combustion chamber length has been questioned, in light of a comparison with historical successful designs, which indicated the current design as off-trend with a short chamber. Inadequate sizing potentially threatens the completeness of the combustion process, that is, the vaporization-mixing-reaction processes are not completed within the residence time allowed to each particle. Since the theoretically required combustion volume is also a function of the mass flow rate of the propellants - an increase of which is envisaged in order for the rocket to produce more thrust - a lengthening of the combustion cylinder becomes mandatory. The question is how much longer the chamber should be. The on-trend value for the chamber length, as suggested by comparison with previously successful designs, amounts to 0.093 m. But this value does not take into account the injector type as well as the propellant combination (thus, talking about dimensions, the characteristic length) of our system, which both influence as well the combustion characteristics and the chamber's volume. Hence, when choosing a suitable value for the chamber length, it makes more sense to rely upon previous, successfully test-proven versions of our system featuring a longer combustion chamber. Particularly, the last engineering model tested (before the current 500 N flight model) achieved a delivered thrust of 470 N with a  $\approx 1.1$  mixture ratio, given the same layout (nozzle geometry and materials selection) and the same combustion characteristic as the envisaged 700 N design, but featuring a characteristic length of 1.6. In conclusion the current flight model's chamber is resized in order to match a 1.6 characteristic length, as follows:

$$L^* = \frac{V_c}{A_t} = \frac{\pi r_c^2 L_c}{A_t} = 1.6 \Rightarrow L_c = 0.07 \text{ m}$$

The chamber lengthening (the geometrical parameters pertaining to it are gathered in the bottom part of Table 6.1) clearly implies some extra weight. In particular the inner graphite liner surrounded by the ceramic outer shell - both are hollow and cylinder-shaped in the thrust chamber portion interested by the combustion process - contribute, each one with its own density, to add 1.2 Kg of extra material.

## 6.2 A summary of the redesign process

Basically, the necessity to switch to a higher thrust level in conjunction with the experience gained through the last test campaign, represented the drivers in the redesign process of the flight model. For each of the drivers, a corresponding design parameter to act upon has been identified, namely:

**Table 6.1:** A comparison between the 500 N and the 700 N designs

<i>Performance parameters</i>			
	<b>Mira 500</b>	<b>Mira 700</b>	$\Delta\%$
Propellant combination	LOX/Eth70	LOX/Eth70	-
Expansion area ratio	2.78	2.78	-
Contraction area ratio	22.3	22.3	-
<u>Propellant mass flow</u> [Kg/s]	0.25	0.33	+32%
<u>Oxidizer to fuel ratio</u>	1.2	1.1	-8%
Oxidizer mass flow [Kg/s]	0.136	0.173	+27%
Fuel mass flow [Kg/s]	0.114	0.157	+38%
Chamber pressure [MPa]	1.5	2.1	+40%
Chamber temperature [K]	2913	2752	-5.5%
Thrust [N]	510	714	+40%
Specific Impulse [s]	225	221	-1.8%
Characteristic velocity [m/s]	1658	1628	-1.8%
<i>Geometrical parameters</i>			
<u>Characteristic length</u> [m]	1	1.6	+60%
<u>Chamber length</u> [m]	0.038	0.07	+85%

- the propellant mass flow rate in order to strike the desired level of thrust
- the oxidizer to fuel mixture ratio as a consequence of a post-campaign lesson learned

A further, third parameter, i.e. the characteristic length of the combustion chamber, has been modified as a consequence of the propellant mass flow increase. The net result of these modifications is a 40% increase in the thrust delivered by the engine at the cost of 4 seconds of specific impulse and 12 newtons of extra weight to lift. The resulting improve in safety during the rocket engine operation, justifies such tiny penalties.



## Chapter 7

# Final thoughts

It is time to sum up what has been done in the present thesis work and draw more general conclusions, looking beyond the numbers so far obtained. In doing so, let us pick it up where we started, that is, the assignment of tasks:

1. Research about rocket engine measurements and their characterization
2. Development of a method for measuring the above derived characteristics
3. Numerical verification (thermal-mechanical analysis) of the flight model design
4. Fire-test verification of the flight model design
5. Post-campaign data reduction and analysis
6. Deriving potential design changes for the 700 N engine

The tasks reflect the transition phase the project was undergoing at the time when they have been assigned, from engineering models to a flight model of the engine - that is, the hardware that, once satisfactorily test-verified, will equip the rocket - thus gradually bringing testing towards the acceptance level preceding the launch. What marked a key-shift from previous designs is a higher value of the mixture ratio, which theoretically means a better performance and, on the flip side, a temperature raise in the combustion chamber. So basically a verification process has been conducted on two levels:

- verification of the higher performance predicted for the engine
- verification of the selected materials against the consequent temperature raise

which ultimately lead back to core-tasks #3 and #4 in the assignment. The verification of the flight model of the engine represents indeed the ultimate goal which the assignment can be reduced to, and which, in the thesis work, breaks down into a numerical verification followed by a test campaign. Before firing the rocket in the attempt to verify the flight model design, a numerical verification, by means of a simulation in a FEA software, has been performed in order to predict the response of the engine's structure to the expected thermal loads, under the renovated operating conditions. The trio of selected materials, which the engine is made up of, as well as the way they are shaped and arranged in the engine, has been numerically confirmed as capable of surviving the thermal loads originating from the unprecedented mixture ratio. The successive test-campaign, although unable to strike the design working point, gave several important indications assisting in the future development of the engine. As a major post-campaign lesson learned, the mixture ratio excursion will be limited in order to avoid the occurrence of erosion phenomena and to ensure a more stable combustion. Then a comparison of experimental data from the temperature sensors with numerical predictions from the thermal-mechanical analysis, suggested that the developed numerical model overestimates temperatures. If on the one hand overestimation - as long as it means a few percentage points gap - can be considered as conservative margin intrinsic to the model, on the other hand it represents a feedback for the improvement of the model itself. And so the maximum temperature in the chamber will be lowered in future simulations so as to strike a better correlation with experimental data, down to a value that anyway ensures a sufficient conservative margin. Further modifications to the numerical model might include a finer modeling of the composite material and the inclusion of radiative heat fluxes. A minor hardware modification will affect the geometry of the combustion chamber in view of the next thrust-improved version of the engine. Indeed, the augmentation of the propellant mass flow as a means of achieving a higher thrust level, imposed a lengthening of the chamber cylinder for the sake of combustion completeness.

The present thesis work marked the entrance of the engine system in a verification process - ultimately aimed at the achievement of a flight-readiness status of the hardware - which necessarily will protract beyond the last test campaign. Further testing will make the system ripe and go for launch. The only team to choose to design a liquid rocket system in response to DLR's call for developed-by-students rockets, the SMART Rockets team at the TU Dresden has so far successfully faced the greater complexity that its choice implies. A bipropellant pressure-fed liquid rocket is on its way to make it to the launch pad. But the greatest accomplishment of all, is that the system has been developed by students. Beyond numbers and technical considerations, the added value of such a programme is indeed the chance students are offered to gain practical experience and know-how in the field. I personally seized the chance and I am very proud of having been part of the team, as a man but most of all as a would-be engineer, with my own mind and ideas.

# Bibliography

- [1] **George P. Sutton, Oscar Biblarz**; *Rocket Propulsion Elements*; Eighth Edition; John Wiley & Sons, Inc; 2010.
- [2] **Martin J. L. Turner**; *Rocket and Spacecraft Propulsion: Principles, Practice and new Developments*; Third Edition; Springer Praxis Books; 2009.
- [3] **Dieter K. Huzel, David H. Huang**; *Modern Engineering for Design of Liquid-Propellant Rocket Engines*; American Institute of Aeronautics and Astronautics; 1992.
- [4] **John D. Anderson, Jr.**; *Introduction to Flight*; Seventh Edition; McGraw Hill; 2012.
- [5] **Christian Bach, Jan Sieder, Frank Wehner, Maximilian Nürnberger**; *Development and Verification of a 500 N Ethanol/LOX Rocket Engine using Oxide-Oxide Ceramic Matrix Composites*; 6th European Conference for AeroSpace Sciences (EUCASS); 2015.
- [6] *ANSYS Mechanical APDL Theory Reference*; ANSYS, Inc; November 2013.
- [7] **P. Nithiarasu, R. W. Lewis, K. N. Seetharamu**; *Fundamentals of the Finite Element Method for Heat and Mass Transfer*; Second Edition; 2016.
- [8] *STERN Project Documentation*; 2015.
- [9] **A. B. P. Benton**; *The Calculated Performance of Ethyl Alcohol-Water Mixtures as Rocket Fuels with Liquid Oxygen*; March 1948.
- [10] **S. McAllister et al.**; *Fundamentals of Combustion Processes*; Mechanical Engineering Series, Springer Science+Business Media, LLC 2011.
- [11] **D. R. Bartz**; *A Simple Equation for Rapid Estimation of Rocket Nozzle Convective Heat Transfer Coefficients*; January 1957.
- [12] **L. Schoenman, P. Block**; *Laminar Boundary-Layer Heat Transfer in Low-Thrust Rocket Nozzles*; August 1967.
- [13] **Richard S. Brokaw**; *Viscosity of Gas Mixture*; Lewis Research Center; April 1968.

- [14] **L. H. Back, P. F. Massier, H. L. Gier**; *Convective Heat-Transfer in a Convergent-Divergent Nozzle*; Jet Propulsion Laboratory; October 1963.
- [15] **P. Kadlec, S. Henke, Z. Bubník**; *Properties of Ethanol and Ethanol-Water Solutions – Tables and Equations*; Department of Carbohydrate Chemistry and Technology, Institute of Chemical Technology, Prague; 2010.
- [16] **A. F. Mills**; *Heat Transfer*; Second Edition; Prentice-Hall; New Jersey; 1999.
- [17] *Stainless Steels at High Temperatures*; Materials and Applications Series, Volume 18; European Stainless Steel Development Association; 2012.
- [18] *High-Temperature Characteristics of Stainless Steels*; A Designer's Handbook Series, N°9004; American Iron and Steel Institute.
- [19] *Properties and Characteristics of Graphite*; Poco Graphites, Inc; January 2015.
- [20] **Donald M. McEligot, W. David Swank, David L. Cottle, Francisco I. Valentin**; *Thermal Properties of G-348 Graphite*; May 2016.
- [21] **A. J. McDonald, P. O. Hedman**; *Erosion of Graphite in Solid-Propellant Combustion Gases and Effects on Heat Transfer*; AIAA Journal, Vol. 3, No. 7; 1964.
- [22] *Oxide Ceramic Matrix Composites – Manufacturing, Machining, Properties and Industrial Applications*; Ceramic Applications; 2015.
- [23] **Narottam P. Bansal and Jacques Lamon**; *CERAMIC MATRIX COMPOSITES MATERIALS, MODELING AND TECHNOLOGY*; John Wiley & Sons, Inc; 2015.
- [24] **E. Volkmann, K. Tushtev, D. Koch, C. Wilhelmi, J. Göring, K. Rezwan**; *Assessment of three oxide/oxide ceramic matrix composites: Mechanical performance and effects of heat treatments*; Elsevier, Composites, Part A; 2015.
- [25] **G. Fiore**; *Design of the Flight Version Combustion Chamber Head and Coaxial Swirl Injector for a LOX-Ethanol Rocket Engine*; 2015.
- [26] **A.D. Baxter**; *Rocket-motor Combustion Chambers*; FLIGHT Magazine, 16 March 1956.
- [27] **S. Gordon, B. J. McBride**; *Computer Program for Calculation of Complex Chemical Equilibrium Compositions and Applications I. Analysis*; NASA Report No. RP-1311, NASA Lewis Research Center, Cleveland, OH, 1994.
- [28] **S. Gordon, B. J. McBride**; *Computer Program for Calculation of Complex Chemical Equilibrium Compositions and Applications II. User's Manual and Program Description*; NASA Report No. RP-1311, NASA Lewis Research Center, Cleveland, OH, 1994.